UNIVERSITEIT
GENT

Faculty of Sciences

Department of Physics and Astronomy

Academic year 2010 – 2011

Neutron exposure and neutron flux in Asymptotic Giant Branch stars.

A study of neutron capture cross sections of Zr isotopes.

Giuseppe Tagliente

Thesis submitted for the obtention of the degree of Doctor of Science: Physics

Promoter : Prof. Dr. C. Wagemans

Co-Promoter : Prof. Dr. N. Jachowicz

"Stanco dell'infinitamente piccolo e dell'infinitamente grande, lo scienziato si dedicò all'infinitamente medio"

Ennio Flaiano

General introduction

About 50 years ago the question of how the elements are created was explained, in the paper Synthesis of the Elements in Stars of 1957 by Burbidge, Burbidge, Fowler and Hoyle (B^2FH)[1]: “*the majority of the chemical elements in the universe is produced through nuclear reactions in the hot interiors of the stars*”.

This fundamental work enacts the birth of nuclear astrophysics, giving new ideas on the astrophysical processes able to explain the abundances of the elements from carbon to the transuranium elements.

While most of the light isotopes are produced via charged particle reactions, the Coulomb barrier becomes prohibitively high above the Fe abundances peak ($Z \geq 26$) for charged particle reactions to play any significant role at energies attainable in a stellar environment. Beyond iron, the only method of production is via neutron induced reactions. There are two dominant neutron capture processes, which differ primarily by the time scale on which they occur. The r-process is a rapid neutron capture process that is related to extremely hot ($T > 10^9$ K), neutron rich environments, and the s-process, a slow neutron capture process, which operates at significantly lower temperatures and neutron density.

The focus of this thesis is on the s-process; the canonical s-process as proposed by [1] takes place in the late He burning stages of the stellar evolution, the so called Asymptotic Giant Branch (AGB) and it was first described in a phenomenological way by assuming an exponential distribution of neutron exposures [2,3]. The abundances produced in the s-process are mostly determined by the neutron capture cross sections of the isotopes involved. These data are required in the energy range from 0.3 keV to 300 keV corresponding to the respective temperature regime between T= 10^8 and 3×10^8 K. While this model was useful to understand the global features of the s-process, it fell short in explaining local structures in the solar abundances distribution, but also with respect to the rich variety of s-abundance patterns observed in AGB stars [4] and in presolar grains [5].

The success of the stellar s-process models could only be achieved by new developments in the neutron capture cross section measurements, which allowed one to obtain cross section data with uncertainties of only a few %. This improved accuracy turned out to be the prerequisite for this application in nuclear astrophysics. However, such data are still largely missing, particularly in the mass region $60 \leq A \leq 100$ as well as for magic neutron nuclei, where cross sections are small and dominated by a single resonance [6].

Accurate s-process analyses have attracted great interest over the last decade, thanks to progress in the astronomical observations and in stellar modeling. In this period, our understanding of the s-process has advanced from the quantitative description of the abundance composition in the solar system towards a comprehensive picture including all aspects of stellar and galactic evolution [7]. This development has emphasized the importance of neutron capture nucleosynthesis for probing the deep interior of Red Giant stars and the following continuous enrichment of heavy elements during galactic evolution.

The Zr isotopes represent important examples for illustrating these possibilities. The small cross section of the magic neutron isotope ^{90}Zr acts as a bottle neck for the reaction flow towards heavier elements.

Therefore, these isotopes build up large abundances and provide evidence for the $^{13}C(\alpha,n)$ reaction as the dominant neutron source [8]. Branchings in the reaction path, which occur at unstable isotopes where neutron capture competes with β-decay, are interpreted as a unique tool for constraining the physical conditions in the He burning zones near the stellar core. A particularly important branching occurs at ^{95}Zr, which allows one to study the s-process neutron flux.

Apart from the impact on problems of nuclear astrophysics, the (n,γ) cross sections of the stable Zr isotopes are of interest for technological reasons as well. Zirconium constitutes an important component in alloys used as structural material in nuclear reactors, e.g. for cladding of fuel elements. In addition, the unstable isotope ^{93}Zr ($t_{1/2}$ = 1.5 10^6 yr) is one of the major long-lived fission products, since it is situated in the maximum of the fission yield distribution.

Chapter I Stellar evolution

1.1 Introduction

The idea that the elements could be formed in the stellar environments was first put forward by Hoyle in 1946 [9]. The other main theories for the origin of the elements considered that the elements were built together in a primordial prestellar phase of the Universe. This idea was based on the assumption, unchallenged at that time, that the stars and the interstellar matter had a uniform and unchanging chemical composition. In the 1950s, however, more detailed observations of the composition of stars became available showing element abundances that differed from those in the sun. In particular, in 1952 Merrill [10] was able to observe the presence of the heavy element technetium (Tc, Z=43) in some type of red giant stars. Technetium is a heavy element with no stable isotopes and its longest-living isotope has a half-life of four million years. Since the time it takes for a star to evolve into a red giant is longer than that, any Tc initially present would have decayed. Its presence, hence, represented a clear sign that its production was occurring somehow within the star.

Within the scenario of stellar nucleosynthesis, only hydrogen and about two thirds of solar helium were made during the prestellar phases of the Universe, perhaps together with some of the low-abundance light elements: lithium, beryllium and boron. All the other elements are constantly produced by nuclear processes occurring in stars.

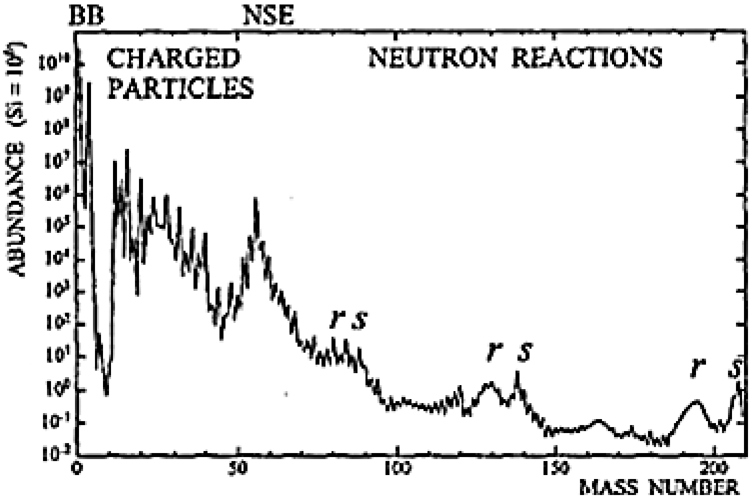

Figure 1.1 The isotopic abundance distribution in the solar system . (Picture from[11])

Major constraints to the theories of the origin of the elements are set by the distribution of their abundances in the solar system, which is shown in Fig. 1.1. This distribution displays several important features, such as the various peaks corresponding to the abundances of several elements, which helped in the identification and early description of the nuclear processes that could be responsible for their production. The theories of the nucleosynthesis are intertwined with theories of nuclear structure as it was soon recognized that the features observed in the solar system distribution of abundances are related to the nuclear properties of each element. For example, the abundances of nuclei around Fe are higher than those of the other elements from S to Pb, which is related to the fact that elements belonging to the “Fe peak” have very stable nuclear structures.

The basics of the nucleosynthesis occurring in stars were set in 1957 by the work of Burbidge, Burbidge, Fowler and Hoyle [1]. The classification of nucleosynthesis processes into eight types as proposed by these authors is still mostly valid today and it is summarized in Table 1.1, where each process is associated with its product nuclei and the typical temperature and site where it occurs. Note that in some cases, such as for the r and the p-process, it is still much disputed in which astrophysical site these processes occur.

Table 1.1 The seven types of nucleosynthesis processes

name	products	T (K)	Site
H burning	He, some isotopes of C, N, O, Ne and Na	**>10^6**	Main sequence and red giant stars
He burning	^{12}C and ^{16}O	**~ 10^8**	Red giant star
α process (C, Ne, O burning)	Ne to S, nuclei with A= integer x 4	**~ 10^9**	Evolved massive stars, supernovae
e process (Si burning)	Iron-peak species	**~ 5 x 10^9**	Supernovae
s process	Almost half of the elements heavier than Fe	**~ 10^8**	Red giant stars, evolved massive stars
r process	Almost half of the elements heavier than Fe	**~ 10^9**	Supernovae, neutron stars, ?
p process	p-rich isotopes of the elements heavier than Fe	**~10^9**	Supernovae,?

1.2 Stellar evolution

The classification of stars, clouds of gas massive enough to have nuclear reactions and to be bound by gravitational attraction, is made by means of the Hertzsprung-Russell diagram, where the luminosity or brightness of a star is plotted against its surface temperature.

In Fig. 1.2 a Hertzsprung-Russell diagram is shown from a sample of 22,000 stars in the solar system neighborhood. The surface temperature increases from right to left in the figure. The vast majority of the stars occupy the Main Sequence (MS), stretching diagonally from the upper left (hot and bright stars) to the lower right (cool and faint stars).

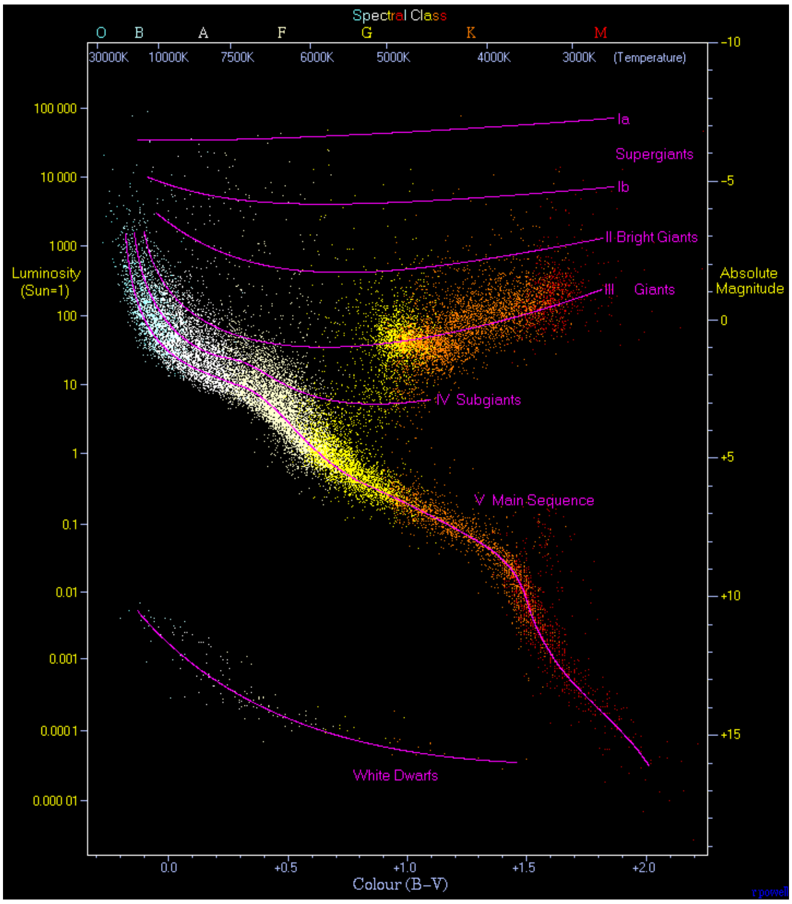

Figure 1.2 Observational Hertzsprung-Russell diagram showing visual magnitude versus surface temperature (top) or color index B (bottom). Each dot corresponds to a star. A sample of 22,000 stars is plotted. The stars tend to fall only into certain regions on the diagram. The most predominant is the diagonal, going from the upper-left (hot and bright) to the lower-right (cooler and less bright), called Main Sequence. In the lower-left region the white dwarfs are found, and above the main sequence are the subgiants, giants and supergiants.(Picture from http://www.atlasoftheuniverse.com/hr.html)

One of the most important goals of the theory of the stellar structure and evolution is to understand why certain stars appear only in specific regions of the diagram and how they evolve from one region to another.

Theoretical models of stars in hydrostatic equilibrium are constructed in the simplest case by solving a set of four partial differential equations (for radius, luminosity, pressure, and temperature) that describe the structure of a star as a function of the distance from the center and as a function of time. A time sequence of such solutions, or stellar models, represents an evolutionary track in the Hertzsprung-Russell diagram. Stellar structure and evolution calculations rely heavily on large scale numerical computer codes. The time changes in the stellar properties are closely related to the energy balance. Energy is generated by the star via nuclear reactions and gravitational contraction, while energy is continuously lost from the stellar surface via emission of photons and neutrinos. A star spends most of its nuclear burning time fusing hydrogen to helium on the MS. Careful observation showed that there is a direct correlation between the mass and the luminosity of a main sequence star. The greater the total mass of the star, the higher the temperature in the core, the faster nuclear energy is generated, and the greater the energy output or the luminosity of the star. For example, a 10 M_{Θ} (10 solar mass) MS star has 3000 times the luminosity of the Sun. Furthermore, the main-sequence lifetime will also depend strongly on the stellar mass because a star burns the nuclear fuel at a rate that is determined by its luminosity. For example stars with masses of 1 M_{Θ}, 5 M_{Θ}, and 15 M_{Θ} spend about 10 Gy, 100 My, and 12 My, respectively, on the main sequence. Once the star leaves the main sequence, the evolution speeds up significantly.

Modern theories have been enormously successful in describing the properties of stars. Nevertheless, many questions remain unsolved, reflecting an incomplete knowledge of certain processes in stars, including the treatment of energy transport via convection, mass loss, atomic diffusion, turbulent mixing, rotation, and magnetic fields. Nuclear physics is deeply intertwined with these issues, and it is worthwhile to keep in mind that nucleosynthesis refers only to one piece in a complex puzzle. One of the main goals of astrophysics is to better understand the inner working of stars. To this aim, a reliable knowledge of nuclear physics is indispensable.

In Table 1.2 the main evolutionary phases for a single star of various initial masses is reported. The stellar masses are shown on the left-hand side and time increases from left to right.

Table 1.2 Major evolutionary stages for single stars in different mass ranges. The initial stellar mass is given on the left-hand side. Time increases from left to right. The nuclear fuel in each burning phase is shown in bold, i.e. H-C refers to hydrogen burning in the core, He-S denotes helium burning in the shell. DU denotes the different dredge-up events (the meaning of dredge-up will be seen further in this paragraph). The labels are: CC for core collapse, SN for supernovae, NS neutron star, and BH black hole. (Table from [12])

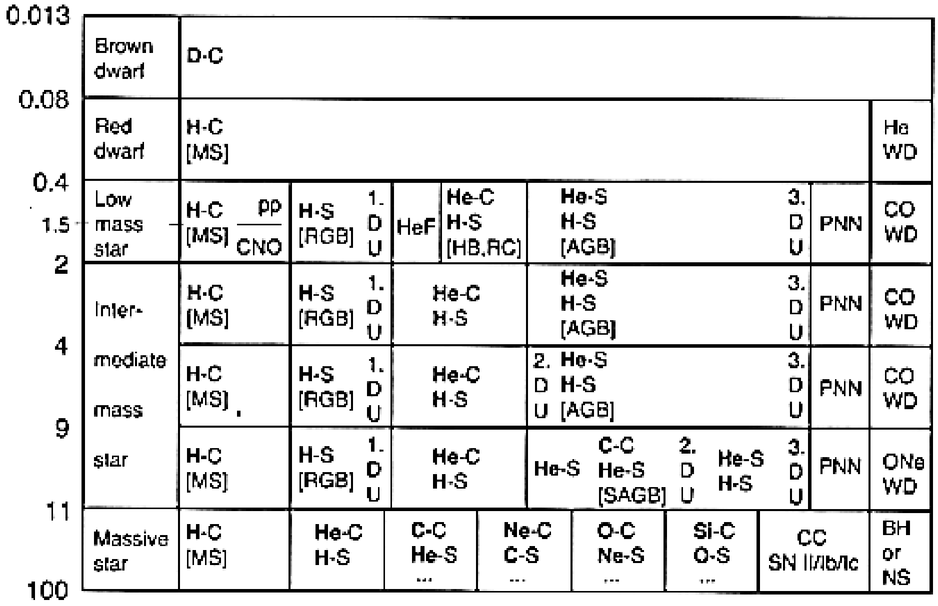

0.013 0.08	Brown dwarf	D-C								
0.08 0.4	Red dwarf	H-C [MS]								He WD
0.4 1.5 2	Low mass star	H-C [MS] pp/CNO	H-S [RGB]	1. D U	HeF	He-C H-S [HB,RC]	He-S H-S [AGB]	3. D U	PNN	CO WD
2 4	Inter-mediate mass star	H-C [MS]	H-S [RGB]	1. D U	He-C H-S		He-S H-S [AGB]	3. D U	PNN	CO WD
4 9		H-C [MS]	H-S [RGB]	1. D U	He-C H-S		2. DU He-S H-S [AGB]	3. D U	PNN	CO WD
9 11		H-C [MS]	H-S [RGB]	1. D U	He-C H-S		He-S C-C He-S [SAGB] 2. DU He-S H-S	3. D U	PNN	ONe WD
11 100	Massive star	H-C [MS]	He-C H-S	C-C He-S ...	Ne-C C-S ...	O-C Ne-S ...	Si-C O-S ...	CC SN II/Ib/Ic		BH or NS

After a first phase where the interstellar gas cloud, consisting mainly of hydrogen and helium, contracts and the gravitational potential energy is transformed into thermal energy and into radiation, the star temperature increases, and reaches 10^5 K. At this temperature the primordial deuterium starts to fuse with hydrogen, a process called deuterium burning, and primordial lithium may be destroyed via interactions with protons. When the temperature reaches several million degrees Kelvin, the fusion of hydrogen to helium starts to occur and contributes with an increasing fraction to the total energy output. At this point the hydrogen fusion in the core becomes the only source of energy, the star is in hydrostatic and thermal equilibrium and has reached the main sequence in the Hertzsprung-Russell diagram which is referred to as zero age main sequence (ZAMS). This first phase is common to all the stars independently of the initial mass, only the time in which the ZAMS is reached is different. The subsequent fate of stars depends strongly on their initial mass, as can be seen from Table 1.2.

Depending on the initial mass (left side of the table) they have a different evolution. In the following a brief description of the evolution for different masses is given, lingering on the mass range more interesting for the nucleosyntesis of the heavier elements.

1.2.1 Initial mass of $0.013\ \mathrm{M}_{\odot} \leq \mathrm{M} \leq 0.08\ \mathrm{M}_{\odot}$

These objects are not real stars, they are called brown dwarfs. They are too small to reach the central temperatures required to sustain hydrogen fusion in their core but they have enough mass to undergo deuterium burning, a fact that sets them apart from massive planets. The search for these very faint and cool “stars” provides important constraints for stellar evolution theory. They are very abundant in the Galaxy and are, therefore, candidates for the elusive (baryonic) dark matter.

1.2.2 Initial mass of 0.08 $M_\Theta \leq M \leq 0.4 M_\Theta$

These stars have sufficient mass to fuse hydrogen to helium in their cores via the pp chain; they are referred to as red dwarfs (or M dwarfs). Starting from the zero age main sequence, the red dwarfs evolve towards higher luminosity and increasing surface temperature (up and left in the Hertzsprung-Russell plot); they run out of nuclear fuel when all the hydrogen is converted in helium. These stars do not have enough mass to reach the temperature required to fuse helium nuclei. They become helium white dwarfs that cool slowly by radiating away their thermal energy.

1.2.3 Initial mass of 0.4 $M_\Theta \leq M \leq 3 M_\Theta$

The evolution of the stars in this mass range is more complicated compared to the previous cases but they are the most important site for the nucleosyntesis of the elements heavier than Fe. The theoretical evolution in the Hertzsprung-Russell diagram of a star of 2 M_Θ and metallicity[1] [Fe/H] = 0 from the pre-main sequence to the AGB phase is shown in Fig 1.3.

---

[1] In astronomy and physical cosmology, the metallicity of a star is the proportion of its matter made up of chemical elements other than hydrogen and helium. The metallicity is often expressed as [Fe/H], which represents the logarithm of the ratio of a star's iron abundance compared to that of the Sun ($[Fe/H] = log_{10}(\frac{N_{Fe}}{N_H})_{star} - log_{10}(\frac{N_{Fe}}{N_H})_{sun}$, where N_{Fe} and N_H is the number of iron and hydrogen atoms per unit of volume respectively).

The way the hydrogen fuses to helium depends on the mass. For stars with masses below 1.6 $M_{\odot}$ hydrogen fusion proceeds via pp chains, while more massive stars burn hydrogen via CNO cycles.

These different processes affect the stellar structure since they possess very different temperature dependences, particularly for stars with $M < 1.5\ M_{\odot}$ the energy generated in the core is transported via radiation while for more massive star the core transports energy via convection.

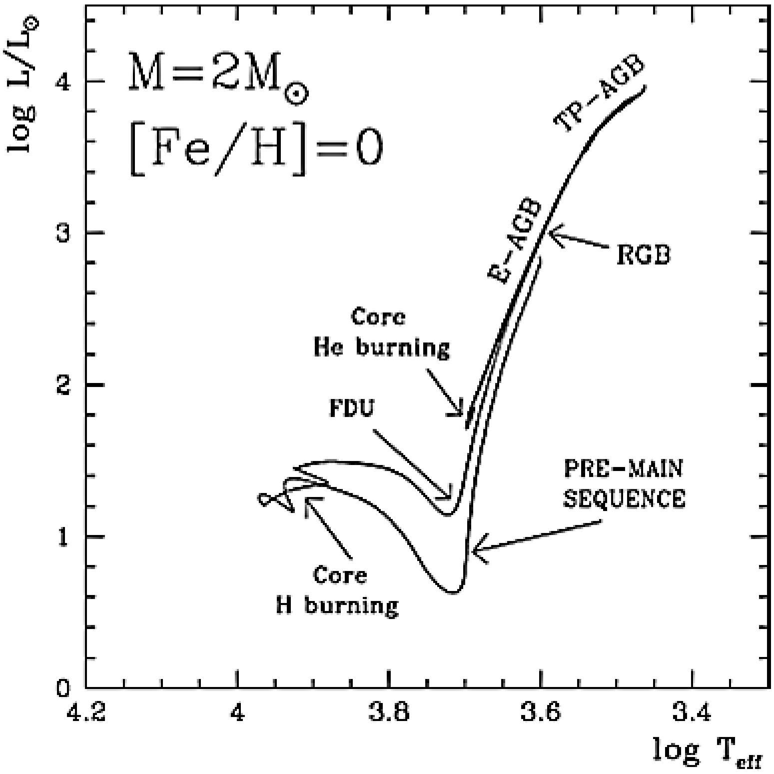

Figura 1.3 Hertzsprung-Russell diagram, in which the stellar luminosity (on a Log_{10} scale) is plotted as a function of the effective (i.e. surface) temperature also in (Log_{10} scale) and decreasing to the right, showing the theoretical evolution of a star of initial $M = 2M_{\odot}$ and solar metallicity. The label FDU is for first dredge up, RGB is for red giant branch, E-AGB if for early Asymptotic Giant Branch, TP-AGB is for thermally pulsing Asymptotic Giant Branch[13].The meaning of dredge up will be explained further in this paragraph.

The main sequence for these stars last about 9 Gy. When the hydrogen in the core is exhausted, the hydrogen fusion continues in a thick layer near the core where hydrogen is still left. At this point the star leaves the main sequence and experiences a contraction in order to generate energy since it is no longer provided by the nuclear processes. This contraction causes further heating and as a consequence, the temperature of the hydrogen burning shell, and the associated nuclear energy generation rate, also increases. The extra energy output from the hydrogen burning shell results in a surface expansion; at this point the star becomes a red giant star. While the star ascends to the red giant branch (RGB) the luminosity increases continuously and the convective envelope deepens significantly until it comprises about 75% of the star’s mass. This deep convective envelope dredges up the products of hydrogen burning from the outer core. The process is referred to as the first dredge-up (FDU). While the conventional envelope expands outwards, its bottom border reaches down to inner regions of the star, where the temperature has been high enough during the main sequence to change the composition of several isotopes via proton capture.

At the point, labeled Core helium burning in Fig 1.3, He starts burning in the center. Because the temperature increases very fast from values at which He does not burn (below $\simeq 1 \times 10^8$ K) to $\simeq 2 \times 10^8$ K, where He burning is very efficient, and because the energy production for the 3α reaction has a strong dependence on the temperature ($\sim T^{40}$), the huge and sudden energy release drives a central convective zone, which almost reaches the location of the H-burning shell. A central source of energy tends to move the star back towards the main sequence region, with higher effective temperatures, while the presence of two energy sources (core He burning and H shell burning) brings the star towards lower luminosities. When the

He is also exhausted in the center, He-burning starts in a shell around the core, now degenerate and rich in C and O produced by complete He burning. The structure completes the loop coming back close to point labeled Core helium burning in the Fig 1.3, and the star ascends to the Asymptotic Giant Branch. This is called so because the evolutionary track at this point approaches the first giant branch almost asymptotically.

The AGB evolution is divided into two phases: the early-AGB (E-AGB) and the thermally pulsing AGB (TP-AGB). The evolution in time and mass of the points defining the structure of the AGB stars is presented in Fig 1.4, where the evolution of stellar structure is represented as a function of mass.

The structure evolves in a very peculiar way as the H- and He-burning shells are activated alternately. Models have shown that during the AGB phase the H-burning shell dominates the energy production for most of the time. Hydrogen is transformed into He at the top of the He intershell, whose thickness consequently grows. The bottom layers of the intershell are compressed until their temperature and density become high enough that He burning is triggered in an almost explosive way. The thermal pulse (also known as thermal instability, or thermal runway) generated by this sudden release of energy causes the energy transport in the whole He intershell to turn from radiative to convective and the material is mixed and homogenized through-out the region (convective pulse). In the meanwhile the H shell cools and H burning stops. A thermal pulse quenches after a few hundred years and then the H burning starts again. This cycle is repeated 10-100 times with intervals between pulses of the order of 10^3 - 10^5 years. The total number of calculated pulses depends on the initial stellar mass and on the choice of the mass-loss law.

Just after the quenching of a thermal pulse an episode of mixing may occur, known as third dredge-up (TDU), during which a fraction of the material from the He intershell is carried to the envelope, see Fig 1.4. During the thermal pulse partial He burning produces high amounts of carbon in the He intershell. This carbon is then mixed into the envelope by TDU, allowing AGB stars to become carbon rich after a certain number of TDU episodes. Stars for which the surface ratio of carbon to oxygen exceeds unity are called carbon stars.

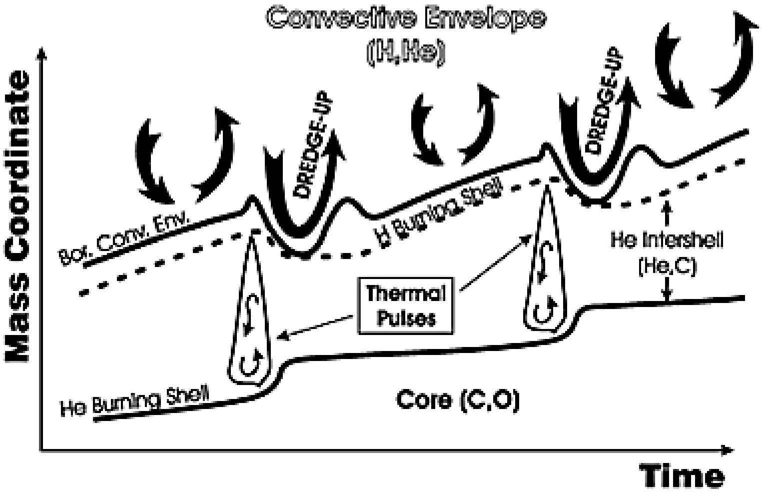

Figure 1.4 Schematic view of the evolution of the position of the inner border of the convective envelope, the hydrogen burning shell and the helium burning shell, during the TP-AGB pase. The convective regions generated by two subsequent thermal pulses are also shown.(Picture from [14])

The star suffers of a significant mass loss on the AGB via a strong stellar wind; thermal pulses are ceasing at this point and the star becomes a post AGB star (P-AGB), with only a fraction of its initial mass left and the other part returned to the interstellar medium. Stars of this mass range end their existence as a white dwarf with a mass of ≈ 0.5 $M_{\odot}$, consisting mainly of carbon and oxygen, they are supported by electron degeneracy pressure and cool slowly by radiating away their thermal energy.

It has to be stressed that the above description of the evolution beyond the red giant branch is rather uncertain because of the lack in knowledge on how to predict convection and mass loss. That these effects occur has been demonstrated by stellar observation, but a deeper understanding is far to come. It is generally accepted that each thermal pulse during the TP-AGB phase provides favorable conditions for another dredge-up episode after the end of flash-burning in the helium shell. The convective envelope reaches deep into the star below the bottom of the hydrogen burning shell and carries the products from the hydrogen and helium shell burning, in particular helium and carbon, to the stellar surface. The AGB stars, as will be discussed later, are the sites where nuclides with mass number beyond A ≈ 60 are created. Stellar models predict that these (s-process) nuclei are also dredged up to the surface where they can be observed in stellar atmosphere. The observation of radioactive technetium in certain (S-type) carbon stars was a strong support for these models.

1.2.4 Initial mass of $3\ M_\Theta \leq M \leq 11\ M_\Theta$

The stars in this mass range do not contribute to the s-process element production. This mass range can be divided in several sub-ranges. Stars with initial masses of $3\ M_\Theta \leq M \leq 4\ M_\Theta$ evolve through the same stages as stars in the range $0.4\ M_\Theta \leq M \leq 3\ M_\Theta$, the major difference arises from the fact that for a star with $M \geq 3\ M_\Theta$ the helium core during the RGB phase does not become electron degenerate. Therefore, a helium flash does not occur but instead helium ignites quiescently in the center.

Stars with masses $M \geq 4\ M_{\Theta}$ experience an additional episode of mixing. Following helium exhaustion in the core, the structural readjustment to helium shell burning results in a strong expansion, such that the hydrogen burning shell is extinguished as the star begins to ascend the early asymptotic giant branch. At this time the inner edge of the convective envelope penetrates the dormant hydrogen shell, and the products of hydrogen burning are mixed to the surface. This process is referred to as second dredge-up (SDU). Afterwards, the hydrogen shell reignites and the star continues to evolve up to the AGB.

1.2.5 Initial mass of $M \geq 11\ M_{\Theta}$

The evolution of stars in this mass range is in many ways fundamentally different compared to our earlier discussion. The total life of such massive stars is relatively short, about 9 My, and the stars spend 90% of the time in the main sequence, burning hydrogen to helium via the CNO cycle in the core. When the hydrogen in the core is exhausted, hydrogen burning continues in the shell. The core contracts and heats up until helium is ignited. This new source of nuclear energy heats the overlying hydrogen shell and the outer layers of the star expand greatly. The star becomes a super giant.

Core helium burning lasts for about 800,000 years and some of the heavy nuclides with $A > 60$ are synthesized during this stage via neutron capture (s-process). When helium is exhausted in the center, helium burning continues in a shell beneath the hydrogen burning shell.

The stars in this mass range are able to ignite successive burning stages in their core using the ashes of the previous core burning stage as fuel. Three distinct burning stages follow carbon burning: neon burning, oxygen burning, silicon burning.

There is a fundamental difference between the last three stages and the initial ones in the manner by which the energy generated in the stellar interior is transformed and radiated from the surface. In the initial stage, hydrogen and helium burning, the nuclear energy is mostly converted into light, in the latest stages it is almost entirely radiated as neutron-antineutrino pairs.

The approximate structure of the massive star after the silicon has been exhausted in the core is shown in Fig 1.5. The star consists of several layers of different composition that are separated by thin nuclear burning shells. This star will end its life as a supernova.

The electron degenerate stellar core has at this point no other source of nuclear energy to its disposal and grows in mass as the overlying burning shells contribute nuclear ashes. When the mass of the core exceeds the Chandrasekhar limit ($\approx 1.4\ M_{\odot}$), the electron degeneracy pressure is unable to counteract gravity, and the core collapses. When the density reaches values of the order of nuclear density ($\approx 10^{14}$ g/cm^3), the nuclei and free nucleons begin to feel the short-range repulsive nuclear force. The inner collapsing core reaches high inward velocities and overshoots the nuclear density. The nuclear potential acts as a stiff spring that stores energy in the compressive phase until it rebounds. The rebounding part of the core encounters falling matter and thus gives rise to an outward moving shock wave.

How exactly the shock wave propagates through the stellar layers beyond the iron core and disrupt the star in a core collapse supernova explosion is still unknown. Nevertheless many species are created in this phase; in particular, the deepest regions that are ejected are characterized by a large number of free neutrons. These give rise to the nucleosynthesis of many heavy nuclei in the A > 60 mass range via neutron capture (r-process)

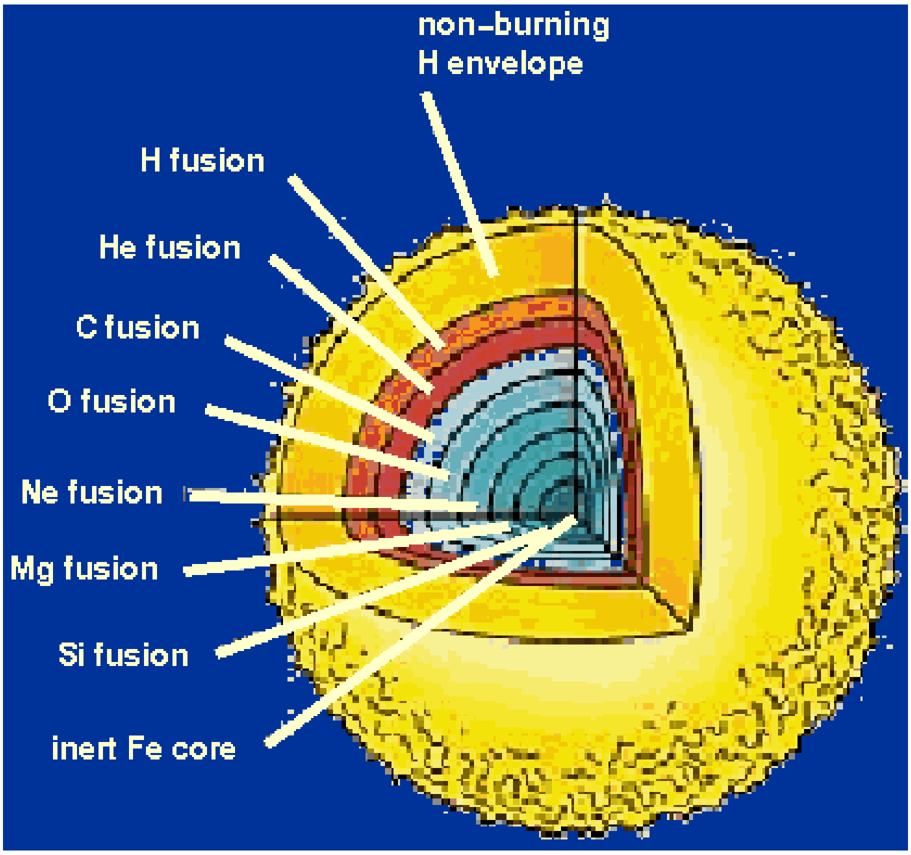

Figure 1.5 Schematic structure of a supernova star (not to scale). The nuclear burning shells are labeled on the lower-left side. This model is sometimes referred to as the “onion shell structure” of a massive star. (Picture from http://www.vikdhillon.staff.shef.ac.uk/teaching/phy213/phy213_highmass.html)

1.3 Nucleosynthesis beyond the iron peak

As described previously the light nuclei ($A < 60$) are built by fusion reactions in the different stages of the stars, but beyond iron the Coulomb barrier is too high for charged particle reactions to occur. For these reasons, charged-particle cross sections are far too small at moderate stellar temperatures to explain the observed solar system abundances of nuclides with masses beyond $A \approx 60$. At this point the neutron will play an important role; indeed there is no Coulomb barrier for them and thus the neutron capture cross sections, even at moderate stellar energies, are often quite large. It is therefore reasonable to assume that heavy nuclides can be synthesized by exposing lighter seed nuclei to a source of neutrons. There is unambiguous evidence for such mechanism; it provides a natural explanation for the fact that the solar system abundance curve, see Fig 1.1, peaks near the mass numbers $A \approx 84$, 138, and 208, corresponding to the magic neutron numbers $N = 50$, 82, and 126, respectively. But free neutrons are unstable, with a $T_{1/2} = 614$ s, therefore a neutron production source is required before such neutron reaction can occur.

The gross property of the solar system abundances in the $A > 60$ range can be accounted for in terms of two extreme pictures, that is, by capture reactions with relatively low neutron density on one side and very high neutron density on the other side.

In the first case the neutron flux is sufficiently small that after a neutron capture the unstable nucleus created has a β-decay constant larger compared to the decay constant of the competing (n,γ) reaction ($\lambda_\beta >> \lambda_{n\gamma}$), in such a way that successive neutron captures by a chain of isotopes occur until a radioactive isotope is reached at which point a β^-decay takes place and another chain of successive isotopes is initiated. The resulting path is shown in Fig. 1.6. This mechanism is referred to as the slow neutron capture process (s-process) [1]. The s-process path runs close to the group of the stable nuclides (β-stability valley), see Fig 1.7.

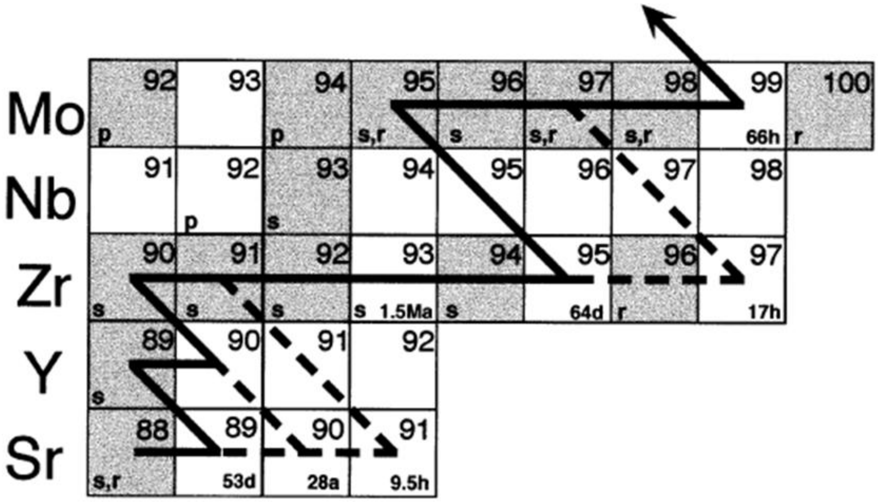

Figure 1.6 The s-process path in the Zr-Mo region of the chart of the nuclides. Stable isotopes are in shaded boxes, β unstable isotopes are indicated by open boxes; the half-lives of some isotopes are shown in the lower right corners. In the lower left corner, the dominant nucleosynthesis processes are indicated.

The abundances synthesized by the s-process will in general depend on the magnitude of the neutron capture cross sections involved in the chain. Nuclei with very small neutron capture cross sections are expected to pile up in abundance, while those with large cross sections will be quickly destroyed and achieve only small abundances.

The other scenario is a neutron flux so large that the decay constant of an unstable nucleus created after neutron capture is small compared to the decay constant of the competing (n,γ) reaction ($\lambda_\beta << \lambda_{n\gamma}$). In this case, the nucleosynthesis path will run close to the neutron dripline. When the neutron flux terminates, all the neutron-rich radioactive nuclei will undergo successive β^{-}–decays along the isobaric chains until the most neutron-rich, stable (or very long-lived) isobar is reached. This nucleosynthesis process is called the rapid neutron capture process (r-process).

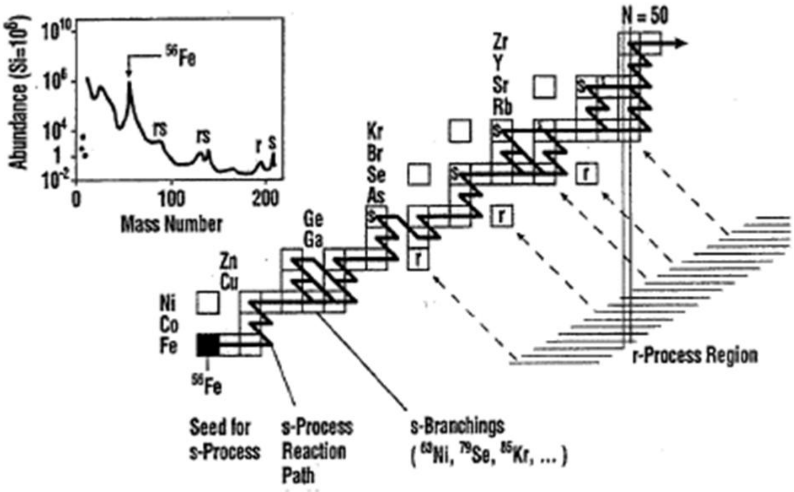

Figure 1.7 An illustration of the neutron capture processes responsible for the formation of the nuclei between iron and the actinides, The observed abundance distribution in the inset shows characteristic twin peaks. These peaks result from the nuclear properties where the s- and r-reaction paths encounter magic neutron numbers. (Picture from[7]).

The neutron density in the s-process is of the order of $N_n \approx 10^8$ cm^{-3}, while for the r-process it is much higher $N_n \approx 10^{21}$ cm^{-3}.

In the following paragraphs a more detailed description of the nucleosynthesis processes will be given.

1.3.1 The s-process

The heaviest nuclei synthesized by charged particle reactions are those of the iron peak. These are the seeds for the neutron captures. The most massive stable nucleus produced by the s-process is ^{209}Bi;

further neutron captures produce radioactive nuclei that decay by α-particle emission, thus ^{209}Bi represents the termination point of the s-process.

In the s-process the majority of the neutron capture reactions involve stable target nuclei, so all these reactions can be reproduced in laboratory.

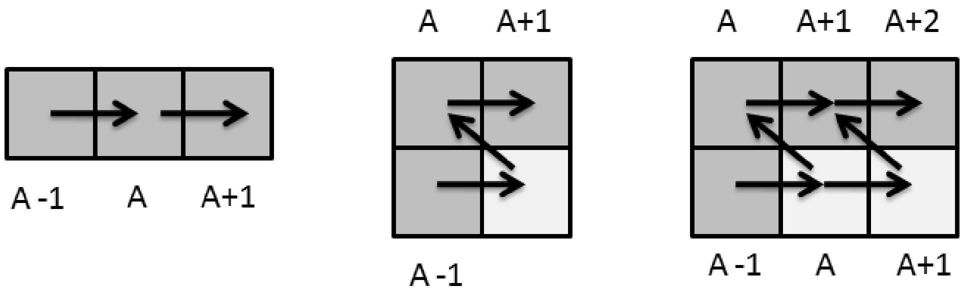

Figure 1.8 Basic building blocks of the s-process path. Stable (or very long-lived) nuclei are shown as shaded squares, short-lived nuclei as open squares. In the left part, the nucleus with mass number A is destroyed by neutron capture and is produced by neutron capture on nucleus A-1. In the central part, nucleus A is again destroyed by neutron capture, but is produced by neutron capture on the nucleus A-1 and the subsequent β^--decay. The right part shows the s-process branching.

Fig 1.8 shows the basic building blocks of the s-process path. The abundance evolution of any stable (or very long-lived) nuclide with mass A is given by

$$\frac{dN_s(A)}{dt} = -N_n N_s(A)\langle\sigma v\rangle_A + N_n N_s(A-1)\langle\sigma v\rangle_{A-1} = \\ -\, destruction\ term + production\ term \qquad [1.1]$$

where $N_s(A)$ and N_n are the abundance of the isotope A and the neutron density and

$$\langle\sigma v\rangle_A = \int_0^\infty v\sigma_A(v)\Phi(v)dv \qquad [1.2]$$

is the reaction rate per particle pair. This is defined as the average value over a Maxwell-Boltzmann velocity distribution $\Phi(v)dv$ of the product of the relative velocity v times the cross section $\sigma_A(v)$. Typically, for neutron captures it is seen that $\sigma_A(v) \propto 1/v$, thus $\langle\sigma v\rangle_A$ is very nearly constant and it is useful to define the Maxwellian-average cross section (MACS) $\langle\sigma\rangle_A$ so that:

$$\langle\sigma\rangle_A v_{th} = \langle\sigma v\rangle_A \qquad [1.3]$$

where $v_{th}$is the thermal velocity. Replacing the time with time-integrated neutron flux, or neutron exposure τ:

$$\tau = \int_0^t N_n v_{th} dt \qquad [1.4]$$

one has:

$$\frac{dN_S(A,\tau)}{d\tau} = N_S(A-1,\tau)\langle\sigma\rangle_{A-1} - N_S(A,\tau)\langle\sigma\rangle_A \qquad [1.5]$$

This last equation attempts to minimize in the sense that it attempts to minimize the difference $N_S(A-1,\tau)\langle\sigma\rangle_{A-1} - N_S(A,\tau)\langle\sigma\rangle_A$. In the mass region between the magic neutron numbers the Maxwellian averaged cross sections are relatively large so that the difference $N_S(A-1,\tau)\langle\sigma\rangle_{A-1} - N_S(A,\tau)\langle\sigma\rangle_A$ becomes much smaller than the magnitude of either product $N_S(A-1,\tau)\langle\sigma\rangle_{A-1}$ or $N_S(A,\tau)\langle\sigma\rangle_A$. In these mass regions, a steady flow is achieved along the s-process path, $dN_s/d\tau \approx 0$, and it is found that

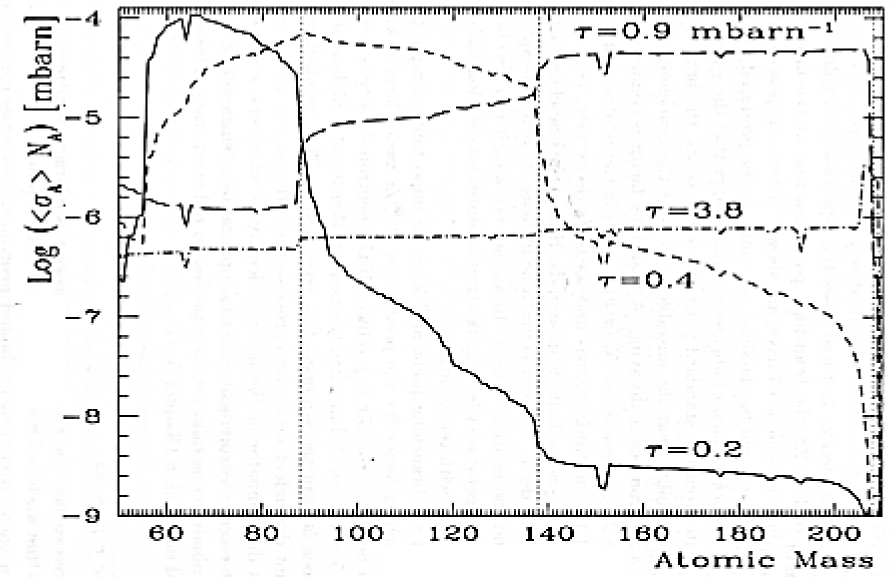

Figure 1.9 The $<\sigma_A>N_A$ distribution produced by the s-process after different neutron exposures as function of the atomic mass A. Neutron-capture cross section values are chosen for a temperature of 8 keV, corresponding to $\simeq 9 \times 10^7$ K. Difference distributions are obtained for different values of the neutron exposure τ, as indicated. Dotted lines are drawn in correspondence to the magic neutron nuclei ^{88}Sr, ^{138}Ba, and ^{208}Pb. Local equilibrium $<\sigma_A>N_A \simeq$ constant is roughly verified far from nuclei with magic neutron numbers. Higher neutron exposures produce heavier nuclei as the bottlenecks at magic neutron numbers are more easily bypassed. (Picture from[14])

$$N_S(A-1,\tau)\langle\sigma\rangle_{A-1} \approx N_S(A,\tau)\langle\sigma\rangle_A \quad \text{or} \quad N_S(A,\tau)\langle\sigma\rangle_A \approx const \qquad [1.6]$$

This result is called local (equilibrium) approximation since it is only satisfied locally in the region between magic neutron numbers. The small cross sections of the magic neutron nuclei represent bottlenecks for a continuous abundance flow of the s-process since the total neutron exposure τ is not infinite. As a consequence, $N_S(A,\tau)\langle\sigma\rangle_A$ is not ≈ constant over the whole distribution but characterized by steps occurring at the magic neutron nuclei as shown in Figs 1.9 and 2.1.

So far it was explicitly assumed that all neutron capture rates on unstable nuclei are either much faster ($\lambda_\beta \ll \lambda_{n\gamma}$) or much slower ($\lambda_\beta \gg \lambda_{n\gamma}$) than the competing β-decays.

At certain locations along the s-process path, however, the abundance flow encounters unstable nuclei with unusual β^--decay constants (half-lives) that are comparable in magnitude to the competing neutron capture rate, $\lambda_\beta \approx \lambda_{n\gamma}$. At these locations the s-process path splits into two branches. The branching factor is the probability that the unstable nucleus at the branching point will capture a neutron before decaying and is computed as

$$f_n = \frac{\lambda_n}{(\lambda_n + \lambda_\beta)} \qquad [1.7]$$

where $\lambda_n = N_n\langle\sigma(v)v\rangle$, $\sigma(v)$ is the neutron-capture cross section of the unstable nucleus and λ_β is the decay rate, i.e. $\lambda_\beta = ln2/T_{1/2}$, where $T_{1/2}$ is the half life in seconds. In an indirect way, it can also be a function of the temperature when the neutron-capture cross section and/or the decay rate vary with temperature.

Fig 1.10 shows the branching paths starting at the unstable nucleus ^{95}Zr, which is an important example because the branching factor for the production of ^{96}Zr varies largely with the neutron density. No ^{96}Zr is produced if the neutron density is lower than about 5×10^8 cm^{-3}, but when the neutron density is as high as 10^{10} cm^{-3}, up to 50% of the s-process flux goes through ^{96}Zr, producing it in an amount dependent on its cross section. Hence, the abundance of ^{96}Zr is a discriminator of the neutron density at which the *s*-process occurs.

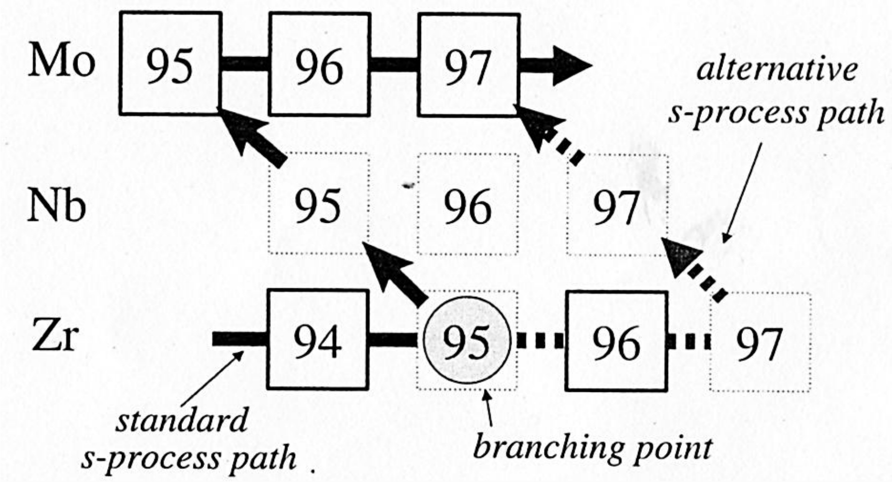

Figure 1.10 Section of the nuclide chart showing the branching path that is open in ^{95}Zr in conditions of high neutron density. When the branching is open, part of the flux goes through ^{96}Zr, skipping ^{95}Mo and ^{96}Mo. (Picture from [14])

1.3.2 Explosive scenarios and the p nuclei

While s-process nucleosynthesis accounts for about one half of the heavy element abundances, the other half is provided by processes occurring under explosive conditions, predominately in supernovae. The very high temperatures and densities in the nucleosynthesis zone result in reaction time scales which are much shorter than those for β-decay. Accordingly, explosive nucleosynthesis involves reactions on unstable and fairly short-lived nuclei which are difficult to study in the laboratory. Therefore, nuclear theory must be involved for extrapolating the relevant properties of the known isotopes to the reaction paths far from stability. In addition to this uncertainty, the hydrodynamics of the explosion represents a difficult problem in itself. The attempt to reproduce the observed abundance patterns can provide important clues for supernova models

1.3.2.1 The r-process

The r process is characterized by very high neutron densities so that nuclei with a very large number of neutrons are produced.

However, for each given element, bound neutron-rich isotopes can be found with a number of neutrons above which it is not possible to capture another neutron because no energy states exist for which the neutron can be bound to the nucleus; in a N – Z diagram this results in a line, the so-called neutron dripline. During the *r*-process, when nuclei with numbers of neutrons at the neutron dripline are abundant, an equilibrium between neutron-capture (n,γ) and inverse photodisintegration (γ,n) reactions is established. At that point the β^--decay reactions also start playing a role, since isotopes with high numbers of neutrons β^- -decay very quickly, with half-lives typically of the order of seconds. Models of the r-process have to include a very large number of unstable isotopes. The properties of these nuclei, such as neutron-capture cross sections and β-decay rates are difficult to measure and are usually calculated by theoretical nuclear models.

For the majority of the heavy nuclides both the s-process and the r-process contribute to the observed abundance.

But as indicated in Fig. 1.7, there are neutron-rich stable isotopes (marked r in the figure) that are not reached by the s-process because of their short-lived neighbors. Consequently, these species are of pure r-process origin. In turn, these r-only nuclei terminate the β-decay chains from the r-process region, making their stable isobars an ensemble of s-only isotopes. The existence of these two subgroups is of vital importance for nucleosynthesis, since the credibility of any model depends on how well the abundances of these particular nuclei can be reproduced

. Therefore one may calculate the solar system r-process abundance by subtracting the s-process contribution calculated by classic or stellar models, see § 2.2 and § 2.3, from the total solar system abundance of a given nuclide ${}^{A}_{Z}X$.

$$N_r(A,Z) = N_{\odot}(A,Z) - N_S(A,Z) \qquad [1.8]$$

The resulting $N_r$values versus mass number A are shown in Fig 1.11. It can be seen that the distribution of solar system r-process abundances is rather smooth and it is consistent with the abundances of the r-only nuclides which are shown as solid circles. The most outstanding features on Fig 1.11 are the two pronounced peaks at mass numbers A=130 and 195. The existence of the r-process abundance peaks and of the long-lived radioisotopes ^{232}Th($T_{1/2} = 1.4 \times 10^{10}$ y), ^{235}U($T_{1/2}$=7.0×10^{8} y) and ^{238}U($T_{1/2} = 4.5 \times 10^{9}$ y), located beyond the endpoint of the s–process, provide the strongest evidence for the occurrence of a neutron-induced process that is quite different from the *s*-process. The solar system r-process abundance distribution represents a strong constraint for models of the *r*-process.

The explanation of the r-process abundances peaks in Fig 1.11 is that, like for the s-process, they are caused by the magic neutron numbers N = 50, 82, and 126. These magic neutron nuclides are proton deficient compared to their counterparts produced in the *s*-process which are located close to the stability valley. In the *r*-process the large neutron flux drives the matter to the neutron-rich side, far away from the stability valley. After termination of the neutron flux, these neutron magic nuclei undergo a sequence of β^{-}-decays along an isobaric chain (A=constant), until the most neutron rich stable (or very long-lived) isobaric is reached.

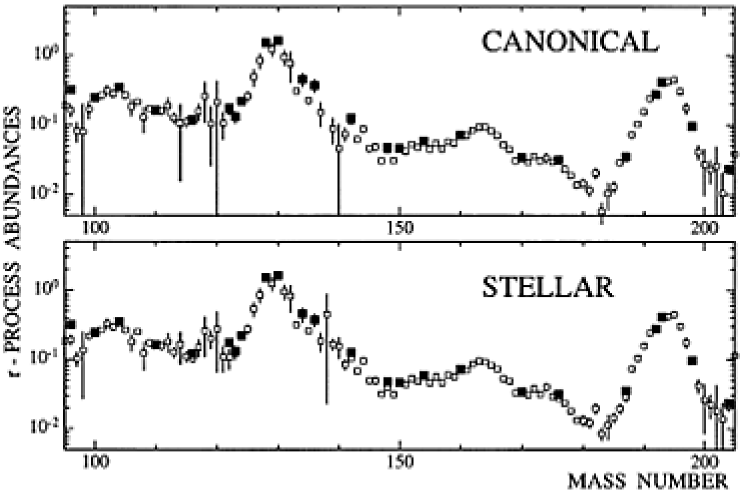

Figure 1.11 Solar system r-process abundances for A > 90, obtained by subtraction of the s-process contribution, obtained for the classical (canonical) and the stellar model, from the total solar system abundance. The full circles show abundances of r-only nuclides, defined here as those species for which the s-process contribution amounts to < 3%. (Picture from[8]).

Consequently, the *r*-process produces abundance maxima in mass regions located below the corresponding *s*-process abundances peak. It is important to note that the observed abundances of the *r*-process nuclides are not correlated with their neutron-capture cross sections, contrary to the case for *s*-process abundances. Rather, the observed r-process abundances reflect the nuclear properties of radioactive progenitors on the neutron rich side far away from the stability valley.

The modeling of the r-process is challenging not only in the nuclear physics involved, but also with respect to the site where it could occur, for a detailed review see Ref [15]. Possible sites for the r-process are the type II supernova explosions, in particular at the time when, as the temperature drops, material freezes out from nuclear statistical equilibrium, or neutron stars, where neutron-rich nuclei can be present together with free neutrons in degenerate conditions.

There are also situations in which the *r*-process products are of secondary nature, i.e. the seed nuclei were initially present in the stellar site where the production of heavy elements occurs. In these cases the r-process is unrelated to statistical equilibrium and the neutrons are produced by α-capture reactions as $^{13}C(\alpha,n)^{16}O$, $^{22}Ne(\alpha,n)^{25}Mg$ and $^{25}Mg(\alpha,n)^{28}Si$, which occur at temperatures lower than about one billion degrees, at which statistical equilibrium has not set in. Another possible site for the r-process has been identified in the neutrino-driven winds of a neutron star that is forming just after a type II supernova explosion.

All these scenarios described above present unresolved problems in trying to match the solar r-process abundance distribution.

1.3.2.2 The p-process

The very neutron deficient, stable nuclides with mass numbers of $A \geq 74$ (between ^{74}Se and ^{196}Hg) are bypassed by the s- and r-process. These species are referred to as p-only nuclei, where the letter p designates the fact that they contain more protons relative to the other stable isotopes of the same elements. The mechanism responsible for the synthesis of the p-nuclei is called p-process.

These nuclei have very low abundances in the solar system with respect to other stable nuclei of the same elements. For example the abundances of the p-only nuclei ^{136}Ce and ^{138}Ce represent only 0.19% and 0.25%, respectively, of Ce in the Solar System. However there are a few p-only nuclei that are exceptions to this rule: ^{92}Mo and ^{94}Mo, which represent 15% and 9%, respectively, of the total abundance of molybdenum, and ^{96}Ru and ^{144}Sm, which represent 5% of the total abundance of ruthenium and samarium, respectively.

The production of the p-only nuclei can be ascribed to proton captures or to disintegration processes. In both cases these nuclei are produced starting from material already enriched in heavy elements (produced in the s- or r- process). For proton capture, the scenario could be similar to that applicable to the r-process in relation to the nuclear statistical equilibrium: in the case of r-process the material freezing out from equilibrium must be neutron rich, in the case of p-process the material must be proton rich. In this situation the production of proton-rich nuclei by proton captures is balanced by disintegration reactions (γ, n) and β^+-decays of unstable nuclei. In the alternative scenario, proton-rich nuclei are produced by disintegration of heavier elements. Within the disintegration scenario it is possible in principle to explain why ^{92}Mo and ^{144}Sm are more abundant with respect to other p-only nuclei: these two p-only isotopes have a magic neutron number (N = 52 and 80, respectively) hence their (γ,n) disintegration rates are small and they act as bottlenecks when disintegration processes are at work.

As in the case of r-process, laboratory β-decay rate measurements are crucial to the modeling of the p-process.

The p-only nuclei can be produced in different sites, such as type II supernova explosions, supernova-driven accretion disks around neutron stars, and also type Ia supernova explosions.

1.3.2.3 The rp-process

Explosive hydrogen burning on the surface of accreting neutron stars (X-ray buster[2]) can yield abundance contributions up to the Fe group [16,17], the sequence of rapid proton capture being halted at ^{56}Ni due to the strong photodisintegration reaction ^{57}Cu(γ,p)^{56}Ni. However, when sequential two-proton captures ^{56}Ni(2p,γ)^{58}Zn were identified as a plausible possibility to bridge this gap at ^{57}Cu, it was found that the rp-process chain could continue along the $N = Z$ line up to iodine, providing some delayed energy production which may explain the time structure of the actually observed bursts. So far, this situation depends on the yet unknown nuclear physics input. Provided that this can be confirmed and that the ejection efficiency of processed material from the neutron star is high enough, the rp-process could provide an alternative explanation of the excess in the abundances of the light Mo and Ru isotopes, which are difficult to understand via the p-process in supernovae.

---

[2] X-ray bursters are one class of X-ray binary stars exhibiting periodic and rapid increases in luminosity (typically a factor of 10 or greater) peaked in the X-ray regime of the electromagnetic spectrum. These astrophysical systems are composed of an accreting compact object, typically a neutron star or occasionally a black hole.

Chapter II Stellar models

2.1 Introduction

In the previous chapter the stellar evolution and the nucleosynthesis of the elements was described. Almost 50% of the elements beyond the iron peak are synthesized by s-process neutron capture. In this chapter the neutron sources and the stellar model for the s-process will be discussed.

2.2 Classical stellar model

The classical stellar model is the phenomenological s-process model, which was sketched already by B^{2}FH [1] and later by Seeger [2]. The local approximation described in § 1.3.1 is most useful for nuclides with adjacent mass number in the regions between closed neutron shells, but does not hold over the entire A = 56 – 209 mass range. This is clear from Fig 2.1, where the symbols show the product $N_{Ο}(A)\langle\sigma\rangle_A$ versus mass number A for the s-only isotopes. The $N_{Ο}(A)\langle\sigma\rangle_A$ values vary in magnitude by a factor of ≈ 100. First the $N_{Ο}(A)\langle\sigma\rangle_A$ values decrease up to the closed N-shell at A ≈ 84, followed by two lower plateaus governed by local equilibrium. Particularly large variations occur at the boundaries of these plateaus (A ≈ 84, 138 and 208), which correspond to closed neutron shells. It was found [18] that a single neutron exposure would not suffice to explain the observed $N_{Ο}(A)\langle\sigma\rangle_A$ values. A better agreement could been obtained by adopting an exponential distribution of neutron exposures [2]. Such a distribution reflects the physically reasonable assumption of decreased probabilities for increasing neutron exposure, that is, the total exposure experienced by some fraction of material relates to the number of times that material had been processed through successive generations of stars or through successive burning episodes in a specific star.

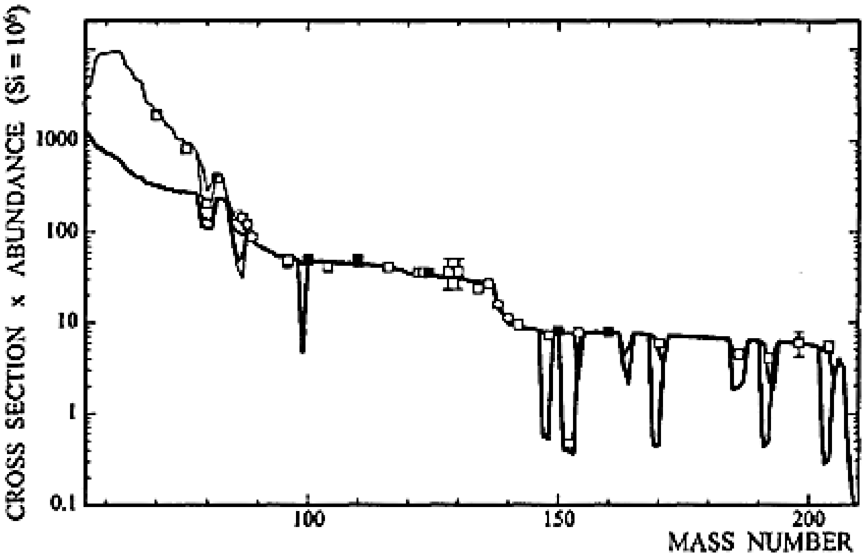

Fig 2.1 The product $N_{\Theta}\langle\sigma\rangle_A$ (in units of millibarn per 10^6 Si atoms) of solar system s-process abundance and Maxwellian-averaged cross section (at thermal energy of kT = 30 keV) versus mass number A. The symbols correspond to s-only nuclides. The solid curves are obtained fitting the data to an expression similar to Eq. (2.1) but which includes the effect of significant s-process branching. The thick solid line is calculated by using a single exponential distribution neutron exposure (main s-process component). For A ≤ 90, the main component falls below the data points and a second distribution (weak s-process component) must be included in the fit (thin solid line). The sharp structures result from s-process branching. (Picture from [7])

In this approach it is empirically assumed that a certain fraction f of the observed ^{56}Fe abundance, $N_s^{seed}(56)$, was irradiated by an exponential distribution of neutron exposures

$$p(\tau) = \frac{f N_s^{seed}(56)}{\tau_0} e^{-\tau/\tau_0} \qquad [2.1]$$

where $p(\tau)d\tau$ is the fraction of ^{56}Fe seed nuclei having received an exposure in the range between τ and $\tau + d\tau$. The parameter τ_0 is the mean neutron exposure and determines how rapidly the exposure distribution falls off.

In this case, an analytical solution can be obtained for the system of coupled differential equations describing the abundance changes along the reaction path from Fe to Bi

$$\frac{dN_s(A)}{d\tau} = \lambda_n(A-1)N_s(A-1) - \left(\lambda_n(A) + \lambda_\beta(A)\right)N_s(A) \qquad [2.2]$$

provided that a possible time dependence of neutron capture rates, $\lambda_n = N_n\langle\sigma\rangle v_T$ is neglected, that is, it is assumed that the temperature and the neutron density N_n, are constant. Then, the product of stellar cross section and resulting s abundance can be given in analytical form:

$$\langle\sigma\rangle_A N_s(A) = \frac{f N_s^{seed}}{\tau_0} \prod_{i=56}^{A} \frac{1}{\left[1 + \frac{1}{\tau_0\langle\sigma\rangle_i}\right]} \qquad [2.3]$$

Once the capture cross sections $\langle\sigma\rangle_A$ are known, a fit of this expression to the observed solar system values of $N_O(A)\langle\sigma\rangle_A$for the s-only nuclides yields the parameters f and τ_0. The magnitude of these parameters, in turn, is important for identifying the sites and the history of s-process nucleosynthesis.

The solid curves in Fig 2.1 are obtained by fitting the data for $N_O(A)\langle\sigma\rangle_A$ with a similar expression. The height and the shape of the steps are sensitive to the magnitude of the mean neutron exposure τ_0, while the fraction acts as an overall scaling factor. The thick solid line is calculated by using a single exponential distribution of neutron exposures. It describes all the observed $N_O(A)\langle\sigma\rangle_A$ values for s-only nuclides in a wide range from A = 90 to A = 205 and is called the main s-process component. The mean square deviation between the thick solid line and the data points in Fig 2.1 amounts to only 3% [19]. This excellent agreement is remarkable in view of the fact that the main component is represented by an exponential distribution of neutron exposures with only the scaling factor and the mean neutron exposure as fitting parameters. The fit gives a value of $f \approx 0.06\%$, where it is assumed that the number of seed nuclei is equal to the solar system abundance of ^{56}Fe, and $\tau_0 \approx 0.3$ mb^{-1} (for Maxwellian averaged cross sections at 30 keV). These results imply that the main s-process component was produced by irradiating only 0.06% of the solar system abundance of ^{56}Fe nuclei with neutrons, while each ^{56}Fe seed nucleus captured on average about 10 neutrons. The averaged neutrons captured per ^{56}Fe seed nucleus is calculated by the following expression :

$$n_c = \frac{\sum_{A=56}^{209}(A-56)N_s(A)}{fN_s^{seed}(56)}$$

$$= \frac{1}{\tau_0}\sum_{A=56}^{209}\frac{(A-56)}{\langle\sigma\rangle_A}\prod_{i=56}^{A}\frac{1}{\left[1+\frac{1}{\tau_0\langle\sigma\rangle_i}\right]} \qquad [2.4]$$

For mass numbers A < 90, the thick solid line falls below the data points. Therefore, a second component is required in order to explain the synthesis of the s-process nuclides in this mass region. It is called the weak s-process component and is shown as the thin solid line in Fig 2.1.This component is fitted with $f \approx 1.6\%$, $\tau_0 \approx 0.07$ mb^{-1} and $n_c \approx 3$ [19], that is, a much lower mean neutron exposure and a much higher fraction of irradiated seed nuclei compared to the main component. In the Pb-Bi mass region a third component is required, since with the two-component model more than 50% of the solar system ^{208}Pb abundance cannot be accounted for. The third component is called the strong s-process component [20], for which the parameters are $f \approx 10^{-4}$ %, $\tau_0 \approx 7$ mb^{-1}, and $n_c \approx 140$ [19]. In this case, the mean neutron exposure is so large that on average about 140 neutrons are captured per seed nucleus in order to convert a very small fraction of ^{56}Fe nuclei to nuclides in the mass region between ^{206}Pb and ^{209}Bi. These three vastly different neutron exposures cannot be obtained in a single astrophysical site, and it is reasonable to assume that different sites are required to explain each of the observed s-process components.

Combining the results obtained from the study of the branching points (neutron density, stellar temperature, stellar density) and from the global fit to the observed $N_{\odot}(A)\langle\sigma\rangle_A$ gives important constraints for stellar models and the identification of the astrophysical sites of the s-process [7].

The empirical *s*-process *classical model* disregards the time dependence of the s-process parameters, such as neutron density and stellar temperature. It provides a satisfactory description of most observed $N_{\odot}(A)\langle\sigma\rangle_A$ values for s-only nuclides over the entire mass region of interest, requiring only relatively small numbers of adjustable parameters. The classical s-process model makes no assumption on the stellar site or the specific reactions which act as neutron sources.

2.3 The thermally pulsing low mass AGB stars model

The shape of the $N_{\Theta}(A)\langle\sigma\rangle_A$ distribution for s-only nuclides is a measure for the total number of neutron captures to which seed nuclei have been subject and, therefore, it contains the global history of the s-process. The composition of the interstellar gas, out of which the solar system formed, reflects a mixture of the ashes of countless stars. The composition has been homogenized by interstellar mixing to the degree where it represents the average rate nucleosynthesis up to the time of solar system formation. The stars providing the sites for the s-process had certainly a range of masses and metallicities. It is clear from these arguments that a single set of parameters derived from the $N_{\Theta}(A)\langle\sigma\rangle_A$distribution does not correspond directly to the properties of any single star. A more sophisticated approach, based on realistic stellar models, is required in order to reproduce all the observed s-process abundances.

In the current stellar model the main s-process component is thought to originate from thermally pulsing, low mass (1.5 - 3 M_{Θ}) AGB stars, § 1.3. In this scenario, some protons are mixed below the H-rich envelope into the top layers of the intershell which consists mainly of ^{4}He (≈ 75% by mass) and ^{12}C (≈ 25% by mass). This occurs after the termination of a thermal pulse at a time when the He-burning shell becomes almost extinct. The star contracts again and the H shell ignites. The protons that are mixed downward initiate the sequence:

$^{12}C(p,\gamma)^{13}N(\beta^{+}\nu)^{13}C(p,\gamma)^{14}N$

giving rise to two separate regions in the intershell that are rich in ^{13}C and ^{14}N and are referred to as ^{13}C pocket and ^{14}N pocket, respectively. When the temperature reaches T ≈ 0.09 GK (or kT ≈ 8 keV), the mean lifetime of ^{13}C versus destruction by the $^{13}C(\alpha,n)^{16}O$ reaction becomes smaller than the time between the two thermal pulses. Hence, neutrons are released within the ^{13}C pocket and are captured by pre-existing seed nuclei (mainly Fe and s-processed material from previous pulses) to produce most of the nuclides in the main component of the s-process. The neutron flux lasts typically ≈ 20000 y and produces locally high neutron exposures (≈ 0.1 mb^{-1}). Since the time scale is long, however, the neutron density remains low ($N_n \approx 10^7$ cm^{-3}). Only a small number of reaction branchings occur since the β^--decay constant exceeds the neutron-capture decay constant in most cases. During this time, ^{13}C is entirely consumed in the thin ^{13}C pocket. The temperature reached in this stage is not sufficient to initiate the $^{14}N(\alpha,\gamma)^{18}O$ reaction. During the H-shell burning, the mass of the intershell increases steadily (and so do temperature and density), up to a point where the He at the bottom of the intershell ignites. This thermal He pulse grows outward until it most reaches the H-burning shell. The large energy release also causes the stellar envelope to expand and extinguishes the H-burning shell. The thermal pulse engulfs the ashes of the H-shell burning. It gives rises to higher temperatures (T ≈ 0.27 GK or kT ≈ 23 keV), initiating the sequence:

$^{14}N(\alpha,\gamma)^{18}F(\beta^+\nu)^{18}O(\alpha,\gamma)^{22}Ne$

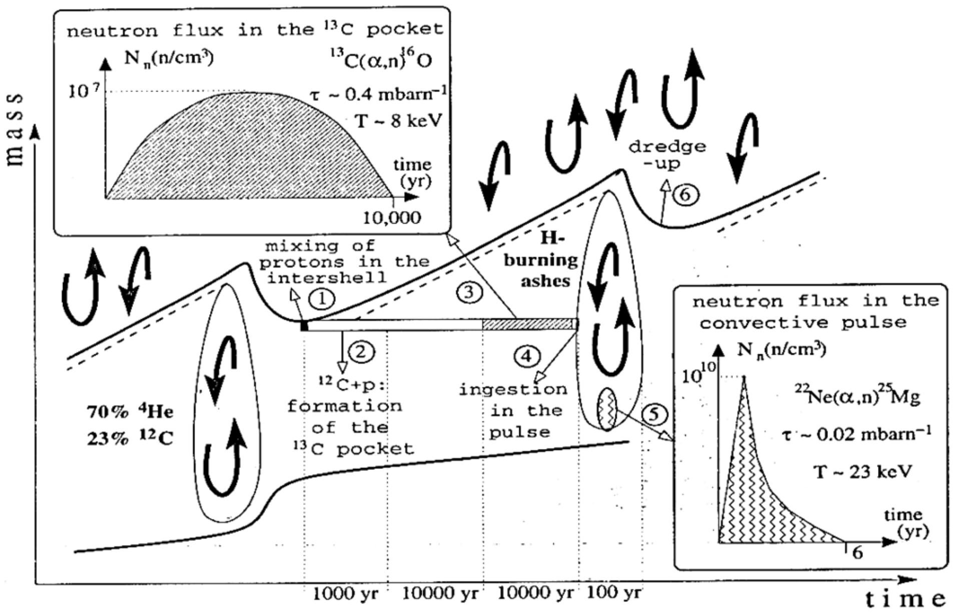

Figure 2.2 Schematic representation of the current model for the s-process in the AGB stars. The six separate mixing and nucleosynthesis phases leading to enrichment of the s-process elements at the stellar surface (1: proton diffusion, 2: ^{13}C production, 3: activation of the ^{13}C neutron source, 4: mixing in the convective pulse, 5: activation of the ^{22}Ne neutron source and 6: third dredge up) are indicated. (picture from [14])

As a consequence, the ^{22}Ne(α,n)^{25}Mg neutron source is (marginally) activated and a second neutron burst occurs. Here, the time scale amounts to a few years, with neutron exposures of ≈ 0.01 mb^{-1} and a peak neutron density of $N_n \approx 10^{10}$ cm^{-3}. This second neutron source does not contribute much to the overall production of the s-process nuclides. It does however influence significantly the s-process branchings which are operating more efficiently at higher temperatures. After a thermal pulse, the He shell becomes inactive, the envelope contracts, and the H shell ignites again. The neutron densities as a function of the time generated by each neutron source are schematically presented in Fig 2.2.

Figure 2.3 demonstrates how well current stellar models of thermally pulsing AGB stars reproduce the solar system abundance distribution of s-process nuclides. Abundances are shown as overproduction factors, that is, as ratios of predicted abundances and corresponding solar system values. The agreement is remarkable, especially in view of the fact that the solar system s-process abundances of the main component must be the products of countless low-mass AGB stars with a range of masses and metallicities. It is also evident that these stars cannot account for the weak s-process component ($A < 90$).

Stellar model studies of thermally pulsing low-mass AGB stars revealed that variations in stellar metallicity have a strong effect on the resulting total neutron exposure. In this scenario, the $^{13}C(\alpha,n)^{16}O$ or $^{22}Ne(\alpha,n)^{25}Mg$ reactions are referred to as primary neutron sources because ^{13}C and ^{14}N (and, hence, ^{22}Ne) are produced in the star itself from the available hydrogen and the ^{12}C. For decreasing metallicity, more neutrons per iron seed nuclei are available from these sources and, consequently, heavier nuclides can be synthesized.

The increased neutron exposure during the s-processing in early generation, metal-poor AGB stars causes an accumulation of material at the end of the s-process path (^{208}Pb and ^{209}Bi). These nuclides provide a natural confirmation for the strong s-process component [21,22].

The weak s-process component is believed to originate from the core He burning stage in massive stars with $M \geq 11\ M_{\odot}$. The ^{14}N nuclei produced by the CNO cycles during the H burning stage are rapidly transformed to ^{22}Ne via $^{14}N(\alpha,\gamma)^{18}F(\beta^{+}\nu)^{18}O(\alpha,\gamma)^{22}Ne$ at the beginning of the He burning stage. But only near helium exhaustion in the core the temperature is sufficient ($T \geq 0.25$ GK or $kT \geq 22$ keV) to ignite the $^{22}Ne(\alpha,n)^{25}Mg$ neutron source.

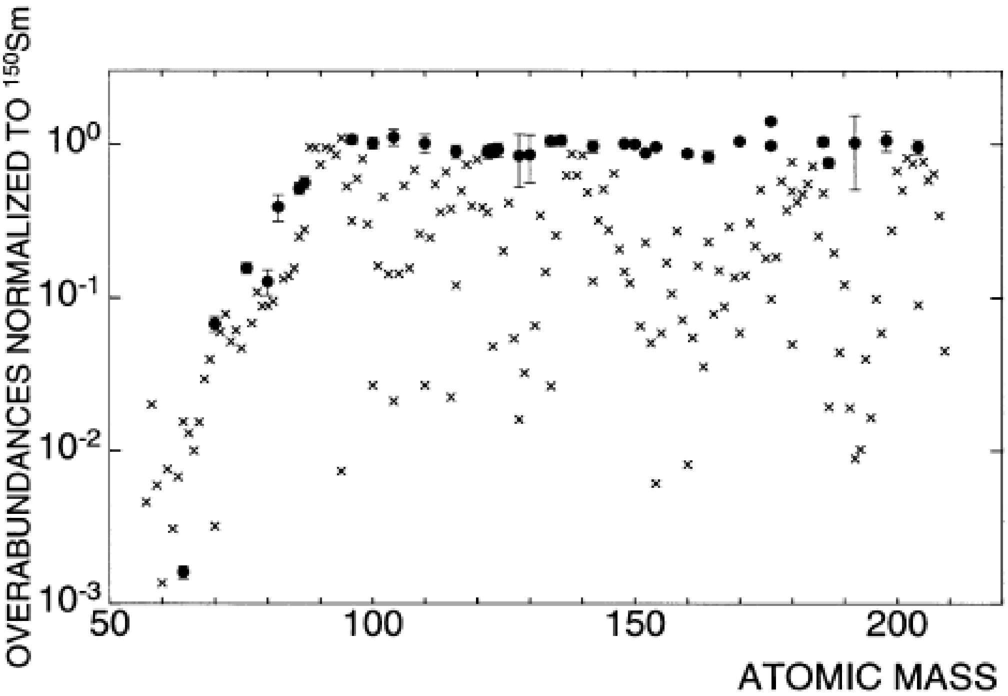

Fig 2.3 Abundance distribution resulting from s-process studies of thermal pulsing AGB stars of mass 1.5 $M_\odot$ and metallicity $Z = 0.01$. Abundances are shown as overproduction factors, that is, as ratios of predicted abundances and the corresponding solar system values, normalized to ^{150}Sm. The solid circles represent the s-only nuclides. Crosses represent all the other nuclides. (Picture from [23])

2.4 Comparison with observations

Another important ingredient in the study of stellar models is the abundances of the elements. In the following section the method used to measure these important quantities will be briefly described.

2.4.1 The surface composition of AGB stars

Since the discovery of s-process Tc by Merrill [10], the atmosphere of the red giants is a fascinating source of information for studies of stars on the AGB. Genuine enrichment by s-process material is common for relatively cool MS, S, and N-type C[3] stars with surface temperature between 2800 and 3800 K, whereas the s enhancements in the hotter Ba stars are meanwhile understood as the result of mass overflow in binary systems [24,25].

Consequently, these MS, S, and C giants can be considered as the only live stars undergoing He shell flashes with concomitant *s*-process nucleosynthesis. Though their low surface temperatures make them difficult to observe, modern observational techniques allow studying the surface composition over a wide range of elements [26]. An impressive example of remarkably detailed analysis based on these observations is the determination of the s-process neutron density for a sample of M, MS, and S giants [27]. In this work, careful measurements of Rb/Sr abundance ratios as well as the isotopic patterns obtained from the ZrO molecular bands were used to constrain the s-process branching of ^{85}Kr and ^{95}Zr. The resulting limits for the neutron density were found to be consistent with the expected value for the ^{13}C(α,n) source, but significantly lower than the predictions for the higher fluxes from the ^{22}Ne(α,n) reaction. This may reflect the gradual increase of the contribution from the ^{22}Ne source along the AGB phase, according to the increase of the temperature in the subsequent convective He shell flashes.

---

[3] In astronomy, stellar classification is a classification of stars based on their spectral characteristics, giving an objective measure of the temperature in the star chromosphere. The M stars are red giant or red dwarf (temperature about 3,000 K), with titanium oxide prominent in their spectra. The C stars (originally known as R and N type stars) are red giants, near the end of their lives, in which there is an excess of carbon in their atmosphere. The Class S stars have zirconium oxide lines in addition to (or, rarely, instead of) those of titanium oxide, and are in between the Class M stars and the carbon stars. The sequence M → MS → S → SC → C-N is believed to be a sequence of increased carbon abundance with age for carbon stars in the AGB.

2.4.2 Isotopic composition of presolar grains

Nucleosynthesis studies normally have to refer to the isotopic abundance distribution of solar material, which is best represented by the composition of primitive meteorites corresponding to that of protosolar nebula [28].

Beyond that representative solar mix, the isolation of the presolar grains from these meteorites is one of the most interesting fields of astronomy. This exciting access to the chemical abundance memories of nature [29,30] has attracted increasing interest from astrophysicists and astronomers. These grains were identified to originate from circumstellar envelopes of mass-losing red giants and from supernova ejecta and have made their way through the interstellar medium without modification. Therefore they contain “pure” s- and r-process material and, hence, represent important probes for these phenomena that allow studying the corresponding nucleosynthesis process in the most direct way.

Silicon carbide is the best studied type of presolar grains, because it occurs as a relatively large grain and it incorporates a number of small impurities which can be used as trace elements. The majority of SiC grains have nuclear abundances suggesting condensation around low-mass (1 or 3 $M_\odot$), thermally pulsing, asymptotic giant branch (TP-AGB) stars.

Aggregates of SiC grains show enrichments in the s-process isotopes of heavy elements [29,31]. Whereas isotope ratios of several light elements (C, N, Mg, Si, Ca, and Ti) have been measured in individual presolar grains, isotope ratios of some elements beyond the Fe peak, Kr, Sr, Xe, Ba, Nd, Sm, and Dy, have been measured only in aggregates of many grains. Each presolar SiC grain may have come from a different star, and grain-size separated aggregates have shown varying degrees of s-process enrichment for Kr, Sr, and Ba. Measurements of the isotopic composition of Si and C in individual SiC grains show large differences from grain to grain, reflecting the unique nucleosynthesis history of each grain.

An illustrative example of how the analysis of the presolar grain can carry very detailed information on the s-process in the AGB phase is given in Fig 2.4. The anomalous Zr patterns shown in Fig 2.4 provide evidence that the neutron density during the s-process exhibits indeed significant variations, which are obvious from the large scatter of the ^{96}Zr component as a result of the branching at A=95.

Fig. 2.4 shows the Zr isotope patterns in function of the mass of 11 single SiC grains (circle) and an aggregate SiC (square) from the Murchisen meteorite, given as δ values (see § 6.32) relative to ^{92}Zr. It is worth to note as each SiC grain has a different pattern, specially for the ^{96}Zr, showing that each grain has a different history. The fit of these analyses to the information obtained from spectroscopy of the AGB star atmospheres allows understanding how the relative contribution from neutron producing reactions on ^{22}Ne and ^{13}C can be traced from the activation of the branching at ^{95}Zr.

Since the anomalous isotope patterns can be measured very precisely, this information has to be complemented by accurate cross section data in order to achieve a full interpretation in an astrophysical sense.

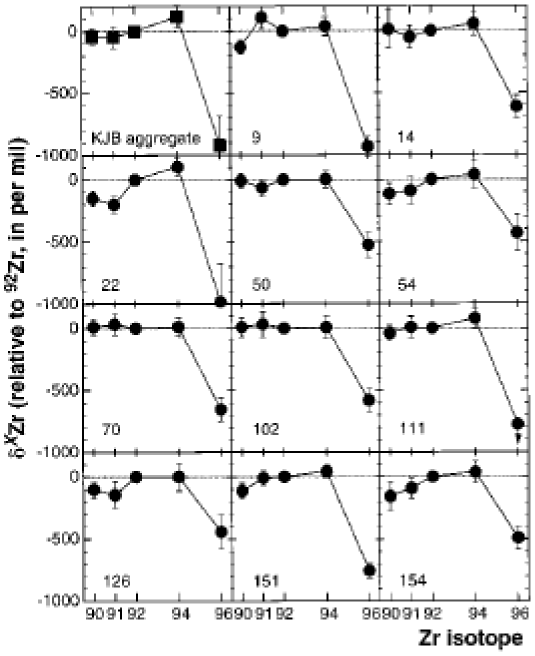

Figure 2.4 Zirconium isotopes patterns as function of mass for single SiC grains (circles) and an aggregate SiC grain (squares) from the Murchison meteorite. The graphs are in the δ notation (see § 6.3.2 for more details). The number in the bottom left of each plot indicate the number of SiC grains (200 single SiC where isolated from the meteorite). For grain 111, a 2σ upper limit for δ^{96}Zr is indicated by an arrow. (Picture from[129])

Chapter III Experimental apparatus

3.1 Introduction

The main nuclear physics input for s-process studies are the (n,γ) cross sections of all nuclei along the reaction path from Fe to Bi as well as the β-decay rates of the branching points.

Laboratory studies of stellar (n,γ) cross sections have to cover the neutron range from 0.1 eV to a few hundred keV. Neutrons in this energy region can be produced in several ways, which are discussed in the following.

Nuclear reactions, such as ^{7}Li(p,n)^{7}Be (Q = -1.644 MeV) at low-energy particle accelerators can be utilized to produce neutrons. From the kinematics of this endothermic reaction follows that near threshold ($E_p^{thresh} \approx -\frac{Q(m_n+m_{^7Be})}{M_{^7Be}} = 1.881\,\mathrm{MeV}$) neutrons are released with an energy of 30 keV and they are emitted in the forward direction. These facilities offer the possibility, with an opportune choice of E_p, of tailoring the neutron spectrum exactly to the energy range of interest; this has the advantage of low backgrounds. Therefore, relatively short neutron flight paths can be used in these cases which compensate to certain extent the limitation in neutron flux. An interesting technique has been applied in a number of neutron-induced reactions by bombarding a $\approx$ 10 μm thick metallic lithium target with protons of energy E_p = 1912 keV, only 31 keV above the reaction threshold. The released neutrons are emitted in the forward direction in a cone with opening angle of 120^{o}. In this case, the angle-integrated energy distribution of emitted neutrons closely resembles a Maxwell-

Boltzmann distribution at kT = 25 keV [32]. If the irradiated sample is mounted very close to the lithium target then the energy distribution of the neutrons incident on the sample is given by the same Maxwell-Boltzmann distribution. The measured average cross section gives then directly the Maxwellian-averaged cross section (see § 4.6).

Much higher intensities can be achieved at linear accelerators via (γ,n) reactions by bombarding heavy metal targets with electron beams of typically 20 - 150 MeV. When the energetic neutrons produced are slown down by a moderator, the resulting spectrum contains all energies from thermal to near the initial electron energy. The measurements need to be carried out at long neutron flight paths, since high resolution is needed in the resonance region. Examples of neutron time-of-flight facilities based on photonuclear reactions are ORELA in Oak Ridge, Tenessee, GELINA in Geel, Belgium, and RPI Rensselaer in Troy, New York.

Spallation reactions induced by energetic particle beams provide the most prolific source of fast neutrons. Also for these facilities the neutron energy range is quite wide and the measurements need to be carried out with the time of flight technique. Facilities of this type are n_TOF at CERN, LANCSE at Los Alamos, and ISIS at Rutherford Appleton Laboratory in Oxfordshire.

Thermal reactors also play a role in this type of measurements. With neutron filters quasi-monoenergetic spectra, suited for cross section measurements, can be produced in the keV range.

The experiments described in this work were carried out at two different neutron facilities, n_TOF located at CERN and GEel LINear Accelerator (GELINA) located in Geel, Belgium. The techniques of these two facilities to produce neutrons are different but both of them are time-of-flight (TOF) facilities. In the following this method will be described in detail and the two facilities and experimental setup will be shown.

3.2 The time-of-flight method

Neutron time-of-flight measurements require a pulsed neutron source. In a relatively short time interval, typically a few nanoseconds, neutrons are generated in a broad energy spectrum; the time at which the neutrons are generated is called t_0. The neutron travels a distance L from the production site to the experimental setup. This distance can vary from a few meters to several hundreds of meters. The reaction products generated in the sample studied are detected and used as stop signals, t_s. The time of flight of the neutron having induced the reaction is given by:

$$t = t_s - t_0 \qquad [3.1]$$

The kinetic energy of the neutron, E_n, is given by:

$$E_n = m_n c^2 \left(\frac{1}{\sqrt{1 - \frac{L^2}{(tc)^2}}} - 1 \right) \qquad [3.2]$$

Where c is the speed of light. In the non relativistic case (E < 100 keV), the well known classical expression of the kinetic energy is applied :

$$E_n = \frac{1}{2} m_n v^2 = \frac{1}{2} m_n \left(\frac{L}{t}\right)^2 \qquad [3.3]$$

The effective flight length L includes not only the geometrical distance between the neutron source and the sample, but also the moderation path followed by the neutron inside the production target and the moderator. Since the moderation process varies with the energy of the neutron, one has to take in account that the effective length depends also on the neutron energy E_n.

For convenience, L can be written as the sum of two terms,

$$L = L(E_n) = L_0 + \Delta L(E_n) \qquad [3.4]$$

Where ΔL includes any dependence of the flight length on the neutron energy E_n due to the moderation process. The constant term L_0 represents the geometrical distance between the outer face of the moderator and the detector in the experimental area.

In the case of the GELINA facility, due to the geometry of the target and moderator this effect is at the first order negligible, while for the n_TOF facility, as will be shown in the following, it cannot be neglected. This difference between the two facilities can be seen from the energy resolution showed in Fig 3.8 and Fig. 3.9. The energy resolution of GELINA facility (lower part of Fig. 3.8) is in first approximation independent on the energy, while n_TOF for neutron energy above 1 keV the energy resolution depends on the neutron energy (Fig. 3.9).

The recursive dependence of the neutron energy E_n on itself is not a very practical situation from the computational point of view.

However, it can be demonstrated [33] that at n_TOF the energy dependent term ΔL can be expressed in terms of a constant time offset, t_{off}, to the measured time of flight t, and Eq. 3.3 can be written as:

$$E_n = \frac{1}{2} m_n v^2 = \left(\frac{72.2977\, L_0}{t + t_{0ff}} \right)^2 \qquad [3.5]$$

this equation is much more practical than equation 3.4, since the recursive dependence on E_n is avoided.

In order to find the values of the calibration parameters L_0 and t_{off}, a set of standard resonances have been measured at n_TOF [33].

In neutron facilities where neutrons are generated by charged particle reaction with electrons or protons, the charged beam impinges on a thick target, for example U, W, Pb. The reaction mechanism yields a large number of high energy γ-rays travelling along the beam pipe, the so called γ-flash. Since the γ-rays travel with the speed of light, they reach the detector before any neutron bunch. The time of detection of the γ-flash can be used to determine the offset of the time scale.

3.2.1 Overlap filters

In a TOF facility particular care has to be paid that fast neutrons of one pulse do not overlap with slow neutrons of the previous pulse. When the repetition rate is not low enough to prevent such eventuality, an overlap filter is needed.

This is done by placing a dedicated filter in the neutron beam; its thickness has to be a compromise between the request to stop all the neutrons with a flight time longer that the cycle period of the accelerator and to let the other neutrons through as much as possible.

Depending on the flight path length and on the beam frequency different solutions may be applied, the most used are Cd and ^{10}B filters. In Figure 3.1 the total neutron induced cross sections are shown. As can be seen the Cd filter of 4 mm is very active for stopping neutrons below 0.167 eV, while the ^{10}B cross section follows a 1/v shape.

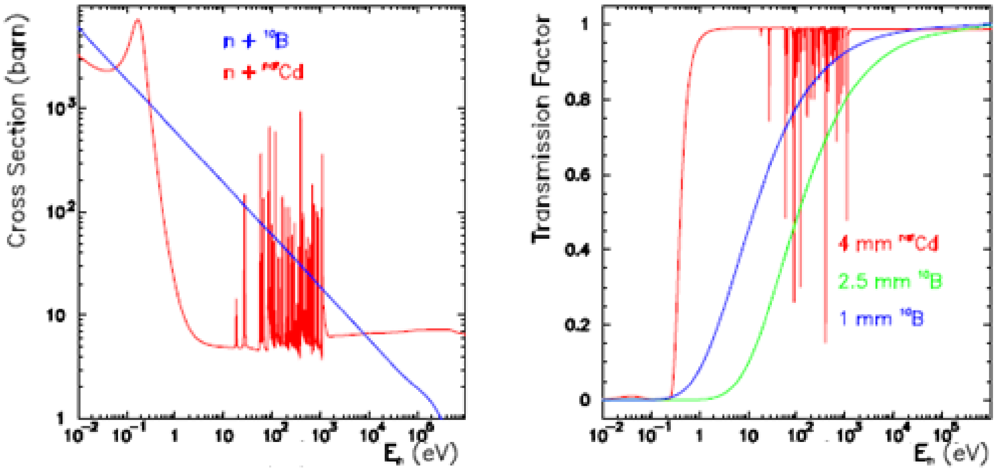

Figure 3.1: The total neutron induced cross section on ^{nat}Cd and on ^{10}B, taken from ENDF/B-VI [105] (left), together with the calculated transmission of the overlap filters [35] (right).

3.2.2 Neutron flux

In order to measure neutron cross sections with the required accuracy of a few percent, it is important to determine the neutron fluence (that is the neutron flux integrated over the time of the measurement) and its dependence on the energy. Typically it is done by means of standard neutron detectors placed in the beam during the measurements. ^{10}B, ^{3}He or ^{6}Li chambers or scintillators and fission chambers are the most common choice. The reaction products resulting from the ^{10}B(n,α)^{7}Li, ^{3}He(n,p)t, ^{6}Li(n,α)t or the ^{235}U(n,f) reactions, are detected by ionization chambers or silicon detectors. The energy range in which the neutron flux has to be measured, determines the reaction to be used. Fig. 3.2 shows the ^{10}B(n,α) and ^{6}Li(n,α) cross sections, these chambers are used from thermal to approximately 0.1 MeV neutron energy. For higher neutron energies fission chambers are used.

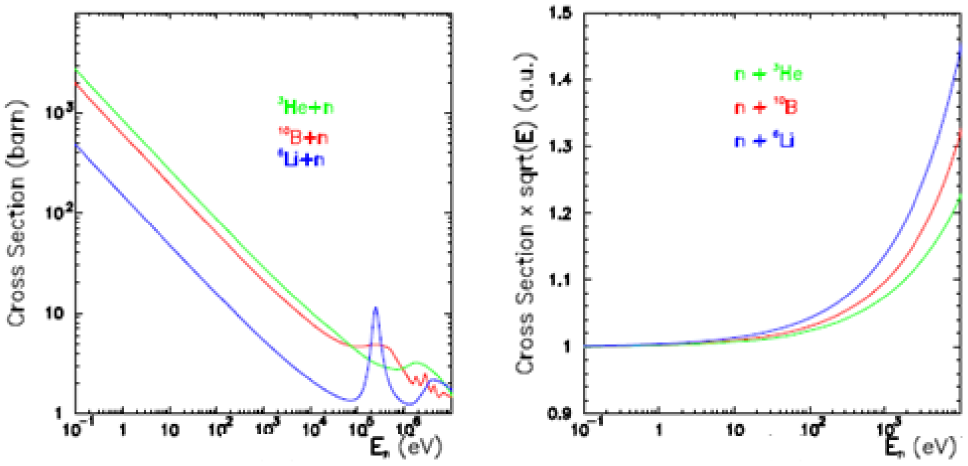

Figure 3.2 The n + ^{10}B, n + ^{6}Li and n + ^{3}He cross sections as a function of the Energy, left panel. On the right panel the deviation from 1/v is more evident, the n + ^{10}B, n + ^{6}Li and n + ^{3}He cross sections are multiplied by v and normalized to 1.

3.2.3 Background filters

To determine the time dependent background the so called black resonance filters are used [36].

Foils of Rh, Ag, W, Mo, Co, Na, S, Bi with adequate thickness are placed in the beam line in order to absorb nearly all the neutrons in a given energy range, the so called black resonance. In such way any count rate observed in the energy region of the black resonance can be attributed to the background.

Contrary to the overlap filters the black filter are not always in the neutron beam, they are used only for the estimation of the background. In some cases, as for the GELINA facility, one black filter is always in the neutron beam, which allows a better normalization of the background measurement.

3.3 The n_TOF facility at CERN

n_TOF [37,38,39] is a time of flight facility based on a spallation source. Neutrons are produced by spallation reactions induced by a sharply pulsed, 6 ns wide (RMS), 20 GeV/c proton beam impinging onto a high purity lead block of 80x80x60 cm^3. This spallation mechanism, generates in average about 300 neutrons per incident proton.

The protons are provided by the CERN Proton Synchrotron (PS)[40], which is able to produce a total of 3×10^{13} protons in a 14.4 s supercycle. The supercycle is divided into sub-intervals, delivering a bunch of protons every 2.4 s (or multiples of this quantity). The PS proton beam can operate in a dedicated mode, delivering 7×10^{12} protons per bunch, or in parasitic mode, delivering 4×10^{12} protons per bunch.

The beam is extracted from the PS and sent onto the spallation target by using a fast extraction system. In terms of peak intensity, the proton beam for n_TOF can be considered as a record for the PS thanks to a special compression procedure, by which the original pulse width of 12 ns is reduced to 6 ns [41].

The neutrons produced by spallation in a lead block surrounded by a water moderator, are canalized through an evacuated flight path to the experimental area at about 185 m downstream from the lead target.

The main characteristics of the proton beam used are:

- a momentum of 20 GeV/c;
- proton bunches of 7×10^{12} particles with a width of 6 ns (RMS);
- up to six bunches per supercycle of typically 14.4 s.

The angle on the horizontal plane between the proton beam axis and the neutron beam is of 10° in order to minimize the number of unwanted secondary particles in the experimental area. At the end of the primary section a sweeping magnet is used to remove the remaining charged particles from the beam line. The diameter of the beam tube is progressively reduced from 800 mm at the target station to 600 mm and eventually to 400 mm before the first collimator, located at 127 m from the target. In the primary section massive concrete and iron shieldings are placed at 72 m and 140 m.

The diameter of the tube is reduced to 200 mm before the second collimator, at 175 m from the target. Before the experimental area the tube crosses a 3.2 m thick concrete shielding wall.

The very high instantaneous intensity is an advantage for measurements of radioactive samples with a greatly improved signal to background ratio covering a unique range in neutron energy from thermal to, potentially, several GeV.

3.3.1. Beam characteristics

In Fig 3.3 the energy distribution of the neutron flux at the sample position at 185 m for a standard time-of-flight bunch of 7×10^{12} protons is shown.

This particular isolethargic shape, i.e. the neutron flux as function of the energy E is ≈ 1/E, is obtained by moderating the fast neutron spectrum with a layer of 5.8 cm of water surrounding the lead target. The data shown in the Fig 3.3 are based on measurements performed with a parallel plate fission ionization chamber loaded with ^{235}U for neutrons with energy > 1 keV, while the flux at lower energy is obtained using the ^{6}Li(n,α) reaction (see next section). In Fig. 3.9 is shown the resolution function at the sample position (185.2 m), given as the distribution of the equivalent distance as a function of the neutron energy, in the range from 1 eV to 1 MeV (the figure is inserted in the end of the chapter to allow a comparison between the n_TOF and GELINA facilities)

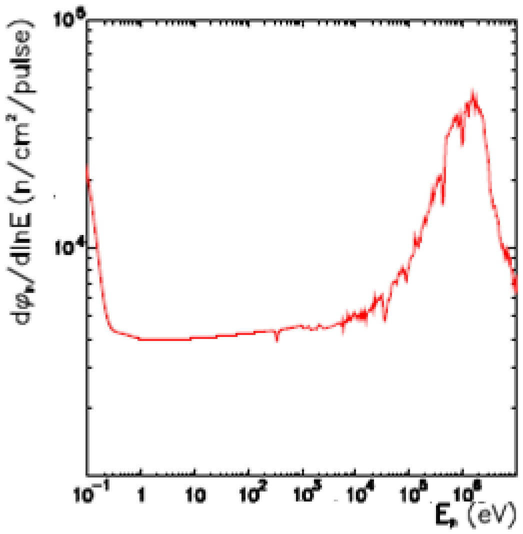

Figure 3.3 The n_TOF neutron flux per bunch at the sample position in the experimental area at 185 m from the spallation target for a standard pulse of 7×10^{12} protons.

In the spallation process by the 20 GeV/c proton beam many charged and neutral particles are produced [42]. While charged particles are strongly suppressed by the sweeping magnet at 145 m from the target, neutral particles and γ-rays can reach the measuring station. The γ-rays are produced in the spallation reaction and in the moderator. These photons can be separated in two groups depending on the way they are generated, a "fast" component resulting from the spallation process itself, they are detected in the measuring station in less than 1 μs, and a "slow" component produced by the thermal neutron capture in the moderator and in the lead target, the latter are detected in a time between 1 μs to a few 100 μs. The fast component, also called γ-flash, is used to determine the offset on t_0 of each pulse.

The γ-flux of the "slow" component arrives at the measuring station in time with neutrons with an energy of a few keV. Since this γ-flux is more than an order of magnitude smaller that the neutron flux [41], it represents a severe source of background in capture cross section measurements. A detailed study of this background shows that 40% of it is due to neutron capture on the hydrogen producing 2.2 MeV γ-rays. Another 5% contribution from photons with energies around 7 MeV results from the capture on lead, on the aluminum alloy sample container and on the iron target support.

3.3.2 Silicon Monitor

For routine neutron beam monitoring a simple system based on silicon detectors has been developed [34]. Four silicon detectors are viewing a foil consisting of a pure ^{6}Li layer 200 μg/cm^{2} in thickness and 6 cm in diameter, which is deposited on a substrate of 3 μm thick Mylar. The geometry is designed such that only the ^{6}Li sample is exposed to the neutron flux, whereas the Si detectors are placed outside of the neutron beam (see Fig. 3.4.a). The ^{6}Li deposit is protected by a 10 μg/cm^{2}layer of evaporated carbon, which allowed maintaining the ^{6}Li deposit in proper state even after four months of operation and several air/vacuum cycles. The energy spectrum deposited in the Si detectors shows a double peak, due to the tritons and alpha particles from the ^{6}Li(n,α)^{3}H reaction, clearly separated, see Fig 3.4.b.

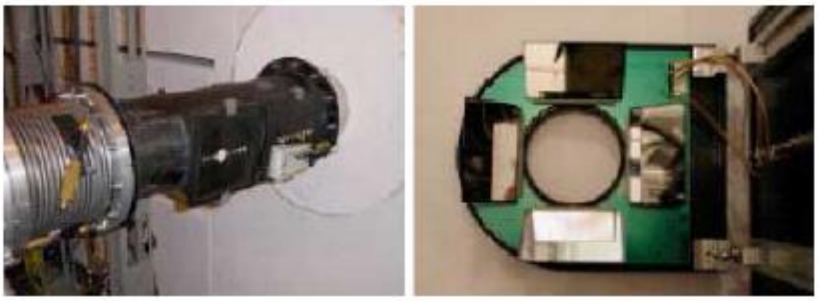

Figure 3.4.a: Carbon-fiber chamber (left) and internal geometry of silicon monitor detectors.

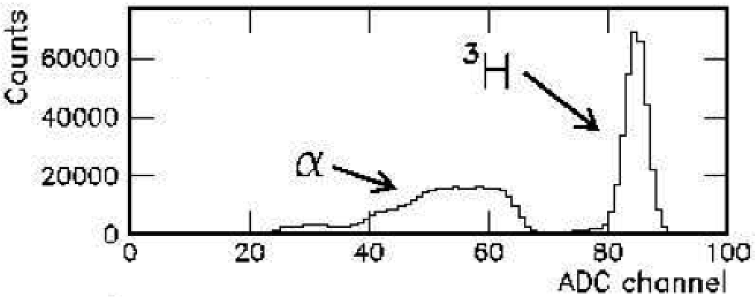

Figure 3.4.b: Particle spectrum from ^{6}Li(n,α)^{3}H reaction taken with the neutron flux monitor

3.3.3 Capture detectors and data acquisition system

In the n_TOF experiments two different detector systems are used for capture measurements: liquid scintillators and a calorimeter of BaF2 crystals.

The liquid scintillators are two in-house developed deuterated benzene C_6D_6 γ-ray detectors [43]. The peculiarity of these detectors is their low neutron sensitivity, which was achieved by substituting or removing all the material that could have a neutron capture. The usual aluminum container of the scintillator cell was replaced by a carbon fiber container and the quartz window for the optical coupling of the scinitillator cell with photomultiplier was removed. As shown in Fig 3.5 the scintillators used at n_TOF have a very low neutron sensitivity compared to the commercial C_6D_6.

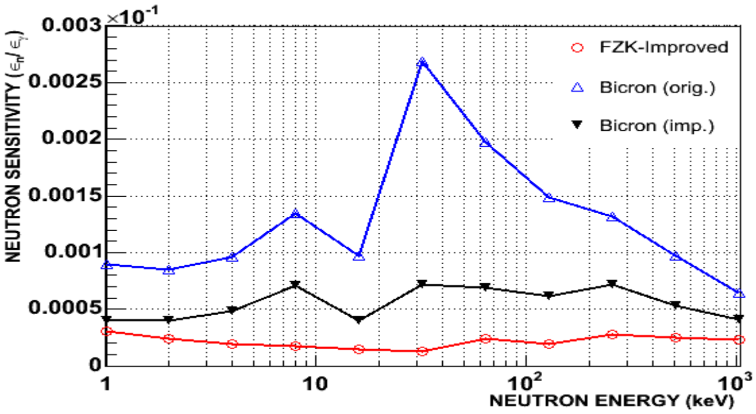

Figura 3.5. Comparison of the neutron sensitivity of three different types of C_6D_6 scintillator neutron detectors. In red the detector used at n_TOF facility. In blue the commercial C_6D_6 from Bicron. In black the modified commercial detector, the photomultiplier tube has been especially built with no borated glass window. (Picture from [43].

The samples to be measured are kept in position by a carbon fiber sample changer, in Fig 3.6 a schematic view of the n_TOF (n,γ)

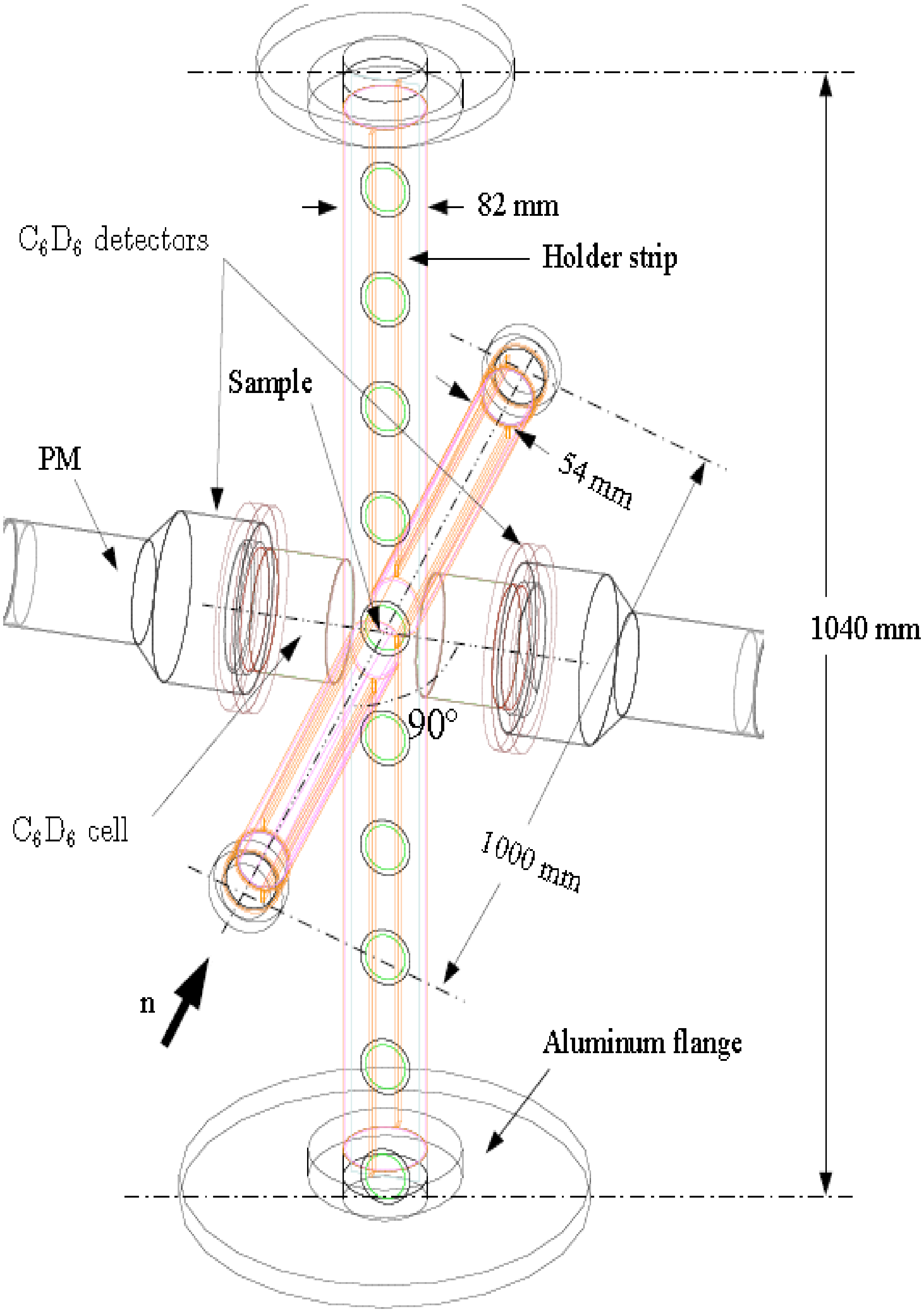

Figura 3.6: Schematic view of the n_TOF (n,γ) experimental setup with the sample changer and two C_6D_6 detectors.

experimental setup with the sample changer and two C_6D_6 detectors is shown.

The second capture detector system has become available in 2004. It is a 4π 100% efficiency total absorption calorimeter (TAC) detector made of 42 BaF_2 crystals in a ^{10}B loaded carbon fiber capsule, coupled to XP4512B photomultipliers. Samples are placed in the center of the calorimeter and are surrounded by a neutron absorber. In Fig 3.7 a schematic view of the TAC is shown.

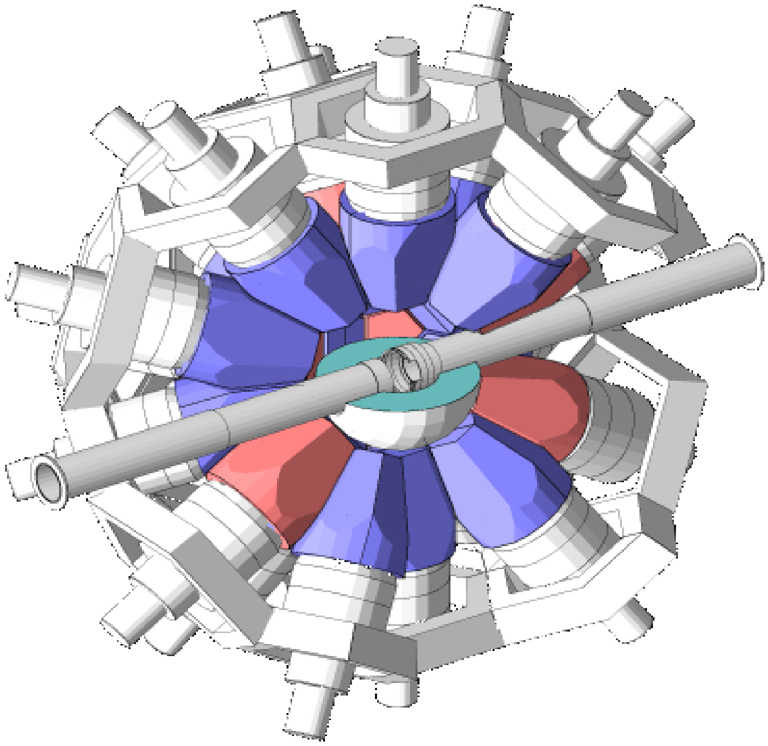

Figure 3.7 Schematic view of the total absorption calorimeter at the n_TOF facility.

The data acquisition system [44] is entirely based on flash ADCs with 8 bit resolution and 1 ns sampling time with 8 Mbytes of memory. It allows recording the full detector signals following the start time given by the incident protons. The digitizers were operated at 500 Msamples/s allowing storing the detector signal for 16 ms, corresponding to a neutron energy of 0.3 eV. After zero suppression, the data are sent to CERN's data storage facility CASTOR for offline analysis.

In 2009 for safety reasons the spallation target was changed, the radioactivity measured in the filters of the cooling system was too high, most probably due to a not well designed target cooling system. The new spallation target has an optimized cooling system which is separated from the moderator, it adds more flexibility in the choice of the moderator. All the n_TOF measurements described in this thesis were performed before 2009.

3.4 The GELINA facility at EU-JRC-IRMM

The Geel Electron Linear Accelerator (GELINA) is a neutron TOF-facility built in 1965 and subsequently upgraded; the last upgrade was done in 2009. The facility has been especially designed and built for high-resolution cross section measurements. It is a multi-user facility, serving up to 10 different experiments simultaneously, providing a pulsed white neutron source, with a neutron energy range between 10 meV and 20 MeV.

The GELINA facility consists of four main parts: a linear electron accelerator, a compression system, a neutron production target with moderator and finally a flight-path area.

Electrons with energy of 100 keV are injected by the triode gun that produces bursts with a pulse length of about 10 ns. These electrons are accelerated in three sections: a 2 m standing wave accelerator section and two 6 m travelling wave sections. In the first section the electrons reach a velocity close to the speed of light and in the following 2 sections they mainly gain energy in the form of mass. This results in a maximum energy of 140 MeV.

The 10 ns time spread of the relativistic electrons leaving the accelerator sections is reduced using a dedicated post-acceleration compression magnet. The pulse width of the electrons is reduced to less than 1 ns (FWHM) with an associated peak intensity of about 100 A [45].

These high energy electrons hit a mercury cooled rotating uranium target, in which they are slowed down, generating Bremsstrahlung. Neutrons are mainly produced via photonuclear reactions (γ,n) and (γ,2n) and via photofission reactions (γ,f) [46]. To increase the number of slow neutrons, two water-filled beryllium moderators are placed above and below the uranium target. Water and beryllium are good neutron moderators because neutrons are slowed down efficiently by collisions with low mass nuclei; moreover hydrogen has a very large neutron scattering cross section. The resulting neutron energy distribution is characterized by a Maxwellian distribution at thermal energy and a high energy tail with approximately a 1/E-shape.

These moderated neutrons are emitted in all directions hence feeding the 10 different flight paths which lead to the measurement station. The flight paths have lengths ranging from 8m to 400 m. Depending on the repetition frequency of the linac (40 Hz to 800 Hz) and the flight path length, the experimentally usable neutrons have an energy range from a few meV up to some MeV. Since the moderated neutrons are emitted isotropically, the neutron flux at a certain distance L from the neutron target is proportional to $1/L^2$.

In Figure 3.8 the flux at the measurement station FP15-30m is shown together with its resolution function. At 800 Hz operating frequency, the target delivers a neutron intensity of about 3.4×10^{13} neutron/s. Using suitable collimators, either the direct neutron spectrum (from 100 keV to 20 MeV) or the moderated spectrum (from 10 meV to 1 MeV) can be viewed. As already pointed out in § 3.2, at 30 m flight path a Cd filter may be utilized only at 50 and 100 Hz repetition rate, since the overlapping energy is below the 0.167 eV Cd resonance. At higher linac frequency a ^{10}B filter with adequate thickness is needed. This introduces a higher limit on the minimum experimentally usable energy (around 100-200 eV) due to the large attenuation of the neutron flux and the consequent small signal/background ratio.

The total neutron output is continuously monitored by several BF_3 proportional counters placed at different positions around the target hall. These monitors measure the energy-integrated neutron flux.

Their output is used to monitor the stability of the accelerator and to normalize spectra to the same total neutron output. These monitors are called central monitor (CM).

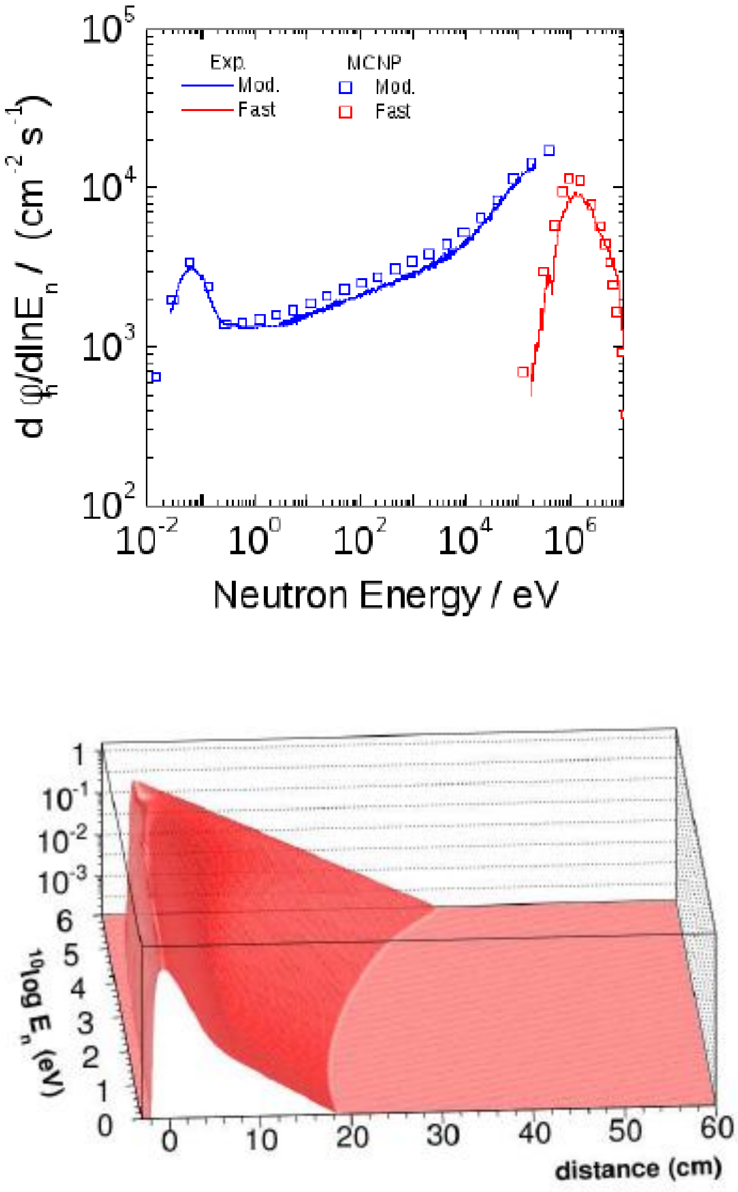

Figura 3.8 The Gelina neutron flux obtained by means of simulations and measurements, top part, and the energy resolution at flight path FP15-30 m, lower part, [47, 48]

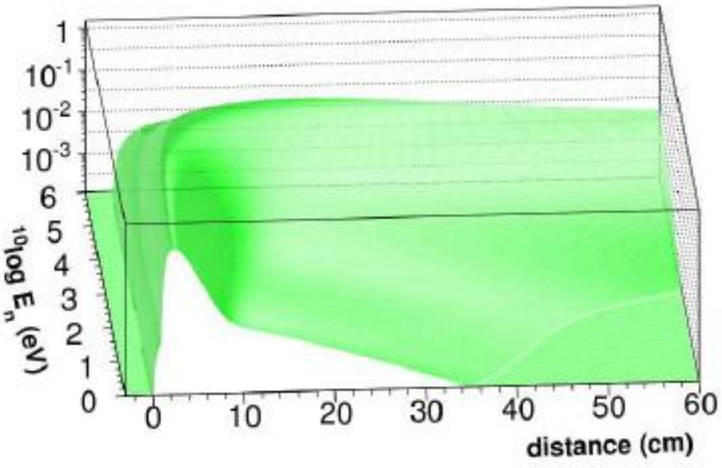

Figure 3.9: The resolution function at the sample position (185.2 m) of the n_TOF facility, given as the distribution of the equivalent distance as a function of the neutron energy, in the range from 1 eV to 1 MeV [49]

3.4.1. Capture and Transmission instrumentation

At the GELINA facility for capture measurements, commercial C_6D_6 scintillators are used. The determination of the neutron flux is performed by an ionization chamber based on the $^{10}B(n,\alpha)$ standard reaction, since it allows to measure the shape of the neutron flux.

Transmission measurements can be performed at 25 m, 50 m, 100 m, 200 m, 400 m flight paths using Li-glass detectors [47,50] or plastic scintillators [51]. To study the Doppler broadening one of the measurement stations is equipped with a cryostat, which is able to cool the sample down to 10 K [52].

Chapter IV Measurement and analysis technique

4.1 Radiative neutron capture

The purpose of this section is to describe briefly the radiative neutron capture process and to define the terms which are going to be used in the following parts. A detailed description of the physics involved can be found in [53, 54].

The radioactive capture reaction proceeds through the formation of an excited compound nucleus and its subsequent decay emitting one or several prompt γ–rays

$$(Z, A) + n \rightarrow (Z, A+1)^{*} \rightarrow (Z, A+1) + \gamma. \qquad [4.1]$$

This neutron reaction is sketched in Fig 4.1. On the right side, the two observables of this reaction are shown. These correspond to the measured time of flight, and therefore the neutron energy, E_n, and to the γ–ray spectrum. The energy of the γ–rays is deposited, E_{dep}, in radiation detectors, which for the present work are C_6D_6 detectors.

The compound nucleus is excited to a level with an energy given by,

$$E^{*} = S_n + \frac{A}{A+1} E_n. \qquad [4.2]$$

Where S_n is the neutron separation energy of the nucleus (Z, A+1) and E_n is the energy of the incident neutron. The compound nucleus decays after a very short time $\tau_\gamma \sim 10^{-14}$ s by emission of one or more γ-rays E_j^{γ} to reach the ground state. Neglecting the recoil energy of the nucleus and the electric conversion, one can write in very good approximation,

$$E^{*} = \sum_j E_j^{\gamma}. \qquad [4.3]$$

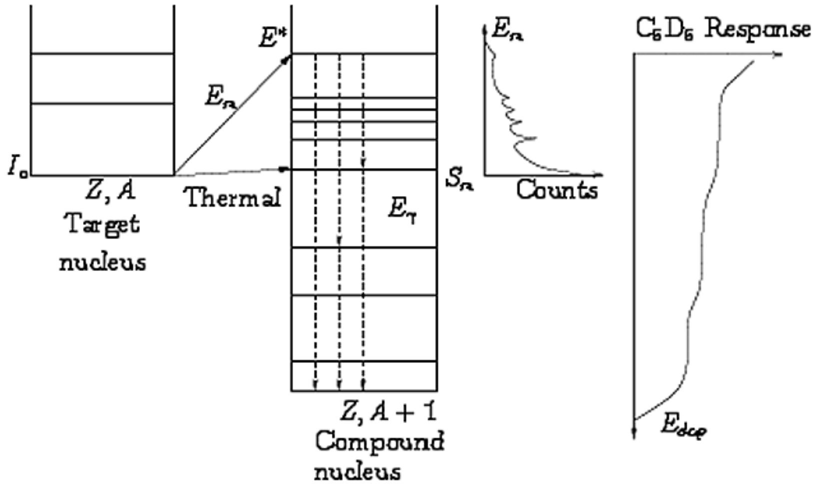

Figure 4.1 Scheme of the radiative capture process and the two observables measured in the experiment, the neutron energy and the response of detector.

The total cross section is related to the formation probability of the compound nucleus. This probability is best described by the R-matrix theory, for more details see [55-60], which for a well isolated resonance simplifies into the Breit-Wigner dispersion formula (neglecting the interference term between potential scattering and resonance part),

$$\sigma_{c^{*}}(E_n) = g\,\frac{\pi}{k_n^2}\frac{\Gamma_n\Gamma}{(E_n-E_0)^2+(\Gamma/2)^2}. \qquad [4.4]$$

where ,

E_o is the energy of the resonance.

g = (2J + 1)/((2s +1)(2I +1)) the spin factor, where:

I is the spin of the target nucleus,

J is the spin of the compound nucleus,

s is the spin of the neutron,

$k_n = 2.196771 \times 10^{-3} \frac{A}{A+1}\sqrt{E_n}$ the neutron wave number,

Γ is the total width,

Γ_n is the neutron scattering width.

The total width Γ is the sum of the individual contributions to the reaction widths,

$$\Gamma = \Gamma_n + \Gamma_\gamma + \Gamma_f + \Gamma_p + \ldots.. \qquad [4.5]$$

The radiative capture width Γ_γ is generally of the order of 0.1 – 1 eV and smaller for heavy nuclei (0.01 – 0.03 eV). These widths imply, through the uncertainty principle $\Gamma_\gamma\, \tau_\gamma \approx \hbar$, that the mean radioactive lifetime is about $\tau_\gamma \sim 10^{-14}$ s. In the energy range and for the nuclei under study in the present work only the neutron scattering channel, Γ_n, shows a similar lifetime, all other channels are excluded by their orders of magnitude larger lifetime. The probability of the compound nucleus to decay by any a channel r is given by,

$$P_r = \frac{\Gamma_r}{\Gamma} \qquad r = n, \gamma, \ldots. \qquad [4.6]$$

And the corresponding cross section,

$$\sigma_r = \sigma_{c^*}(E_n)P_r. \qquad [4.7]$$

In the case of (n,γ) capture the last equation reduces to,

$$\sigma_\gamma(E_n) = g\frac{\pi}{k_n^2}\frac{\Gamma_n\Gamma_\gamma}{(E_n-E_0)^2+(\Gamma/2)^2}, \qquad [4.8]$$

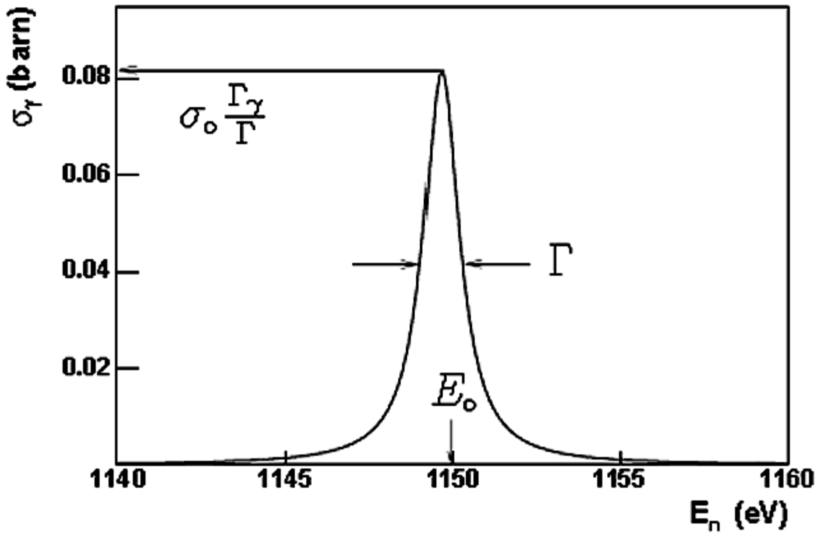

Figure 4.2: Resonance in ^{56}Fe + n, with I = 0, J = ½, orbital angular momentum *l* = 1, E_0 = 1149.7 eV, Γ_γ = 0.574 eV and Γ_n = 0.0617 eV.

The peak cross section, at $E_n = E_0$, is given by,

$$\sigma_\gamma(E_0) = \sigma_0\frac{\Gamma_\gamma}{\Gamma}, \qquad [4.9]$$

σ_0 being the peak value of the total cross section,

$$\sigma_0 = \frac{4\pi}{k_n^2}g\frac{\Gamma_n}{\Gamma}, \qquad [4.10]$$

The total radiative area of a resonance is given by integrating equation 4.8 between $E_0 - \frac{\Gamma}{2}$ and $E_0 + \frac{\Gamma}{2}$,

$$A_r = \frac{2\pi^2}{k_0^2} g \frac{\Gamma_n \Gamma_\gamma}{\Gamma} = \frac{4.09 \times 10^6}{E_0} (\frac{A+1}{A})^2 K, \qquad [4.11]$$

Where K is the radiative kernel,

$$K = g \frac{\Gamma_n \Gamma_\gamma}{\Gamma}, \qquad [4.12]$$

In Fig 4.2 the physical meaning of some parameters described in this section is graphically shown.

4.2 Measurement technique

The goal of this work is the accurate measurement of the capture cross section of the ^{90,91,92,93,94,96}Zr isotopes in the energy range of the resolved resonance region (RRR). From Fig. 4.3, the resonance region is defined when the FWHM, Γ, of the resonance is smaller than the distance D between resonances ($\Gamma < D$), the RRR when the detection resolution, Δ_R, is smaller than D ($\Delta_R < D$) and the unresolved resonance region (URR) when $\Delta_R > D$.

Neutron capture cross sections of these isotopes are very small, thus requiring a measuring technique of high sensitivity or signal to background ratio.

On the other hand, the capture cross section of these isotopes is dominated by resonances, which shows in general a much larger scattering than capture probability. Therefore, for these resonances there are more neutrons being scattered than captured in the sample. These scattered neutrons can be captured in the material of the experimental setup, enhancing the apparent capture yield and contributing as a source of background.

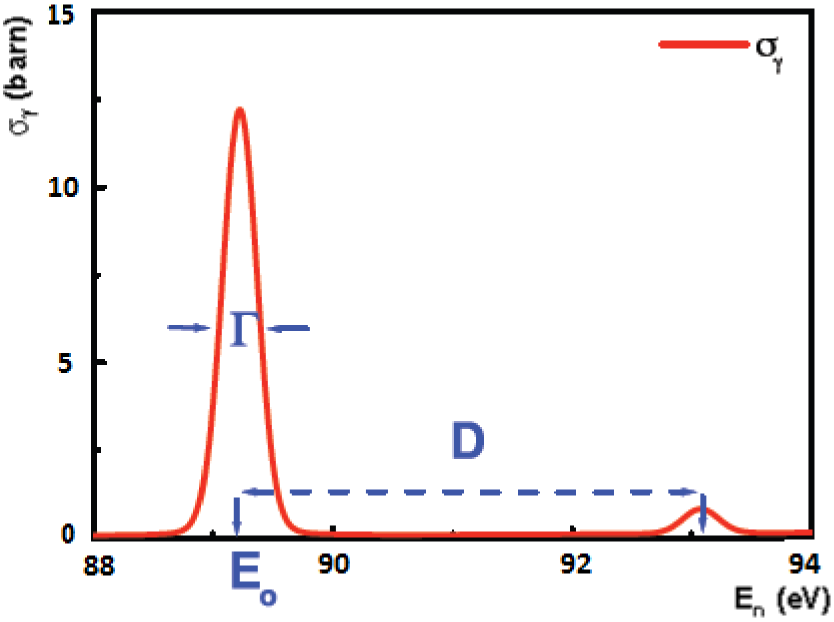

Figure 4.3 Cross section versus neutron energy. E_0 resonance energy, D distance, Γ Full Width Half Maximum (FWHM) of the resonance.

The common technique of measuring the number of cascades by using a 4π detector with high efficiency (calorimetric technique) is not valid for this type of measurements, because of the high level of background due to the neutron sensitivity of this kind of apparatus.

The technique largely used for this type of measurement is the so called total energy detection. There are two ways to apply this technique, the Moxon-Rae detector and the pulse height weighting technique.

The total energy detection principle is based on γ-ray detection system with a very low efficiency, so that at most only one γ-ray of the capture cascade is registered.

$$\varepsilon^{\gamma} \ll 1 \qquad [4.13]$$

But since ε^{γ} varies with the γ-ray energy E^{γ}, such a detection setup would show a detection efficiency for a capture process depending on its particular nuclear deexcitation path. One can avoid this dependence by introducing a proportionality condition into the detection efficiency,

$$\varepsilon^{\gamma} = \alpha E^{\gamma} \qquad [4.14]$$

if the last equation is also fulfilled, then the probability to detect a cascade will be independent of the particular deexcitation path, indeed:

Mathematically, the efficiency of detecting a nuclear cascade composed of j = 1, ….., N γ-rays of energy E_j^{γ}, can be written as

$$\varepsilon^{c} = 1 - \prod_{j=1}^{N}(1 - \varepsilon_j^{\gamma}) \qquad [4.15]$$

where ε_j^{γ} is the efficiency to register a γ-ray of the energy E_j^{γ}. The latter equation describes the probability of detecting at least one of the cascade γ-rays, which has been written as the complementary of not detecting any of those γ-rays.

Given the initial condition (4.13 and 4.14), the previous equation can now be written in good approximation as,

$$\varepsilon^{c} \approx \sum_{j=1}^{N} \varepsilon_j^{\gamma} = \alpha \sum_{j=1}^{N} E_j^{\gamma} = \alpha E_c \qquad [4.16]$$

Hence, as the cascade detection probability ε^c is now proportional to the constant value of the neutron capture energy E_c, it does not depend any more on the particular nuclear deexcitation path or prompt γ-ray registered.

While the first condition (4.13) of having very low γ-ray detection efficiency can be easily achieved by utilizing small volume and low Z detectors, the second condition (4.14) is more complicated to fulfill.

In the early 60's, the Moxon-Rae detector [61] was a first approach to the total energy detection. The idea is that a plastic scintillator with a thick converter wall of a low Z material has a γ-ray detecting efficiency which increases nearly linearly with γ-ray energy. This feature makes the efficiency for the detection of a capture event independent of the particular γ-ray cascade emitted.

Maier-Leibnitz showed [62] that for a wide class of radiation detectors one can generate an average response function proportional to energy by applying to each pulse from the detector a certain weight, which is a function of the pulse size only. This is the basic idea of the so called Pulse Height Weighting Technique (PHWT) and has the big advantage of considerable freedom in optimizing the detection system in terms of insensitivity to scattered neutron backgrounds, shielding, efficiency, time resolution, etc. By calculating an accurate Weight-Function (WF), one can in principle obtain a better proportionality between γ-ray efficiency and energy than with the Moxon-Rae method.

For the measurement of the isotopes object of this work, low neutron sensitivity detectors and PHWT have been used. The neutron sensitivity of the experimental setup used in previous measurements of these isotopes [63], was still a source of high systematic uncertainty and the measured cross sections needed in some case corrections larger than 50%.

4.3 Pulse height weighting technique

In order to calculate the PHWT one need to know the response function of the detection system. If we assume R_i^γ, with i = 1,…..,n, to be the response function of the detection system for a capture γ-ray of energy E^γ, normalized to the efficiency for detecting that γ-ray, i.e., $\sum_{i=1}^{n} R_i^\gamma = \varepsilon^\gamma$. The proportionality condition (4.14) between detection probability and γ-ray energy can be achieved by appropriately weighting the response function R_i^γ for the registered γ-ray,

$$\sum_{i=1}^{n} W_i R_i^\gamma = E^\gamma. \qquad [4.17]$$

In the last equation, the proportionality constant α has been chosen equal to one in inverse energy units. The weighted response function, $R_i'^\gamma = W_i R_i^\gamma$, fulfills now the proportionality condition 4.14 between efficiency and γ-ray energy,

$$\varepsilon'^\gamma = \sum_{i=1}^{n} R_i'^\gamma = \sum_{i=1}^{n} W_i R_i^\gamma = E^\gamma \qquad [4.18]$$

It is important to note here, that the accuracy of this technique depends directly on two assumed conditions of low efficiency 4.13 and proportionality 4.14.

The detection of at most one γ-ray of the nuclear cascade, condition 4.13, is sufficiently well fulfilled with the low efficiency experimental setup used for the measurements presented in this work.

In the past the weighting functions were derived using experimental response functions R_i^{γ} for a number of E^{γ} values covering the whole energy range of interest in neutron capture. The WF was one for each capture set-up (and not depending on the sample to be measured) [64].

To obtain reliable WFs, an accurate response of the detection system is required for a set of γ-ray energies. Since the early '90 the R_i^{γ} are calculated using Monte Carlo simulation. The response function depends on the γ-ray transport in the sample and the detector assembly. At n_TOF and GELINA, GEANT [65] and MCNP [66] codes are used with accurate geometry descriptions of the experimental conditions [67,68]. The response is obtained by the convolution of the simulated $R_i^{\gamma}$with a Gaussian function, which represents the amplitude resolution of the detector. Validation of the Monte Carlo calculation is obtained by means of γ-ray sources, comparing experimental and simulated responses.

The WF is obtained by expressing W_i as a smooth function of the observed deposited energy E_i and a set of free parameters. These parameters are obtained by a least square fit to a number of γ-ray responses minimizing the χ^2 defined as,

$$\chi^2 = \sum_j (E^{\gamma j} - \sum_{i=1}^{n} W_i R_i^{\gamma j})^2 \qquad [4.19]$$

Once the WF has been determined, one should check how well the proportionality condition 4.14 is achieved, by substitution of the WF back into the equation 4.17 for a set of γ-ray energies, but they do not give any information about the uncertainty introduced in the capture experiment by the WF itself. In order to determine the WF uncertainty a method based on a Monte Carlo simulation of a realistic nuclear cascade with fixed total energy E_c, where at most one of the prompt γ-rays is registered, was used. Let W_i be the calculated WF and $R_{i,c}$ the response distribution of each simulated cascade c. Then, for a large number of cascades N and an exact WF it should be fulfilled that the weighted sum is equal to the number of cascades times the capture energy.

$$\sum_{c=1}^{N} \sum_{i=1}^{n} W_i R_{i,c} = NE_c. \qquad [4.20]$$

Deviations of the weighted sum (left term in Eq. 4.20) from NE_c indicate the uncertainty due to the calculated W_i.

4.4 Capture reaction yield

The main experimental quantity determined in capture cross section measurements is the reaction yield, i.e. the fraction of incident neutrons undergoing a (n,γ) reaction in the sample. For non fissionable samples and for energies below the first inelastic scattering level, the theoretical expectation value for the capture yield can be expressed as a sum of contributions from multiple scattering events, in which a neutron undergoes a number of elastic collisions before inducing the (n,γ) reaction. In the top part of Fig 4.4 the contribution from multiple scattering events to capture yield is shown.

$$Y_\gamma = Y_{\gamma 0} + Y_{\gamma 1} + Y_{\gamma 2} + \ \ldots.. \qquad [4.21]$$

The first term, $Y_{\gamma 0}$, is the product of the interaction probability of an incident neutron times the ratio $\sigma_\gamma / \sigma_{tot}$:

$$Y_{\gamma 0} = (1 - e^{-n\sigma_{tot}}) \frac{\sigma_\gamma}{\sigma_{tot}} \qquad [4.22]$$

where n is the areal density of the sample. For very thin samples, $n\sigma_{tot} \ll 1$, second order collisions can be neglected, so that $Y_{\gamma^0} \simeq n\sigma_\gamma$.

In general thick samples are used for capture reactions, therefore also the effect of multiple scattering has to be taken in account and Eq. 4.21 must be used. This concerns the fact that there is a non negligible probability that the incident particle scatters from a nucleus in the sample and reacts afterwards with another nucleus in the sample. This effect depends not only on the cross section but also on the sample geometry.

The capture reaction yield is defined as the fraction of the neutron beam particles which undergoes a capture reaction in the sample. The transformation of the registered number of counts into the experimental yield is called data reduction.

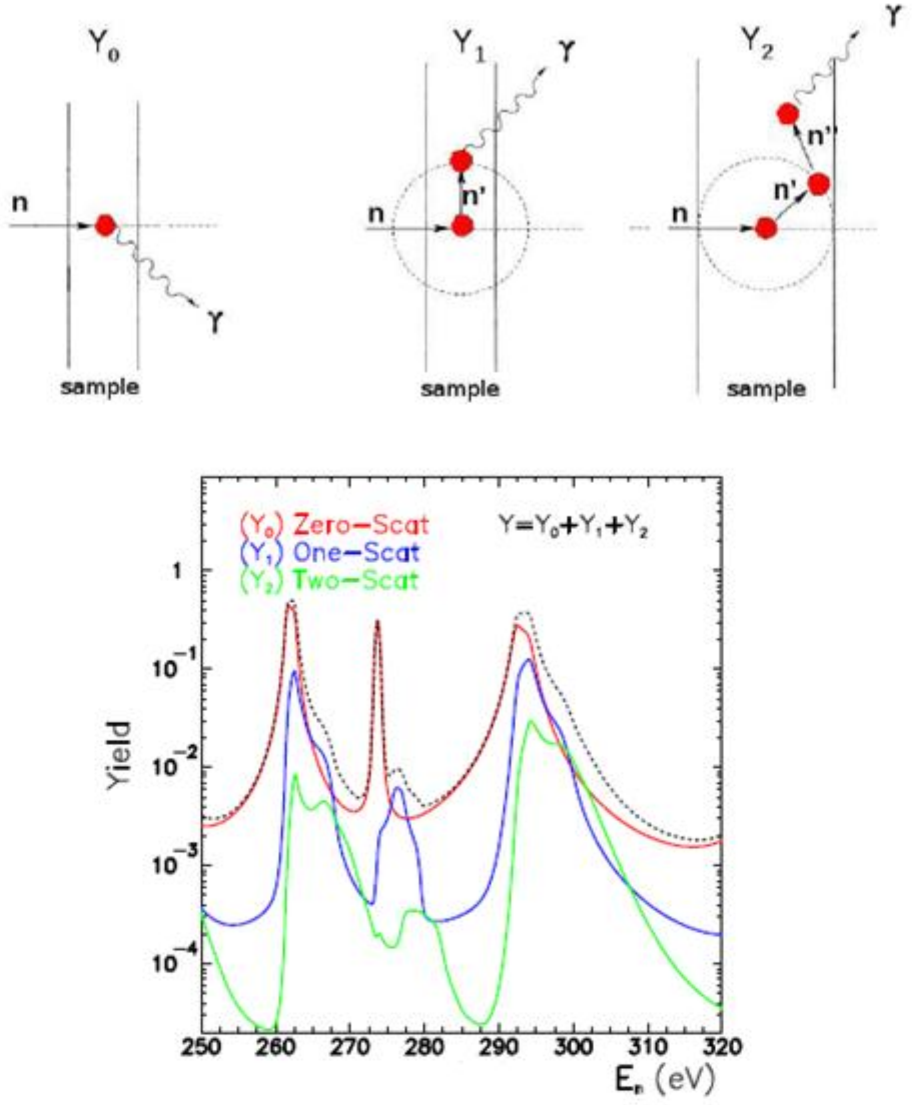

Figure 4.4: Top: Schematic view of the contributions from multiple-scattering events to the capture yield. Bottom: capture yield calculation of Y, Y_0, Y_1, Y_2 for a 1 mm thick Au sample

The raw number of counts registered in one measurement, N, can be written as in the simplest form as depending on the time of flight (t_{TOF}) and the pulse height (A) of each measured signal

$$N = N(t_{TOF}, A) \qquad (4.23)$$

Since we are interested in the yield as a function of the neutron energy E_n, an accurate time of flight calibration is needed. Indeed, as seen in § 3.2 in any time of flight experiment, one of the observables measured during the experiment is the time at which one event (neutron capture) occurs. This time is related with the energy of the neutron by means of equation 3.2.

After this time of flight calibration the experimental capture yield Y can be expressed as the ratio between the number of counts registered in one measurement and the product of the incoming number of neutrons N_n and the efficiency ε,

$$Y_{exp} = \frac{N(E_n, E_{dep})}{N_n(E_n) \times \varepsilon(E_n, E_{dep})} \qquad [4.24]$$

Here E_n is the neutron energy and E_{dep} is the energy deposited in the γ-detectors. The dependence of neutron intensity on energy has been determined from independent measurements, as explained in § 3.3 and 3.4. In general, N_n designates the time integrated neutron flux ϕ_n crossing a sample of a certain surface S,

$$N_n = \iint_S \phi_n dSdt. \qquad [4.25]$$

In the equation 4.24, the dependency on the efficiency must be avoided, since it means a cascade detection probability dependent on the actual deexcitation path. As was described in § 4.2, applying the PHWT we have,

$$N^{w}(E_n) = \sum_{E_{dep}} W(E_{dep}) \times N(E_n, E_{dep}). \qquad [4.26]$$

The weighting function, W(E_{dep}), is in general different for each particular capture sample. As discussed in § 4.2, after the weighting function process, the efficiency to detect a capture event becomes now equal to the energy of the cascade, $E_c = S_n + E_n$,

$$N^{w}(E_n) = Y_{exp} \times N_n(E_n) \times E_C(E_n). \qquad [4.27]$$

From the last equation, the experimental yield can finally be expressed as,

$$Y_{exp}(E_n) = \frac{N^{w}(E_n)}{N_n(E_n) \times (S_n + E_n)}. \qquad [4.28]$$

The absolute value of the efficiency ε required for the calculation of W(E_{dep}) is not trivial to obtain since it depends on the exact positioning of the detectors with respect to the samples and on the exact volume of the scintillation liquid in each detector. Variations in these two quantities with respect to the simulation values would introduce only a proportionality constant in the simulation efficiency ($\alpha \neq 1$ in Eq. 4.16). Furthermore, the absolute value of the neutron flux is more difficult to obtain than just its relative dependence with energy.

For the two reasons mentioned just above, the capture yield is always measured relative to a reference sample. This is the usual procedure to determine a cross section using PHWT and it is usually based on the saturated resonance method, see § 4.4.1. The corresponding correction factor will be denoted as f^{sat}.

There are two other additional sources of systematic effect which must be considered in the previous formula in order to determine the experimental yield reliably.

On one side, capture measurements are sometimes affected by a time of flight dependent background, due to the neutron sensitivity of the detection system. The corresponding correction, f^{ns}, for the detection system used for this work (R. Plag et al. [43]) its value, 2.6 x 10^{-5}, is constant in the neutron energy range 0.1 - 1000 keV. The correction due to the neutron sensitivity f^{ns} has been omitted in this work because it was found to be negligible for all the resonances of the Zr's measured, a full description on the neutron sensitivity and how the data should be corrected for it can be found in Borella et al. [68].

The second correction, $f^{t,s,ce}$, is mainly due to the loss of low energy counts below the threshold of the detectors, the summing of the prompt γ-rays and the internal electron conversion process.

The correct capture yield, $Y'(E_n)$, can be finally calculated as,

$$Y'(E_n) = f^{sat} \times f^{t,s,ce} \times Y_{exp}(E_n) \qquad [4.29]$$

other experimental effects like self shielding and multiple neutron scattering in the sample, as well as the Doppler broadening, due to the thermal motion of the atoms in the target, and the yield broadening due to the resolution function of the neutron beam have been included in the resonance analysis, § 4.5.3.

4.4.1 Saturated resonance method

The determination of the capture yield (equation 4.28, § 4.4) depends on the detection efficiency ε and the neutron intensity N_n. But the absolute value of the simulated detection efficiency ε, unlike its relative dependence on the γ-ray energy, depends on several parameters whose exact values are difficult to keep under control such as, e.g., the volume of C_6D_6 liquid in the cells (which may vary with the temperature) and the relative distance between sample and detector. Furthermore, in the determination of the absolute neutron intensity, the analysis of the fission yield in the case of the PTB chamber or the ^{3}H products of the ^{6}Li(n,α) reaction for the silicon monitor, depends on the precise knowledge of cross sections, angular distributions and monitor efficiency.

Performing an inter-calibration measurement with respect to a well known resonance at a given energy E_o, one can avoid these uncertainties related to absolute intensity and efficiency values [128]. One usually chooses a reference sample of small thickness n (at/barn) with a resonance such that $\sigma \approx \sigma_\gamma$ and large $n\sigma$. Then, the yield at the resonance is saturated and it can be determined very accurately in the plateau region.

From equation 4.26, the experimentally determined yield for the reference resonance Y_{ref}^{exp} can be obtained as,

$$Y_{ref}^{exp}(E_n) = \frac{N_{ref}^{w}(E_n)}{N_n(E_n) \times (S_n^{ref} + E_n)} \qquad (4.30)$$

On the other side, the yield at this resonance can be precisely calculated Y_{ref}^{th} if its cross section is very well known and the sample is indeed thin (to avoid large thickness effects corrections). As the transmission is very small, multiple scattering becomes the main source of neutrons loss. $Y_{ref}^{th}(E_n)$ must therefore be calculated with an appropriate code which accounts for those effects. An example of the reference resonance at 4.9 eV in ^{197}Au+n is shown in Fig 4.5. The data points correspond to the experimental yield $Y_{ref}^{exp}(E_n)$. The solid line corresponds to a function with the form, $AY_{ref}^{th} + B$. The parameters A and B were fitted to have,

$$Y_{ref}^{exp}(E_n) = AY_{ref}^{th}(E_n) + B \rightarrow f^{Sat} = \frac{1}{A} \qquad (4.31)$$

the calculated yield Y_{ref}^{th}, as well as the fit, were obtained with the SAMMY code [75], § 4.5.3. B is a constant term which accounts for the background. The value of the yield normalization constant, f^{Sat}, see § 4.4, is given by the inverse of the fitted parameter A.

At n_TOF different reference samples of ^{197}Au and ^{109}Ag have been used, which fulfill the requirements of high and well known peak cross section and small thickness. Since gold is monoisotopic, the pure Au sample was preferred for the yield calibration in the measurement of the Zr isotopes cross sections.

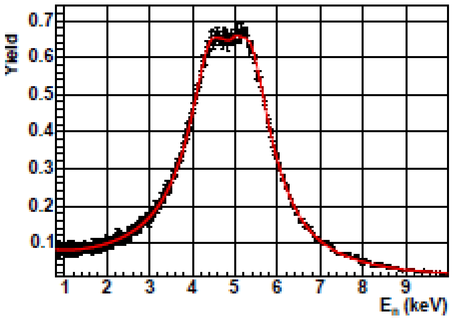

Figure 4.5: 4.9 eV ^{197}Au+n resonance used for normalization

4.5 Resonance analysis of the experimental data

For a non fissile nucleus the total, capture and elastic scattering cross sections can be parameterized with the following resonance parameters: the potential scattering radius, the resonance energy, the neutron and radiation width, the spin and the parity of the resonance. A full set of resonance parameters can be determined by a combination of different types of measurements such as transmission and capture. Furthermore different thicknesses of the same sample can be used in order to obtain a good accuracy of the extracted cross section and in the case of transmission measurements spin information when they are combined. All the data presented in this work are only from capture measurements.

In the analysis of the resonance cross section data the yield is parameterized by means of nuclear reaction theory. In the thermal and resolved region, the R-matrix theory is most conveniently employed. The parameters of this model are level energy, level spin and partial widths.

The advantage of using the R-matrix formalism to describe cross section data, which uses only the properties of the nuclear excitation levels instead of a full description of the forces inside the nucleus, resides on the reduced number of parameters needed to describe the cross section over a wide energy range as well as to ensure consistency with physical constraints [69].

There are several approximations of the R-matrix formalism to describe the cross sections; the most important are the Blatt-Biedenharn, single-level (multi-level) Breit-Wigner, multi-level Adler-Adler and multi-level Reich-Moore. The last one is considered to be the better approximation than the other variants [69].

In the following sections the relation between observables and the resonance parameters will be illustrated.

4.5.1 Area analysis

The area method is based on the fact that the area below a resonance is independent of the experimental resolution and doppler effect (provided that the energy limits enclosing the area are sufficiently far from the resonance energy). Therefore in the case of isolated resonances, the simplest method to extract resonance parameters from measured data is the area analysis [70,71]. The area can be expressed in the following ways depending on the experimental data [72]:

$$A_{tot} = \int (1 - e^{-n\sigma_{tot}})dE \qquad [4.32]$$

$$A_{\gamma} = \int (1 - e^{-n\sigma_{tot}})\frac{\sigma_{\gamma}}{\sigma_{tot}}dE \qquad [4.33]$$

where A_{tot} and A_γ, are the transmission, and the capture area respectively, σ_{tot} and σ_γ are the total and the capture cross section respectively. The sample thickness in atoms per unit area for the transmission and capture is denoted by n. The integrations are performed over the energy range of the resonance.

To calculate the integrals the Doppler broadening effect is neglected and only the resonant part of the Single Level Breit-Wigner (SLBW) formalism is considered for the parameterization of the total and capture cross section. Generally a measurement of two of the areas, observables, should be sufficient to determine Γ_γ and Γ_n. However one has to find the combination that yields the highest accuracy.

In case of a very thin ($n\sigma_{tot} \ll 1$) or very thick ($n\sigma_{tot} \gg 1$) sample the following asymptotic approximation can be applied to the previous equations [72]:

$$A_{tot}(thin) = \frac{1}{2}\pi n\sigma_0\Gamma = 2n\pi^2ƛ^2g\Gamma_n \qquad [4.34]$$

$$A_{tot}(thick) = \sqrt{\pi n\sigma_0\Gamma} = 2\piƛ\sqrt{ng\Gamma_n\Gamma} \qquad [4.35]$$

$$A_\gamma(thin) = \frac{1}{2}\pi n\sigma_0\Gamma_n = 2n\pi^2ƛ^2g\frac{\Gamma_n\Gamma_\gamma}{\Gamma} \qquad [4.36]$$

where $\sigma_0 = 4\piƛ^2g\,\Gamma_n/\Gamma$, ƛ is the reduced neutron wavelength at the resonance energy and σ_0 is the peak total cross section of the resonance. The quantity A_γ is related to the capture kernel, K, defined in equation 4.12, by the following relation :

$$A_\gamma = 2n\pi^2Kƛ \qquad [4.37]$$

The transmission measurements of a thin and thick sample yield the values of Γ and $g\Gamma_n$. When $\Gamma_n \gg \Gamma_\gamma$ the neutron width will dominate the total width, such that $\Gamma_n \approx \Gamma$, g and Γ_n can be obtained; no information about Γ_γ can be obtained by transmission measurements. On the contrary, in the limit of $\Gamma_\gamma \gg \Gamma_n$ the radiation width will dominate the total width, such that $\Gamma_\gamma \approx \Gamma$, and the radiation width and $g\Gamma_n$ can be calculated.

The combination of Eqs. 4.34, 4.35, and 4.36 would yield g, Γ_n, Γ_γ, and Γ, but in the case of $\Gamma_\gamma \gg \Gamma_n$ Eq. 4.36 reduces to Eq. 4.34 and an elastic scattering measurement is necessary to achieve a solution. On the other hand if $\Gamma_n \gg \Gamma_\gamma$, A_γ is proportional to Γ_γ, making the capture measurement necessary. In conclusion the reaction cross section data from elastic scattering, capture and transmission measurements are complementary and at least two of these sets of measurement are needed to determine the partial widths. The results are summarized in Table 4.1

Table 4.1: The resonance area as a function of the resonance parameters for different neutron cross section measurement.

	Area	Resonant Part	
	$E_0, \Gamma_n, \Gamma_\gamma, g$	$\Gamma_n \gg \Gamma_\gamma$	$\Gamma_\gamma \gg \Gamma_n$
A_{tot}(thin)	$2\pi^2 ƛ^2 n g \Gamma_n$	$\approx n g \Gamma_n$	$\approx n g \Gamma_n$
A_{tot}(thick)	$2\pi^2 ƛ \sqrt{n g \Gamma_n \Gamma}$	$\approx \sqrt{n g}\Gamma_n$	$\approx \sqrt{n g \Gamma_n \Gamma}$
A_γ(thin)	$2\pi^2 ƛ^2 n g \frac{\Gamma_n \Gamma_\gamma}{\Gamma}$	$\approx n g \Gamma_\gamma$	$\approx n g \Gamma_n$

Furthermore to obtain the experimental observables related to the areas defined in Eq. 4.34, 4.35 and 4.36 the data must be corrected for the Doppler broadening (which affects the self shielding term), for the energy resolution of the spectrometer, and for the multiple scattering. Procedures to correct the data for these effects are reported in [70,71,73,74].

4.5.2 Resonance shape analysis

Another way to obtain the experimental observables related to the areas defined in the Eq. 4.34 to Eq. 4.36 is performing a full Resonance Shape Analysis (RSA) of the data.

An interactive fitting procedure can be used in the analysis, varying one or more of the parameters describing the “theoretical” yield until the best parameterization has been found for the measured yield.

In this analysis method the experimental data are not corrected for experimental effects, such as Doppler and resolution broadening, but are included in the calculation of the theoretical estimate of the observed yield. In general for a detailed analyses RSA is more convenient, utilizes all the information contained in the data and is more accurate from the analysis viewpoint.

4.5.3 RSA codes SAMMY

The resonance shape analysis code SAMMY [75] has been used to deduce resonance parameters from experimental data. The code can work in the Reich-Moore approximation of the multi-level R-matrix formalism; but also other approximations are also included in the code. This code accounts for the experimental effects in partial cross section measurements, as Doppler broadening, self-shielding and multiple scattering. The theoretical reaction yield and transmission factors are folded with experimental resolution. The resonance parameters together with some other parameters linked to the experimental set up (e.g. normalization, background level, effective temperature, target thickness and homogeneity) can be determined by least-square fits to the experimental data.

In the SAMMY code the experimental data have to be expressed as a function of the energy, therefore the SAMMY code requires the conversion of time-of-flight, being the observable measured, into energy prior to the resonance shape analysis, where the resolution function is applied.

The background of the measurement can be fitted although better results are obtained if the data are background free. SAMMY code provides another possibility, the pointwise background can be given as input, the code will provide to subtract it from the data, in principle there is no difference between to input background free data or make the code do the subtraction of the background from the data.

The fitting procedure consists in the minimization of the χ^2 defined as:

$$\chi^2(\vec{a},\vec{b}) = \left(\vec{Z}_{exp} - \vec{Z}_{calc}(\vec{a},\vec{b})\right)^T V_{Z_{exp}}^{-1} (\vec{Z}_{exp} - \vec{Z}_{calc}(\vec{a},\vec{b})) \quad [4.38]$$

where Z_{exp} is the experimental observable. The corresponding quantity, Z_{calc} as a function of the time-of-flight t is calculated starting from the theoretical quantity Z(E_n) broadened for the experimental effects:

$$Z_{calc}(E_n) = N(\int R_E(E'_n)\varepsilon_c(E'_n)Z(E'_n)d\,E'_n) + B \qquad [4.39]$$

in particular for the transmission factor:

$$T_{calc}(E_n) = N(\int R_E(E'_n)e^{-n\sigma_{tot}(E'_n)}dE'_n) + B \qquad [4.40]$$

for the capture yield:

$$Y_{calc}(E_n) = N(\int R_E(E'_n)\varepsilon_c(E'_n)Y_c(E'_n)dE'_n) + B \qquad [4.41]$$

where $R_E(E_n)$ is the neutron time-of-flight resolution function, $\varepsilon_c(E_n)$ is the detector efficiency for capture events, N is the normalization and B is the background. The matrix $V_{Z_{exp}}$ is the covariance matrix and $\vec{a}$ is the vector of resonance parameters, while $\vec{b}$ is the vector of experimental parameters. This vector takes in account the experimental factors as sample characteristics, flight path length, sample temperature (Doppler), resolution and so on.

4.6 Calculation of the Maxwellian averaged cross section

The quality of s-process calculation depends strongly on the reliability of the input data. As seen in §1.4.1 three sets of data are needed: (1) stellar reaction rates of the nuclei on the synthesis path; (2) β half-lives of the branching points, (3) s-process abundances.

Among these three the set of stellar reaction rates has a particular importance. In the past it was considered sufficient to calculate this set of data only at kT = 30 keV, which was considered the AGB temperature where the s-processes could occur (standard model). In the current models the s-process is expected to be activated at lower temperature in the low mass AGB stars and at higher temperature for massive AGB stars, therefore the relevant temperatures for these models range from kT = 5 keV to 100 keV.

A method of converting the experimental cross section data into proper stellar values has been developed in the past [76], in this thesis a brief summary of the main features of this method are given.

As described in § 1.4.1 the stellar neutron capture rate

$$\langle \sigma v \rangle_A = \int_0^\infty v\sigma_A(v)\Phi(v)dv \qquad [4.42]$$

is determined by the integration of $v\sigma_A(v)$ over the velocity distribution $\Phi(v)dv$. In stellar environments, the relative velocities *v* between the neutrons and the target isotopes follow a Maxwell-Boltzmann distribution at a temperature T

$$\Phi(v)dv = \frac{4}{\sqrt{\pi}}\left(\frac{v}{v_{th}}\right)^2 exp\left(-\frac{v}{v_{th}}\right)^2 d\left(\frac{v}{v_{th}}\right) \qquad [4.43]$$

where $v_{th} = \sqrt{2kT/\mu}$ is the thermal velocity, with μ the reduced mass of the system.

Maxwellian average stellar (n,γ) cross sections $\langle\sigma\rangle$ are defined as

$$\langle\sigma\rangle_{kT} = \frac{\langle\sigma v\rangle}{v_{th}} = \frac{2}{\sqrt{\pi}} \frac{\int_0^\infty \sigma(E_n) E_n \exp\left(-\frac{E_n}{kT}\right) dE_n}{\int_0^\infty E_n \exp\left(-\frac{E_n}{kT}\right) dE_n} \quad [4.44]$$

where $E_n = E_{n,lab}(A/(A+1))$ is the total kinetic energy in the center of mass system, $E_{n,lab}$ is the laboratory energy.

The most common form of Eq. (4.44)

$$\langle\sigma\rangle_{kT} = \frac{\langle\sigma v\rangle}{v_{th}} = \frac{2}{\sqrt{\pi}} \frac{1}{(kT)^2} \int_0^\infty \sigma(E_n) E_n \exp\left(-\frac{E_n}{kT}\right) dE_n \quad [4.45]$$

shows that the (n,γ) cross section as a function of energy, $\sigma(E_n)$, has to be determined over a sufficiently wide energy interval. In order to avoid bias effects due to truncated cross section measurements, data between $E_n \approx 0.1$ and 500 keV have to be considered in the integral to cover the full range of thermal energies from kT = 5 to 100 keV.

In this work the MACSs were calculated using the code SAMMY [75], which calculates the MACS in two different ways, analytical approximation and a numerical calculation technique.

The assumptions under which the analytical approximation is derived are the following:

(1) The function $\exp\left(-\frac{E_n}{kT}\right)$ is constant across the width of a resonance.

(2) The neutron width Γ_n is constant across the width of a resonance.

(3) The multilevel Breit-Wigner approximation provides an adequate description for the cross section.

(4) The lower-energy limit may be extended from 0 to negative infinity. Under these assumptions, the Maxwellian average has the approximate value

$$\langle\sigma\rangle_{kT} = \frac{\pi^{\frac{3}{2}}}{m_n}\frac{1}{(kT)^2}\sum_i \exp\left(-\mu\frac{E_i}{kT}\right)\frac{2g_i\Gamma_{in}\Gamma_{i\gamma}}{\Gamma_i} + \sqrt{\frac{E_{th}}{kT}}\,\sigma_{capture}(E_{th}) \qquad [4.46]$$

where E_{th} = 0.0253 eV is the energy of the thermal neutrons. The summation includes only those resonances that have positive energies, and the “thermal” energy, E_{th}, is somewhat arbitrarily taken to be the lowest energy for which the differential cross sections are calculated. This is sufficient, since results are the same as long as the energy is low enough that the energy-dependence of $\langle\sigma v\rangle$ is $1/v$ (i.e., $1/\sqrt{E}$). An important parameter to indicate the energy-dependence of the reaction cross section σ is the Westcott-g factor [77] which indicates the deviation of the energy-dependence from $1/v$. This factor is equal 1 if σ varies as $1/v$, while for nuclides with resonances in the thermal neutron energy range the g-factors are different from unity and they will be temperature dependent. The Zr isotopes measured in this work do not have resonances in the thermal neutron energy range, their g-factors are reported in [78].

(5) The total widths of the resonances have to be much smaller than the temperature kT.

(6) Bound state resonances, direct capture and the $1/\sqrt{E}$ component from distant resonances have to be treated separately.

For a more detailed description refer to Beer at al. [76].

Chapter V Data analysis and results

5.1 Introduction

In this chapter the experimental results for the ^{90,91,92,93,94,96}Zr(n,γ) measurements are presented. The different aspects of the analysis performed are described in detail, from the determination of the Weighting Function to the measurement and subtraction of the background. The extracted kernels in the resolved resonance region are given as well as a comparison with previous data.

5.2 Samples

The Zr samples were prepared from ZrO_2 powder, the enrichment and the sample characteristics, as thickness, mass and impurities are reported in Table 5.1. The oxide powder was pressed to a pellet 22 mm in diameter; this pellet was then encapsulated in a very thin aluminum can with a total weight of about 300 mg.

Traces of Hf, Sn, Na, Mg, Al were also present in the samples. Although these impurities were below 0.01%, their contribution to the measured capture yield was not negligible and had to be considered in the data analysis. For example, the significant resonances below the first ^{90}Zr resonance at 3.86 keV must be attributed to contaminating Hf and Sn isotopes (see Fig.5.1).

Additional Au and Pb samples of the same diameter were used for repeated neutron flux measurements and background runs throughout the experiment.

Table 5.1: Sample characteristics

Sample	Form	Isotopic composition (atomic %)						Thickness
		^{90}Zr	^{91}Zr	^{92}Zr	^{93}Zr	^{94}Zr	^{96}Zr	(atoms/b)
^{90}Zr	$Zr0_2$	97.7	0.87	0.6	0.00	0.67	0.16	0.00353
^{91}Zr	$Zr0_2$	5.43	89.9	2.68	0.00	1.75	0.24	0.00181
^{92}Zr	$Zr0_2$	4.65	1.62	91.4	0.00	2.03	0.30	0.00173
^{93}Zr	$Zr0_2$	2.29	18.61	18.95	19.98	20.50	19.67	0.00832
^{94}Zr	$Zr0_2$	4.05	1.18	1.93	0.00	91.8	1.04	0.00254
^{96}Zr	$Zr0_2$	19.41	5.21	8.2	0.00	8.68	58.5	0.00427
^{208}Pb	metal							0.00299
^{197}Au	metal							0.00149

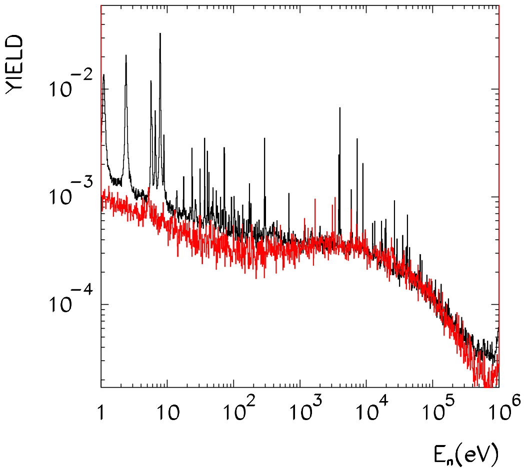

Figure 5.1: The $^{90}Zr(n,\gamma)^{91}Zr$ normalized yield (black) and the overall background (red)

5.3 Data analysis

The data reduction and analysis requires a careful consideration of many aspects. The main steps can be summarized as follows:

- Energy calibration of the detectors;

- Choice of suitable cuts for electronic noise rejection and for the rejection of the neutron signal at higher energy;
- Calculation of the weighting functions;
- Control of the stability of the measurement chain (via the Au measurement)
- Estimation of the different background components and their subtraction.

It should be noticed that the whole procedure has to be applied not only to the Zr samples, but also to the Au sample used for absolute normalization, and to any other sample used in the measurement.

The energy calibration of the detectors was performed with three γ-ray sources: ^{137}Cs, ^{60}C and Pu/C for the high energy region. For an accurate calibration, the response of the detectors was simulated for the three sources and the deposited energy was convoluted with the detector resolution. The channel corresponding to the half maximum of the Compton edge was used for energy calibration. The corresponding energies extracted from the simulation are: 0.542 MeV for the ^{137}Cs, 1.136 MeV for the ^{60}Co and 6.034 MeV for the Pu/C. A first order polynomial fitted very well the three points for all detectors, implying that the detector responses are linear at least up to 6 MeV.

For an accurate determination of the capture cross sections, it is important to apply conditions that allow to identify the capture γ-rays with a well defined threshold which allows to reject spurious events, such as those generated by electronic noise. A software threshold of 200 keV for n_TOF detectors and 350 keV for GELINA detectors, was applied in the analysis and considered in the determination of the weighting functions. It was found that this threshold is able to completely eliminate the electronic noise, which was in some cases affecting the measurement.

5.4 Determination of the capture yield

As described in § 4.2, the analysis of the C_6D_6 data for capture cross section determination relies on the Pulse Height Weighting Function method. The weighting functions for all the samples used in the Zr experiment, were obtained from simulation of the detector response performed with GEANT 3.21 and GEANT 4, for n_TOF, and MCNP4A, for GELINA, with a realistic replica of the experimental apparatus and including the resolution of the detector and applied light-output threshold.

After simulating the detector response for different γ-ray energies a least-square fit method is applied to extract the weighting function. The parameters of a 4th order polynomial used as weighting function, resulting from the least-square method, are reported in Table 5.2.

Table 5.2: parameters of the 4th degree polynomial used as weighting function, the parameters are part of the expression: $y=a_0+a_1x+a_2x^2+a_3x^3+a_4x^4$

Isotope	a_o	a_1	a_2	a_3	a_4
^{90}Zr	-3.86	45.36	1.17	1.21	-0.106
^{91}Zr	0.426	35.89	6.06	0.34	-0.047
^{92}Zr	-4.099	46.93	1.06	1.2	-0.965
^{93}Zr	-7.44	49.75	0.72	1.11	-0.098
^{94}Zr	5.01	48.90	-1.25	1.58	-0.109
^{96}Zr	1.19	35.28	6.19	0.34	-0.055
^{197}Au	-4.32	45.44	1.38	1.02	-0.105

Following the procedure described in § 4.6.1 the experimental capture yield is obtained from the measured and weighted count rate N^w as in equation 4.26.

The neutron number N_n can be calculated as the ratio between the nominal proton bunch 7×10^{12}, and the product of the protons employed in the measurements times the isolethargic neutron flux per bunch dN/dlnE. The total proton pulse intensity is registered at n_TOF by the Wall Current Monitor, the values registered showed too large deviations from some proton pulse and therefore, the silicon monitor, see § 3.3, information was used to renormalize between measurements.

An accurate determination of N_n, which takes in account also the sample dimensions is obtained from the reference measurement with a Au sample, see § 4.4.1, the parameter A of the equation 4.31 is the normalization factor. It relates directly the measured yield with the calculated yield.

Table 5.3 Normalization factors calculated from the saturated resonance at 4.9 of the Au.

Isotope	A
^{90}Zr	0.662(7)
^{91}Zr	0.661(7)
^{92}Zr	0.662(7)
^{93}Zr	0.572(6)
^{94}Zr	0.658(7)
^{96}Zr	0.660(7)

The values of the normalization factor A obtained from the fit of the saturated resonance at 4.9 eV of the Au are shown in Table 5.3. The quoted uncertainties include 1.5% from the weighting function.

The differences between the values of A, for the different isotopes of the Zr, reflect the fact that the measurements where done in different time, so they take in account any small modification of the experimental setup, as the positioning of the detector respect to the sample, or the small difference in the volume of the liquid scintillators. In particular in the case of ^{93}Zr, where A shows the larger difference, the measurement was done in 2004 while the other measurements where performed in 2003. At the end of the first set of measurements, all the stable Zr isotopes, the detectors were dismounted and emptied, for the measurement of the ^{93}Zr the detectors were refilled and mounted 2.15 m downstream, respect to the previous position, to allowed the TAC in the experimental area.

Figure 5.2 shows the capture yield measured in the ^{93}Zr experiment. The two C_6D_6 detectors were summed together. In the case of the n_TOF detectors a difference of ≈ 10% was observed between the count rate of the two detectors. Since all conditions in the analysis were kept the same, the difference is due to a different efficiency of the two detectors, probably due to a different volume of the C_6D_6 scintillator. Although the Weighting Functions were done for two detectors of the same active volume, the use of an overall normalization factor extracted from the Au sample accounts completely for the different efficiency.

It should be noted that, for background subtraction (see § 5.5), the spectrum of the Al container has to be corrected for the Weighting function of the sample from which it is being subtracted. Fig 5.3

shows the spectrum of the Al container of the ^{93}Zr sample, the C and Pb samples all processed with the weighting functions of ^{93}Zr.

5.4.1 Background determination

As described in § 3.2.3 and § 3.3 several sources of background affect the capture cross section determination, with different contribution in different energy regions. Together with the ambient background (which is observed without sample in the beam), spurious counts are generated by the Al-can containing the samples, by neutrons and by in-beam γ-rays scattered by the sample. For an accurate determination of the cross section, each of those components has to be evaluated.

The first two components, i.e. the ambient background and the one generated by the Al-can, were jointly estimated by means of an empty container similar to the one hosting the sample.

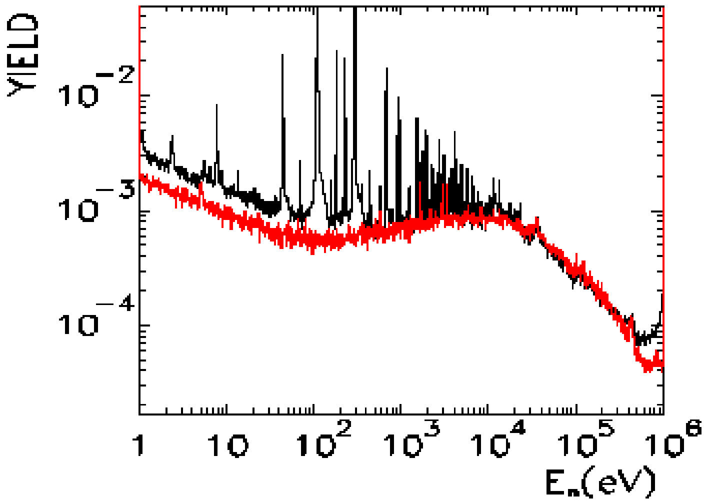

Figure 5.2: The ^{93}Zr(n,γ)^{94}Zr normalized yield (black) and the overall background (red)

Other sources of background that have to be taken into account are the sample-scattered neutrons and the γ-ray contamination in the neutron beam. These background components were evaluated by performing two other measurements, on a C and ^{nat}Pb sample. Both of these isotopes are characterized by a very low capture cross section, morever:

- The measurement with C sample can be used to estimate the background due to the sample-scattered neutrons. To take in account the difference between the C sample and the Zr sample the elastic cross section of the two samples has to be considered, therefore the neutron background can be written as:

  $$B_n = (Y_C - Y_e) \times \frac{\sigma_{Zrel} \times n_{Zr}}{\sigma_{Cel} \times n_C}$$

  Where Y_c and Y_e are the C and empty can capture yield respectively, σ_{Zrel} and σ_{Cel} are the Zr and C elastic cross section and n_{zr} and n_c are the Zr and C tickness in atom/barn;
- due to its large atomic number a ^{nat}Pb sample can be used to check for the background induced by the γ-ray contaminations in the neutron beam. Due to the different Z of the Pb and Zr, the Pb yield has to be scaled. The scaling factor f_s is obtained by MC simulation. The background due to the γ-ray contamination can be written as:

  $$B_\gamma = (Y_{Pb} - Y_e) \times f_s$$

The experimental yield of these measurements are reported in Figure 5.3. The reported spectra are normalized to the number of protons and scaled for the relative number of atoms/barn and for the elastic cross sections.

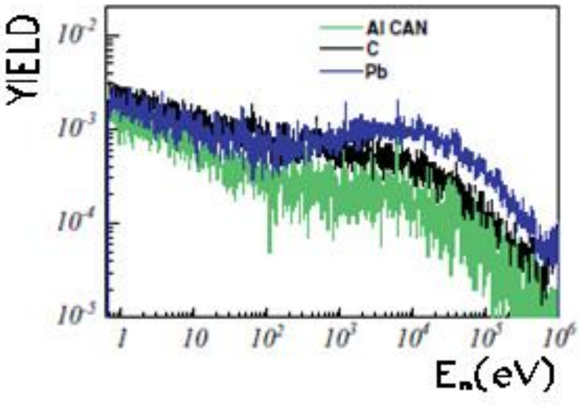

Figure 5.3 Normalized yield of the Individual background components in the neutron energy region between 1 eV and 1 MeV. Each component, except for the Al can, are corrected or scaled to account for the difference with the ^{93}Zr sample.

As can be seen the C and Pb backgrounds are close to the one measured with an empty Al-container, it confirms the low level of background. Indeed the yield of the background events is of the order of 10^{-3}.

Figure 5.2 shows the results for ^{93}Zr (black histogram) and the total background (in red) calculated as:

$$B = B_n + B_\gamma + Y_e$$

5.5 Uncertainties estimation

The total uncertainty in the yields consists of several contributions that can be identified in the analysis procedure. An important source comes from the determination of the normalization factor; its uncertainty is less than 2% supposing that no supplementary effects are involved due to difference between the γ-ray spectra of Au and Zr.

The additional uncertainties are related to the background subtraction, the dead-time and the pile-up corrections. Since the magnitude of each correction is among 0.1 and 5%, the overall uncertainty on the normalization can be assumed to be around 2%. An uncertainty of 2-3% is related to the determination of the shape of the neutron flux. Adding up these components the overall uncertainty is around 3%. To this uncertainty the statistical one has to be added.

5.6 Resonance analysis

Resonances were analysed in the Reich-Moore approximation with the R-matrix code SAMMY [75]. The corrections for Doppler broadening of resonance widths due to the thermal motion, for the energy resolution of the neutron beam, for isotopic and chemical sample impurities, and for self-shielding and neutron multiple scattering, are considered in the fits with this code. The Doppler broadening was treated by a free gas model assuming a temperature of 300 K. The effect of potential scattering was calculated using the scattering radius from [79]. The resolution function of the n_TOF neutron beam becomes important at energies above 1 keV and leads to low energy tails in the resonance shapes (see Fig 3.9).

The neutron widths Γ_n and the spin assignments values listed in the data libraries [79, 80], which were derived from transmission measurements [81, 86], have been adopted as fixed values in the fits, whereas the resonances energies E_r and the radioactive widths Γ_γ were considered as free fit parameters. For each resonance the capture kernel has been calculated.

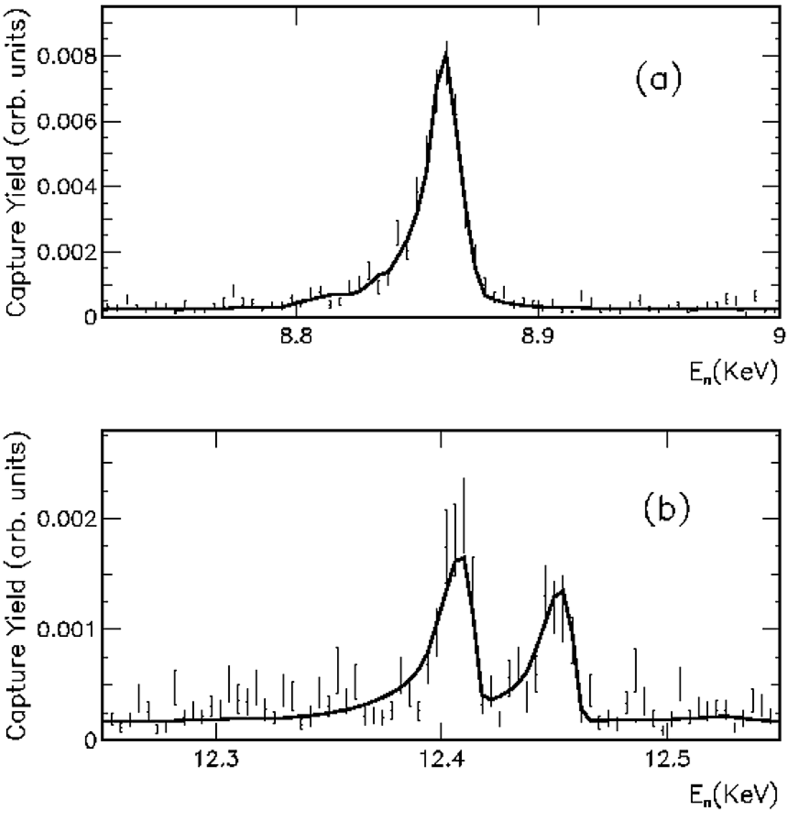

Figure 5.4 Examples for fits of ^{90}Zr resonances with the R-matrix code SAMMY. (a) for a previously reported resonance. (b) two small resonances, which were observed for the first time.

5.7 ^{90}Zr measurement

^{90}Zr represents one of the most important isotopes to be investigated. ^{90}Zr is a magic neutron nucleus and it behaves as bottle neck of the s-process flow. The status of the ^{90}Zr cross section is not satisfactory, because different measurements have reported uncertainties between 6 and 25%, but exhibit discrepancies up to a factor of two.

5.7.1 Resonance analysis

Resonances observed in the neutron energy range from 0.01 to 70 keV were analysed; the resonance parameters obtained by SAMMY analyses of the background subtracted capture yield are listed in Table 5.3 [83].

Among the 45 analysed resonances, 10 resonances and one doublet around 13.4 keV were identified for the first time [82,84]. The spin assignments in the fits with the SAMMY code were adopted from evaluated parameter sets [79, 80]. Examples illustrating the quality of the SAMMY fits are shown in Fig 5.4.

Table 5.3: ^{90}Zr extracted E_R, K

E_r (keV)	J	l	K (eV)	ΔK (%)
3.6812(4)	1/2	0	0.077	3.0
4.00832(6)	3/2	1	0.13	4.0
7.2603(2)	3/2	1	0.287	3.0
8.8851(4)	1/2	1	0.211	3.4
9.60204(7)	1/2	1	0.19	7.6
12.20802(2)	1/2	0	0.0067	9.4
[a]12.39980(7)			0.031	6.5
[a]12.44288(1)			0.026	6.6
[b]13.365(3)	1/2	0	0.068	7.9
[a]13.4439(1)			0.053	8.8
[a]16.894(1)			0.092	6.5
[a]16.92958(2)			0.024	8.4
16.9792(1)	1/2	0	0.018	9.3
17.402(2)	1/2	1	0.162	7.5
[a]19.07930(1)			0.017	7.5
19.713(2)	1/2	1	0.267	5.5
26.469(3)	3/2	1	0.124	8.4
26.538(1)	3/2	1	0.41	6.0
28.827(3)	3/2	1	0.27	8.8
35.356(4)	1/2	0	0.579	6.2
39.507(3)	3/2	1	0.329	7.2
40.40(1)	1/2	1	0.162	9.0
41.39(1)	3/2	1	1.96	5.4
[a]42.0699(1)			0.68	8.5
42.21(6)	1/2	0	0.203	9.6
[a]42.455(6)		0	0.062	8.7

E_r (keV)	J	l	K (eV)	ΔK (%)
a42.64(2)			0.20	8.7
44.822(8)	3/2	1	0.627	7.2
[a]53.264(7)			0.025	9.7
53.371(8)	1/2	0	0.088	9.2
53.672(6)	1/2	0	0.134	7.7
54.353(1)	1/2	1	0.070	7.7
54.546(1)	1/2	1	0.117	7.1
55.80(2)	1/2	1	0.192	9.3
56.52(1)	1/2	1	0.244	8.7
57.790(4)	1/2	0	0.257	6.9
[a]58.311(8)			0.174	8.9
61.900(2)	3/2	1	0.313	8.1
62.410(2)	1/2	1	0.128	8.8
[a]63.9419(3)			0.133	8.3
64.95(6)	1/2	1	0.079	9.9
[a]65.18(2)			0.938	7.8
65.362(2)	1/2	0	0.212	7.6
68.591(7)	3/2	1	0.802	9.1

(a)New

(b) Doublet, identified as a single resonance in previous measurements [79,84]

The extracted values for K are on average 15% smaller than those reported in a previous measurement [84] as illustrated in Fig 5.5. Compared to the evaluated parameter set of Ref. [79], which is based on all available experimental data, the results are approximately 10% lower.

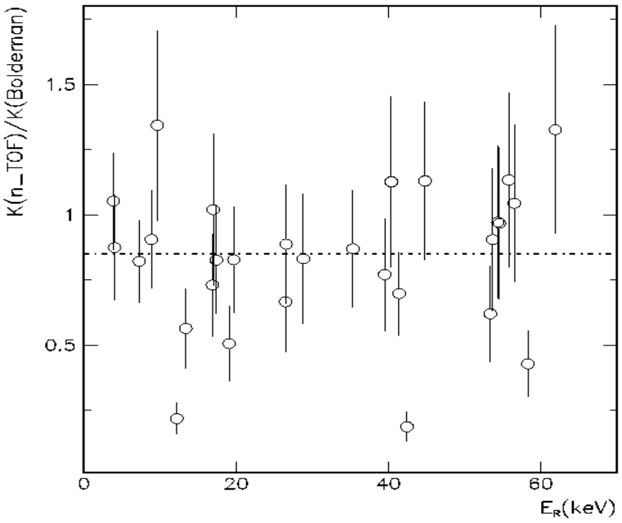

Figure 5.5 Ratio between ^{90}Zr capture kernels obtained in the present measurement and those of Ref.[85]. The average is given by the dashed-dotted line.

5.8 ^{91}Zr measurement

In the s-process path, ^{91}Zr follows the magic neutron isotope ^{90}Zr and belongs, therefore, to the critical mass region around N = 50, where the Zr assumes a key role in a comprehensive discussion of the relative contributions of the s-process components. Experimental (n,γ) cross sections with uncertainties of $\leq$ 3 to 5% are required for discriminating between different stellar model approaches [86].

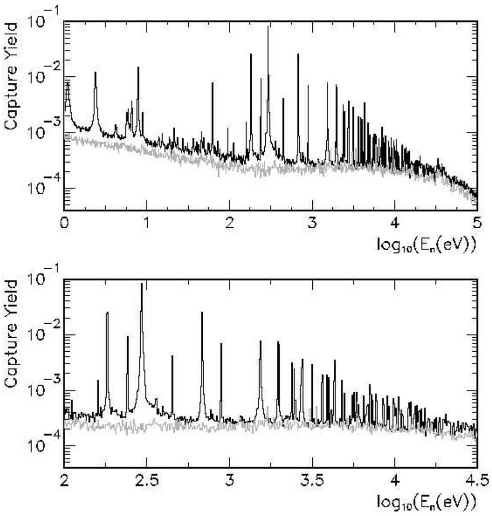

Figure 5.6: ^{91}Zr capture yield (black) and overall background (grey) between 1 eV and 100 keV. Most of the resonances below 150 eV are due to Hf and Sn contaminations in the sample.

5.8.1 Resonance analysis

The capture yield of ^{91}Zr and the overall background are presented in Fig. 5.6. Resonances observed in the neutron energy range up to 26 keV were analysed [87].

For the scattering radius the value of 7.2 fm from Ref. [79] was used. In total, 157 resonances could be analysed in the investigated energy range. Compared to previous measurements [80, 81, 89] new resonances were observed for the first time. The results of the resonance analyses are listed in Table 5.4. Examples illustrating the quality of the fits are shown in Fig. 5.7.

As a consequence of the relatively small capture cross section of ^{91}Zr, the limited counting statistics contribute significantly to the overall experimental uncertainty. Because of the decreasing signal/background ratio, the statistical uncertainty grows with neutron energy from ≈ 3% at 150 eV to ≈ 6% at 26 keV. Beyond 26 keV, resonance analyses are challenged by counting statistics.

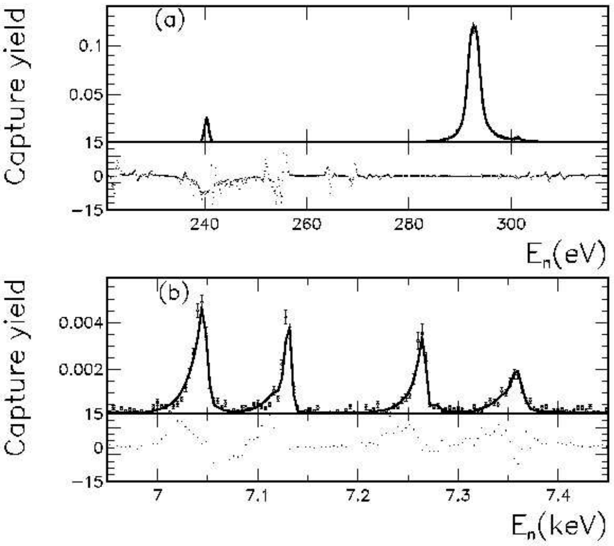

Figure 5.7: Examples for fits of ^{91}Zr resonances with the R-matrix code SAMMY and residuals to the fit (in percentage). The resonance at 7.26 keV is not reported in databases of Refs. [79, 80, 88].

The present results can be compared with existing measurements in the energy range up to 20 keV. The only information on resonance parameters was reported more than 30 years ago by Musgrove et al. [80]. Other data are incomplete [81,89,91]. The energy region covered by the only recent measurement [92] overlaps with the present data above 15 keV.

Table 5.4: ^{91}Zr kernels extracted from the n_TOF capture data.

E_r (eV)	J	l	K (eV)	ΔK (%)
159.43(2)	1	1	9.24×10^{-4}	3.7
181.987(2)	4	1	4.99×10^{-3}	0.5
240.404(6)	2	1	1.61×10^{-3}	1.3
292.702(5)	3	0	5.89×10^{-2}	0.4
449.76(1)	3	1	2.03×10^{-3}	1.9
681.76(1)	3	0	5.52×10^{-2}	0.7
893.14(1)	3	1	1.50×10^{-2}	2.1
1532.3(2)	2	0	5.69×10^{-2}	2.3
1533.28(4)	3	1	4.24×10^{-2}	4.4
1954.48(3)	3	1	7.55×10^{-2}	3.9
1998.78(6)	3	0	1.15×10^{-2}	3.4
2013.18(3)	3	1	5.49×10^{-2}	2.7
2361.4(6)	2	0	2.86×10^{-3}	7.5
2385.16(5)	3	1	4.05×10^{-2}	5.3
2476.7(1)	2	0	4.89×10^{-2}	2.4
2727.1(2)	3	0	7.11×10^{-2}	2.7
2757.8(1)	1	1	1.81×10^{-2}	6.0
2763.62(6)	2	1	4.90×10^{-2}	3.4
3158.99(6)	4	1	7.59×10^{-2}	2.4
3612.4(1)	4	1	3.16×10^{-2}	5.5
3644.29(7)	3	1	5.15×10^{-2}	4.4
3864.0(1)	3	1	6.15×10^{-2}	7.2
[b]3866.7(5)	(3)	(0)	1.36×10^{-2}	9.5
4007.5(1)	3	1	5.78×10^{-2}	5.2
4278.6(1)	2	0	3.97×10^{-2}	3.9
4327.2(1)	1	1	0.15	3.0
4749.0(1)	2	1	6.80×10^{-2}	4.4
4979.6(2)	3	0	4.27×10^{-2}	4.6
5360.3(1)	3	1	1.07×10^{-2}	5.8
5527.6(6)	2	0	5.49×10^{-2}	5.1
5634.0(2)	3	1	6.01×10^{-2}	4.0
5825.1(3)	4	1	4.58×10^{-2}	5.6
6090.51(5)	4	1	3.40×10^{-2}	6.5
6169.18(3)	4	1	4.95×10^{-3}	8.8
[b]6179.04(4)			5.08×10^{-3}	9.0
6472.6(3)	3	0	5.82×10^{-2}	4.6
6759.5(4)	2	1	2.76×10^{-2}	6.3
6859.0(3)	2	0	3.95×10^{-2}	5.5
7040.5(3)	4	1	0.125	3.3
7125.9(3)	3	1	7.83×10^{-2}	4.2
[a]7259.8(4)			6.44×10^{-2}	5.5
7354.2(5)	3	0	6.97×10^{-2}	4.7
7755.5(4)	2	1	0.121	5.5
7766.0(8)	1	1	4.86×10^{-2}	7.5
8498.7(4)	3	0	6.15×10^{-2}	5.6
8516.9(3)	2	1	7.77×10^{-2}	4.9
8944.7(5)	3	0	4.11×10^{-2}	6.0
9035.0(4)	4	1	6.63×10^{-2}	6.0

E_r (eV)	J	l	K (eV)	ΔK (%)
9098.4(4)	3	1	6.27×10^{-2}	5.4
9226.6(4)	3	1	4.74×10^{-2}	5.8
9301.0(6)	2	0	3.18×10^{-2}	6.5
9826.7(3)	2	0	8.47×10^{-2}	5.4
9870.8(8)	2	0	5.07×10^{-2}	6.3
9989.5(4)	4	1	9.80×10^{-2}	4.6
10124.8(6)	2	1	7.52×10^{-2}	5.5
10517.7(6)	4	1	6.75×10^{-2}	5.8
10550.4(4)	3	1	7.59×10^{-2}	5.6
10701.8(5)	2	1	6.47×10^{-2}	6.0
10734.9(8)	2	0	3.64×10^{-2}	6.4
[a]11024.34(4)			1.42×10^{-2}	7.6
11024.34(4)	3	1	6.72×10^{-2}	6.1
11117.5(4)	2	0	2.81×10^{-2}	7.0
11123.2(9)	2	1	4.59×10^{-2}	8.8
11230.7(7)	3	0	5.31×10^{-2}	6.4
12102.1(5)	3	1	9.07×10^{-2}	5.7
[a]12150.26(3)			1.96×10^{-2}	8.0
12217.9(5)	4	1	0.154	4.7
12318.6(7)	3	0	6.59×10^{-2}	6.3
[b]12511.8(4)			2.02×10^{-2}	8.8
12546.(2)	2	1	0.121	8.7
12559.2(6)	2	1	8.33×10^{-2}	8.4
12924.(4)	2	1	3.60×10^{-2}	8.7
12933.(4)	3	0	2.89×10^{-2}	9.1
13151.9(8)	1	1	7.56×10^{-2}	2.8
13255.5(9)	3	1	6.01×10^{-2}	7.0
13301.0(9)	3	0	8.57×10^{-2}	6.7
[a]13348.(4)			2.21×10^{-2}	9.2
13567.3(9)	2	0	4.83×10^{-2}	7.0
13694.0(7)	3	1	0.156	5.3
13802.(1)	3	0	5.94×10^{-2}	7.4
[a]13934.5(2)			1.39×10^{-2}	9.1
14074.(1)	3	0	0.109	6.4
14187.(1)	1	1	3.88×10^{-2}	7.4
14236.(1)	2	1	5.67×10^{-2}	7.0
[a]14485.(1)			6.59×10^{-2}	9.8
14582.(1)	4	1	0.132	6.0
[a]14811.(2)			1.05×10^{-2}	8.9
14839.(1)	2	0	5.12×10^{-2}	7.8
15175.(1)	2	1	0.137	6.2
15230.(2)	2	0	4.71×10^{-2}	8.4
[a]15763.3(1)			6.57×10^{-2}	7.2
15777.3(3)	3	0	2.12×10^{-2}	8.9
[a]15937.(4)			7.29×10^{-2}	9.8
15978.(1)	4	1	8.58×10^{-2}	7.2
16190.(3)	2	1	8.58×10^{-2}	8.1
16699.(1)	2	0	6.17×10^{-2}	8.3
[a]16826.25(5)			3.26×10^{-2}	7.5
16972.(6)	3	1	3.39×10^{-2}	9.1

E_r (eV)	J	l	K (eV)	ΔK (%)
17062.(2)	2	1	2.61×10^{-2}	7.8
[b]17424.(3)			4.50×10^{-2}	9.1
17454.(2)	3	1	7.71×10^{-2}	8.1
17800.(1)	4	1	0.107	6.5
[b]18543.(1)	3	1	7.05×10^{-2}	7.5
18584.03(1)			1.75×10^{-3}	10.
18632.(1)	2	1	0.212	6.0
19487.(1)	4	1	0.166	6.5
19590.2(1)	2	1	4.97×10^{-2}	7.1
19760.(2)	3	1	8.16×10^{-2}	7.6
19800.(2)	3	0	5.65×10^{-2}	6.8
20012.7(1)	4	1	5.66×10^{-2}	6.7
20058.7(1)	3	0	4.85×10^{-2}	7.8
20171.(2)	3	0	0.101	7.8
20241.(3)	4	1	0.107	9.1
20250.(4)	2	0	1.33×10^{-2}	7.0
20309.5(1)	2	1	5.56×10^{-2}	7.8
20402.8(5)	3	1	6.79×10^{-2}	6.8
20626.(2)	3	0	7.89×10^{-2}	8.5
20913.(1)	4	1	0.134	8.3
21234.(1)	3	0	7.33×10^{-2}	9.5
[a]21277.(1)			6.77×10^{-2}	9.2
21345.8(2)	4	1	1.15×10^{-2}	7.7
[a]21396.(3)			2.30×10^{-2}	8.1
21476.(2)	1	1	0.108	9.2
21747.(3)	2	0	0.107	7.7
21782.(2)	3	1	3.29×10^{-2}	8.1
[a]22113.(1)			3.28×10^{-2}	9.2
22161.(4)	3	0	3.91×10^{-2}	8.6
[a]22276.(2)			3.47×10^{-2}	8.2
[a]22374.9(3)			2.37×10^{-2}	6.9
[a]22454.(2)			5.11×10^{-2}	7.3
[a]22513.(2)			4.27×10^{-2}	8.0
22598.(1)	4	1	6.80×10^{-2}	6.5
22744.(4)	2	0	7.19×10^{-2}	8.7
[a]22796.(2)			0.105	7.3
22820.(6)	4	1	6.10×10^{-2}	9.8
[a]22850.7(7)			3.90×10^{-2}	7.0
[a]22975.(2)			9.11×10^{-2}	9.0
[a]23231.(3)			1.96×10^{-2}	9.2
23318.(4)	2	1	3.46×10^{-2}	9.5
[a]23512.(3)			2.51×10^{-2}	9.4
23695.(5)	4	1	5.68×10^{-2}	7.9
23785.(2)	2	0	4.67×10^{-2}	6.7
[a]23925.(2)			8.84×10^{-2}	9.3
[a]24190.(3)			9.68×10^{-2}	8.7
24236.(2)	3	1	0.161	7.7

E_r (eV)	J	l	K (eV)	ΔK (%)
[a]24775.(3)			6.74×10^{-2}	7.6
24800.(3)	2	1	5.56×10^{-2}	8.9
[a]24852.(6)			1.69×10^{-2}	9.4
[a]24892.(4)			4.91×10^{-2}	9.1
24924.(2)	2	1	0.11	8.0
[a]24996.(2)			1.52×10^{-2}	7.2
25222.(5)	2	0	3.93×10^{-2}	8.4
25265.1(2)	3	1	6.99×10^{-2}	7.9
25698.1(4)	4	1	7.96×10^{-2}	7.0
25990.(2)	3	0	0.160	7.1
[a]26126.(3)			7.27	8.1

Uncertainties are given as: 159.43(2) ≡ 159.43±0.02.

a) New, not present in the compilations of Ref. [79, 90].

b) Doublet, identified as a single resonance in previous measurements [79, 90].

These data have been used to evaluate the average neutron capture cross section above 26 keV. The present results for the capture kernels are compared in Fig. 5.8 with the values given in Ref. [80].

Fig. 5.8 clearly indicates that the present capture kernels are ≈10% lower on average.

5.9 ^{92}Zr measurement

The astrophysical importance of improved MACS for ^{92}Zr at stellar energies is related to the overabundance of ^{92}Zr reported in Ref. [8]. Using the previously recommended MACS values [6] it was calculated that 93% of solar ^{92}Zr was of s-process origin, notwithstanding the expected r-process contribution of 10% inferred from the neighboring isotopes. Therefore, the MACS value of ^{92}Zr needs to be verified in order to refine the constraints for the s-process models and to study the consequences for the r-process component. A better determination of the solar ^{92}Zr production is also related to the potential interpretation of the ^{92}Nb/^{92}Zr pair as a cosmochronometer [93] for the early solar system.

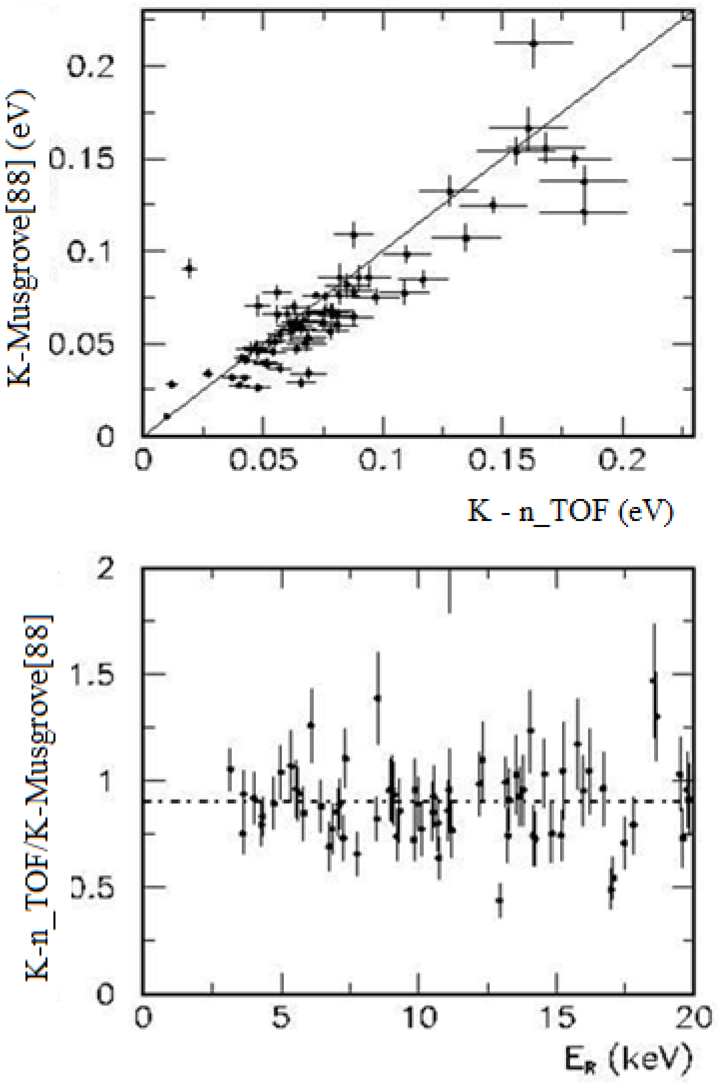

Figure 5.8: Upper panel: ^{91}Zr capture kernels from Ref. [80] compared to the present results. Lower panel: Ratio of the ^{91}Zr capture kernels from Ref. [80] and the present results versus resonance energy. The average value is indicated by the dotted line.

Existing experimental data mainly come from relatively old measurements [81, 82, 85, 94, 95]. Ref. [95] lists the energy of the resonances up to 40 keV and gives capture kernels up to 10 keV (with associated uncertainties between 10 and 20%); Ref. [82] lists some resonances (15 on 52 known in this range) up to 52 keV, but gives detailed information only for 4 strong resonances. Ref. [94] lists 5 resonances, but the first one has been recognized not belonging to ^{92}Zr. A recent publication [92] does not present the resonance analysis. The only rich information available is that present in the mid-1970 publication [85], already revisited by evaluators [79, 88].

5.9.1 Resonance analysis

The capture yield of ^{92}Zr and the overall background are presented in Fig. 5.9. Resonances observed in the neutron energy range up to 40 keV were analysed [96]. The effect of potential scattering was theoretically calculated using a radius of 7.2 fm [79].

The analysis was limited to the energy range between 2 and 40 keV because the statistical precision of the capture data was poor at higher energies. Among the 44 resonances which were analysed, three resonances were identified for the first time.

The deduced E_R (resonance energy) together with the capture kernel are listed in Table 5.5.

Examples illustrating the quality of the fits are shown in Fig. 5.10.

Due to the relatively low capture cross section of ^{92}Zr the overall uncertainties of the results are dominated by the counting statistics. The statistical uncertainty grows with neutron energy from ≈ 4% at 150 eV to ≈ 6% at 40 keV.

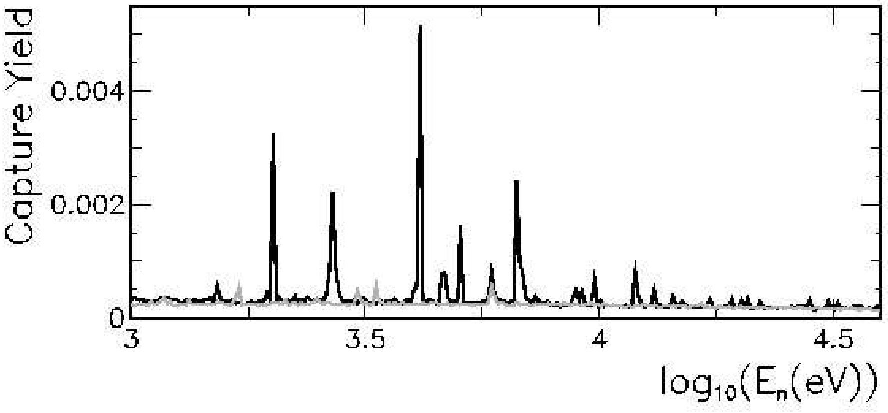

Figure 5.9: ^{92}Zr capture yield (black) and overall background (gray) in the investigated energy range (1 keV < En < 40 keV).

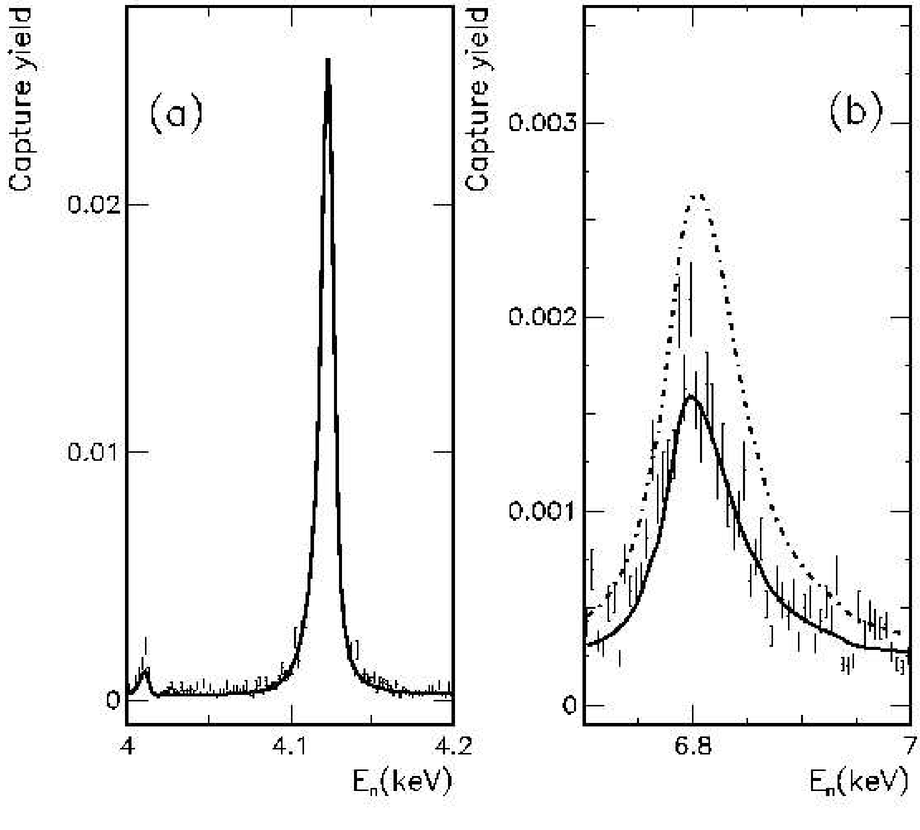

Figure 5.10: Examples for fits of ^{92}Zr(n,γ) resonances with the R-matrix code SAMMY (full lines). The left panel shows the resonance at 4.2 keV, which turned out to be most important for the calculation of the Maxwellian averaged cross section The right panel shows the resonance at 6.8 keV, where the present results deviate significantly from the resonance parameters listed in Ref. [85] (dashed-dotted line).

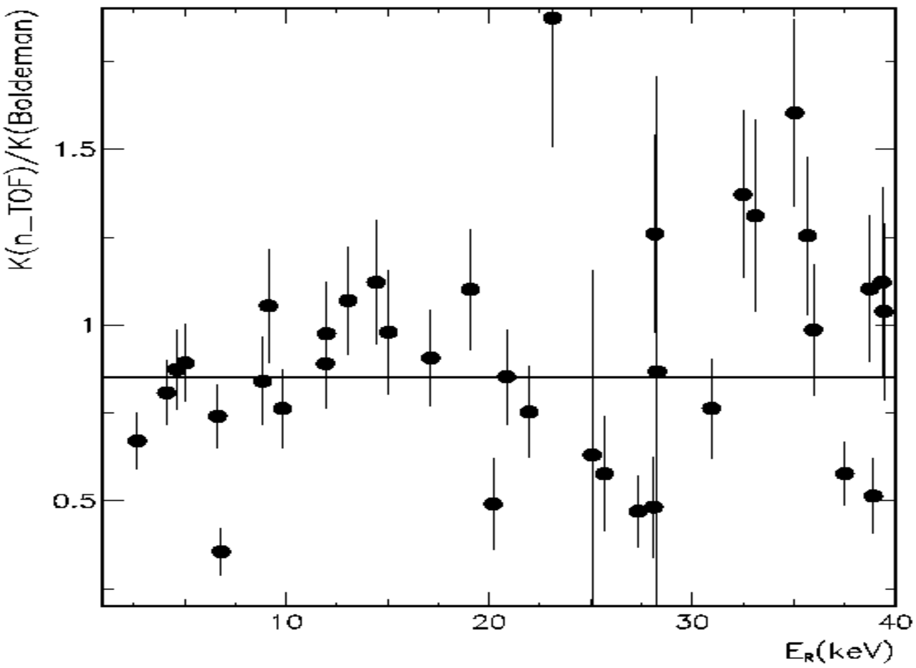

Figure 5.11: Ratio between capture kernels obtained in the present measurement of ^{92}Zr and those given in Ref. [85]. The average value is indicated by the solid line

The present values of the kernels are 15% smaller compared to the results of Ref. [85] as shown in Fig. 5.11.

TABLE 5.5: ^{92}Zr(n,γ) resonance parameters extracted from the fit of the n_TOF capture data.

E_r (eV)	J	l	K (eV)	ΔK (%)
2012.91(3)	3/2	1	0.0443	2.4
2689.4(4)	1/2	0	0.115	1.7
4121.2(1)	3/2	0	0.460	1.3
4639.6(5)	1/2	0	0.100	3.1
[a]4653.69(3)	-	-	(0.0089)	(82.)
5045.7(1)	1/2	1	0.142	2.3
6638.9(1)	3/2	1	0.363	2.0
6811.(3)	1/2	0	0.132	9.0
8845.0(4)	1/2	1	0.107	4.8
9136.7(5)	1/2	0	0.0970	5.2
9821.0(3)	3/2	1	0.160	4.6
11943.7(3)	3/2	1	0.240	4.1
12013.1(7)	1/2	1	0.195	5.1
13065.7(4)	3/2	1	0.224	4.3
14427.(1)	1/2	1	0.202	5.7
15027.9(8)	3/2	0	0.0980	8.0

E_r (eV)	J	l	K (eV)	ΔK (%)
[a]16941.0(1)	-	-	(0.020)	(83.)
17132.(1)	3/2	1	0.290	5.1
[a]17284.6(1)	-	-	(0.018)	(83.)
19076.(1)	3/2	1	0.308	5.6
20195.(1)	1/2	0	0.185	7.6
20846.(1)	1/2	0	0.299	5.8
21977.(1)	1/2	1	0.218	7.0
23114(10)	1/2	0	0.150	9.5
25078.2(1)	-	-	(0.030)	(74.)
25665.(4)	1/2	0	0.0750	19.
26236.(1)	-	-	(0.05)	(88.)
26776.(3)	3/2	1	0.22	9.5
27327.(5)	1/2	1	0198	12.
28098.(6)	3/2	1	0.14	20.
28167.(4)	1/2	1	0.26	12.
28282.(1)	-	-	(0.008)	(87.)
30398.(7)	1/2	0	0.072	23.
30932.(3)	3/2	1	0.473	8.5
32490.(3)	3/2	1	0.604	7.3
33094.(9)	1/2	0	0.10	11.
35035(20)	1/2	1	0.289	6.6
35677(12)	1/2	1	0.414	7.9
37507.(7)	1/2	1	0.185	5.2
38740(10)	1/2	1	0.121	8.8
38922(8)	3/2	1	0.20	11.
39345(9)	1/2	1	0.44	14.
39418(40)	1/2	0	0.12	14.

(a) New;
Uncertainties are given as 2012.89(4) ≡ 2012.89±0.04;

5.10 ^{93}Zr measurement

^{93}Zr is a radioactive isotope ($t_{1/2}$=1.5 × 10^5 yr). Due to its short half-life compared to the lifetime of low-mass stars (~10^9 yr) and the fact that the AGB phase occurs at the end of the star's life, ^{93}Zr in stars has to be synthesized locally and could not be inherited from other stars. On the other hand, the half-life of ^{93}Zr is long compared with s-process half-life, a few years; therefore it can be considered as stable in the s-process path.

The presence of ^{93}Zr in a stellar spectrum gives the indication of a binary star[4] or a so called extrinsic AGB star (mass transfer of s-rich material from the companion star of the binary system) .

5.10.1 Resonance analysis

The sample of ^{93}Zr used in the measurement had an activity of 92.5 MBq, for this reason it was encapsulated in an aluminum container with the same size and thickness as used for the other Zr samples, and sealed in a titanium container 0.2 mm thick.

To estimate the background due to the natural activity of the sample a dedicated measurement with no neutron beam was done. Fig 5.12 shows the capture yield of the sample (black) and the radioactive background (blue), the counts were normalized by the acquisition time, the ^{93}Zr weighting function and binding energy were used to extract the yield.

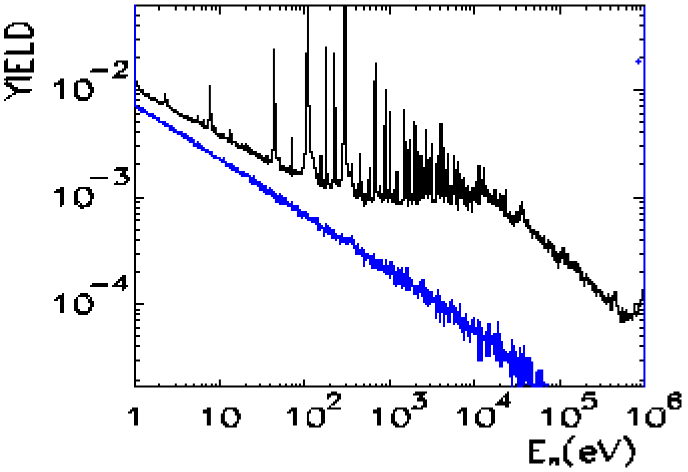

Figure 5.12 Capture yield of the sample used for the ^{93}Zr(n,γ) measurement (black) and background due to the activity of the sample

---

[4] A binary star is a star system consisting of two stars orbiting around their common center of mass. The brighter star is called the primary and the other is its companion star, or secondary.

In Fig 5.2 the capture yield is shown, radioactive background free, compared to the overall background due to the other sources of background discussed in § 5.4. Another difference with the other Zr isotopes measured in this work is the low enrichment in ^{93}Zr of the sample used. As can be seen from Tab 5.1 only 20% of Zr present in the sample was from the isotope ^{93}Zr. In Fig 5.17 the effect due to the low enrichment is shown. The presence of other Zr isotopes contamination was used to cross check the quality of the data analysis. Different sets of data were produced, one for each isotope of Zr present in the sample, where the proper weighting function and binding energy were used to produce the data set.

Traces of Hf, Mo, Sn, Na, Mg, Al were also present in the sample. Although these impurities were below 0.1%, their contribution to the measured capture yield was not negligible; in Fig 5.13 the effect of Mo is shown, and had to be considered in the data analysis.

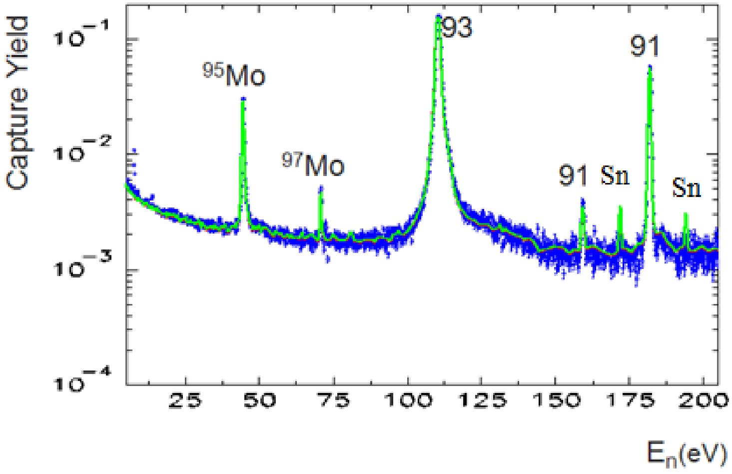

Figura 5.13 Capture yield of the sample of Zr in the neutron energy range 0,25 eV – 200 eV. Besides the contamination of the other Zr isotopes also the contribution due to other impurities, (Mo e Sn in the Fig) is clear. Although, the sample contains less than 1% of these elements, at low energy their contributions cannot be neglected.

The deduced E_R together with the capture kernels are listed in Table 5.6.

TABLE 5.6: ^{93}Zr(n,γ) kernels extracted from the fit of the n_TOF capture data

E_r (eV)	J	l	K (eV)	ΔK (%)
110.371(2)	2	0	29.11	0.18
225.034(4)	4	1	4.44	0.69
669.092(9)	2	0	16.81	1.06
693.261(8)	2	0	35.34	0.86
882.15(3)	3	1	2.57	3.26
934.34(1)	4	1	28.10	1.68
1010.72(1)	4	1	20.10	1.23
1237.89(4)	3	1	4.82	3.20
1285.24(4)	3	1	4.74	3.44
1497.9(1)	3	1	2.10	21.76
1574.71(3)	2	1	17.37	2.71
1642.26(3)	4	1	16.79	2.52
1708.06(8)	2	1	6.58	5.67
1743.2(2)	2	0	26.83	2.10
1802.42(3)	4	1	31.44	1.89
2053.30(6)	1	1	28.27	2.93
2116.34(8)	2	1	7.43	4.71
2209.3(1)	2	1	4.76	6.28
2320.15(6)	2	0	29.72	3.02
2358.8(1)	2	1	12.30	6.95
2404.1(2)	3	1	4.78	7.89
2610.77(6)	2	0	22.79	3.78
2767.5(4)	2	0	36.55	7.05
2898.54(6)	2	0	35.27	4.06
3008.8(1)	2	0	47.68	3.05
[a]3162.1(5)			51.29	14.44
3251.46(6)	3	0	59.71	4.26
3511.4(2)	2	0	33.18	4.11
3690.(1)	3	0	28.66	5.07
3698.3(2)	2	0	30.27	5.19
[a]3872.3(2)			42.53	6.27
3996.1(2)	2	0	36.53	4.61
4130.(1)	4	1	29.50	24.67
4156.0(2)	2	0	27.62	7.75
[a]4180.5(5)			48.52	13.31
4288.1(4)	3	1	9.30	27.59
(x)≈4300.9				
(x)≈4320.3				
4432.3(2)	2	0	20.35	7.02
4484.1(1)	2	0	46.13	4.71
4577.2(2)	2	0	35.30	4.49
4779.7(2)	2	1	19.11	7.02
5010.7(2)	1	1	71.75	3.85
5027.8(3)	1	1	35.24	7.41
5133.9(4)	2	0	35.59	6.17

E_r (eV)	J	l	K (eV)	ΔK (%)
5539.1(3)	1	1	31.27	8.44
5674.8(6)	1	1	21.25	10.34
5738.2(5)	2	0	30.30	9.17
5876.7(2)	3	1	5.89	100.10
(x)≈5921.42				
(x)≈5940.05				
6109.3(4)	2	1	17.08	18.76
[a]6148.0(4)			40.06	7.48
6207.4(5)	2	0	25.01	8.65
6339.0(3)	3	0	48.68	5.97
6376.4(4)	3	0	25.21	9.13
6620.(2)	3	0	6.35	46.55
6766.6(4)	2	0	54.99	8.27
6822.(2)	3	1	15.04	80.02
6977.1(2)	3	1	23.72	80.90
7073.5(5)	3	1	21.83	22.23
7169.5(5)	3	0	62.13	6.97
7407.2(8)	3	0	29.77	14.09
7587.1(6)	2	1	34.25	42.32
7772.(1)	3	0	32.81	26.06
7893.2(8)	3	0	34.69	14.27
7945.1(1)	3	0	94.71	9.71

Uncertainties are given as 110.371(2)≡110.371±0.002;
(a) New;
(x) Refers to not observed resonances;

In Tab 5.7, 5.8, 5.9, 5.10 the parameters, E_R and kernel are reported, for the isotopes ^{90}Zr, ^{91}Zr, ^{92}Zr, ^{94}Zr respectively obtained from the analysis of the sample used for the ^{93}Zr measurement compared with values obtained from the measurements with enriched samples.

The agreement is better than 3%.

TABLE 5.7: Comparison between the ^{90}Zr kernel from Tab 5.3, K_E, and the kernel extracted from the fit of the capture data of the sample used for the ^{93}Zr measurement where the ^{90}Zr enrichment is 2.3%.

E_r (eV)	K_E (meV)	K (meV)	ΔK (%)
3861	78.1	79.5	1.8
4008	131.8	130.	1.4

TABLE 5.8: Comparison between the ^{91}Zr kernel from Tab 5.4, K_E, and the kernel extracted from the fit of the capture data of the sample used for the ^{93}Zr measurement where the ^{91}Zr enrichment is 18.6%.

E_r (eV)	K_E (meV)	K (meV)	ΔK (%)
159.5	0.09	0.09	0.0
181.9	4.99	4.96	0.7
240.3	1.61	1.61	0.1
292.6	60.22	60.20	0.0
681.4	55.25	55.76	0.9
892.7	14.95	14.58	2.5

TABLE 5.9: Comparison between the ^{92}Zr kernel from Tab 5.5, K_E, and the kernel extracted from the fit of the capture data of the sample used for the ^{93}Zr measurement where the ^{92}Zr enrichment is 18.95%.

E_r (eV)	K_E (meV)	K (meV)	ΔK (%)
2012	45.09	46.09	2.1
2688	115.0	117.2	1.9
4119	440.3	440.0	0.1
4640	99.32	102.	2.7
5044	142.4	124.9	2.0

TABLE 5.10: Comparison between the ^{94}Zr kernel from Tab 5.11, K_E, and the kernel extracted from the fit of the capture data of the sample used for the ^{93}Zr measurement where the ^{94}Zr enrichment is 20.5%.

E_r (eV)	K_E (meV)	K (meV)	ΔK (%)
2240	66.52	64.71	1.2
4922	126	124.9	0.8

Because of the relatively low cross section of ^{93}Zr, an important uncertainty in the results is due to the limited counting statistics.

Due to the decreasing signal/background ratio, the statistical uncertainty grows with neutron energy from ≈ 4% at 100 eV to ≈7% at 8 keV. The present results can be compared with existing measurements [97, 98]. Ref. [97] gives information on resonance parameters, obtained in a neutron capture measurement performed at the Oak Ridge Electron Linear Accelerator with a pair of non-hydrogenous fluorocarbon liquid scintillators. The sample used in the measurements was similar, in Zr impurities, to the one used for this work. The contamination due to the other Zr isotopes in [97] was treated as background and therefore subtracted from the ^{93}Zr(n,γ)^{94}Zr yield. Fig 5.14 shows the comparison between the kernels of the two measurements. A difference of 35% in average was found.

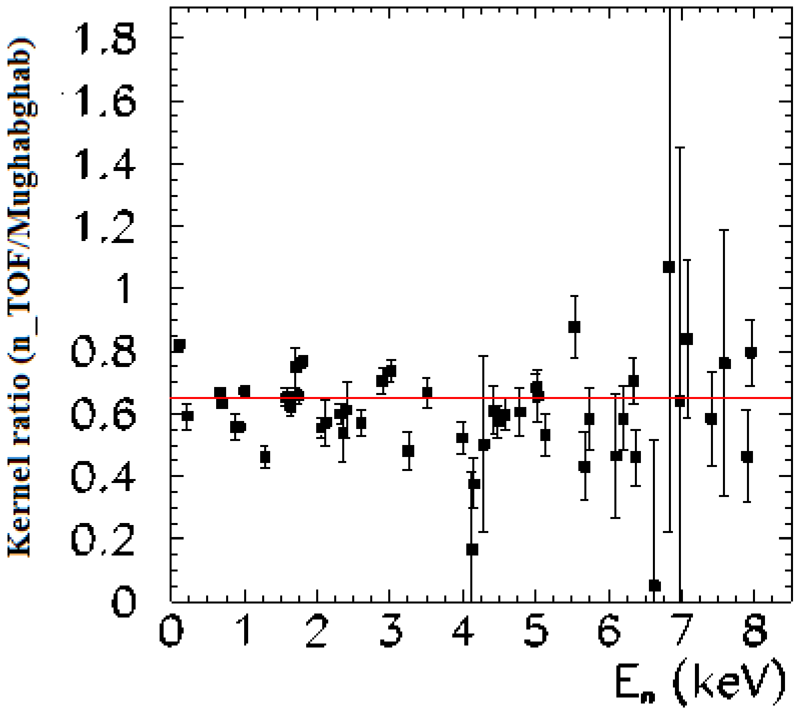

Figure 5.14: Ratio between ^{93}Zr capture kernel values extracted between the present measurement and the values reported in reported [79], versus resonance energy.

5.11 ^{94}Zr measurement

^{94}Zr is the last Zr isotope of the almost s-only chain; in particular Davis et al. [5] pointed out that ^{94}Zr is the most nearly pure s-process isotope. It is then possible to use ^{94}Zr as reference isotope in order to evaluate, between Zr isotopes, the balance of s- and r-processes. Since the isotopic abundances produced in the neutron capture processes are mostly determined by the neutron capture cross sections of the involved isotopes, a fine determination of the ^{94}Zr(n,γ) cross section becomes mandatory to constraint stellar parameters as neutron density, temperature and metallicity at which nucleosynthesis took place.

5.11.1 Resonance analysis

In total 49 resonances were analysed in the investigated energy range between 0.01 and 60 keV [99]. Among the analysed resonances, 4 resonances were identified for the first time [85,95]. On the other hand, 5 of the resonances reported previously, have not been observed in this measurement [85].

The values obtained by the analyses of the background subtracted capture yield are listed in Table 5.11; examples illustrating the quality of the fits are shown in Fig.5.15.

Due to the decreasing signal/background ratio, the statistical uncertainty grows with neutron energy from ≈ 4% at 2 keV to ≈8% at 60 keV. The present results can be compared with existing measurements [82, 85, 89, 95]. Data from Refs. [82, 89, 95] are largely incomplete; Ref. [85] gives information on resonance parameters, obtained in a measurement performed at the Oak Ridge Electron Linear Accelerator with a pair of non-hydrogenous fluorocarbon liquid scintillators (capture measurement) and a ^{6}Li glass scintillator (transmission measurement).

As in the case of ^{90,92}Zr, the neutron widths are much bigger than the radiative width for all the analysed resonances; then, the present neutron capture measurement is mainly sensitive to the capture width $\Gamma_{\gamma,}$ see § 4.5. A direct comparison of K values, between present results and those of Ref. [85] are very close to the unity, as shown in the upper panel of Fig.5.16.

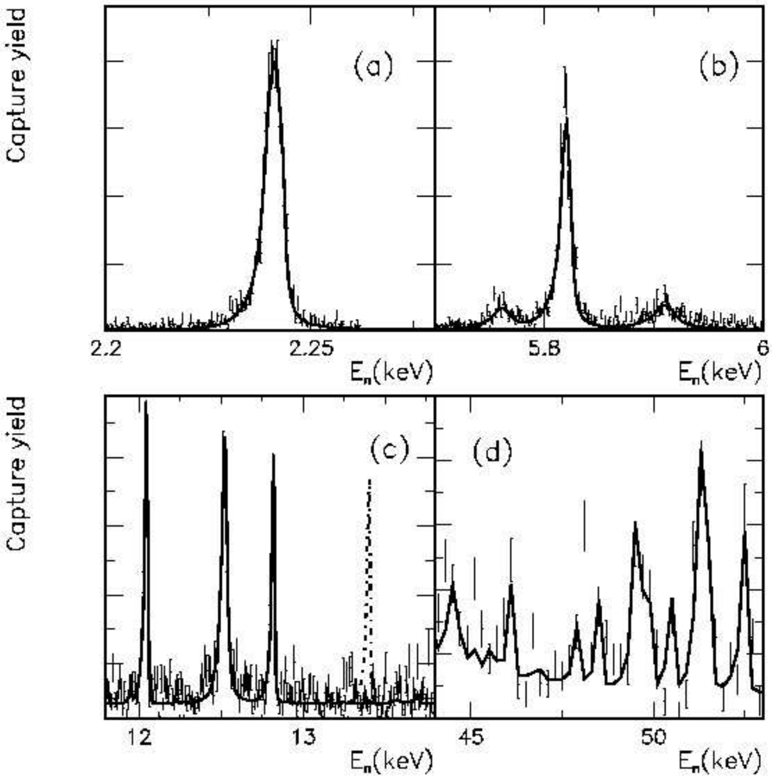

Figure 5.15: ^{94}Zr capture yield as a function of the energy of incident neutrons (E_n). Examples for fits with the R-matrix code SAMMY (solid lines); in the panel (c) a previously reported resonance [85] probably due to a ^{90}Zr contamination) is drawn in a dot-dashed line, using the parameters listed in the JENDL3.3 compilation [88].

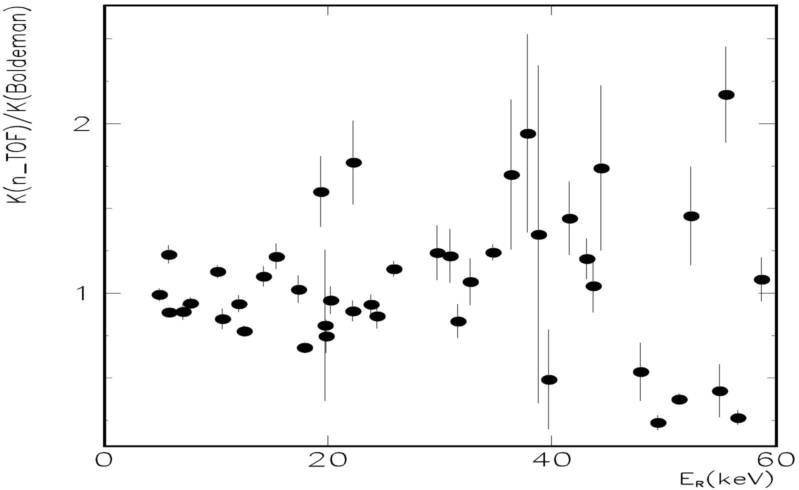

Fig 5.16: Ratio between ^{94}Zr capture kernel values extracted from the present measurement and the results reported in Boldeman et al. [85], versus resonance energy.

TABLE 5.11: Resonance parameters extracted from the fit of the n_TOF ^{94}Zr capture data. Except for the first resonance, the values of Γ_n used in the SAMMY fit were kept fixed to values from Ref. [79, 85,88].

E_r (eV)	J	l	K (meV)	ΔK (%)
2240.54(3)	1/2	0	66.5	1.5
4024.70(4)	1/2	1	126.	3.8
5760.4(6)	1/2	0	54.1	4.4
5817.7(1)	3/2	1	293.	2.2
7071.(1)	1/2	0	66.	5.4
7712.3(3)	3/2	1	160.	3.8
10135.4(3)	3/2	1	203.	3.4
10562.4(6)	1/2	1	48.4	7.2
12037.9(5)	1/2	1	122.	5.3
12515.9(7)			233	4.3
[a]12809.1(8)			(87.5)	(56.)
(x) ≈13390				
14231.7(6)	3/2	1	187.	5.4
15389.(1)	1/2	1	140.	6.2
17372.(1)	1/2	1	132.	7.8
19375(16)	1/2	0	104.	13.
19738.(2)	3/2	1	219.	55.
19855.(2)	1/2	0	59.	13.
20236.(4)	1/2	1	163.	8.4
22203(2)	1/2	1	215.	6.9
22280.(4)	1/2	0	62.	14.
23853.(3)	3/2	1	327.	6.2
24389.(3)	1/2	1	199.	8.5
25858.(4)			286.	4.0
[a]27836.(3)			239.	9.2
[a]28155.(2)			376.	9.9
29755.(9)	1/2	0	114.	13.
30884.(5)	1/2	1	183.	13.
31612.(7)	3/2	1	184	12.
32719.(1)	3/2	1	299.	13
34749(23)	1/2	0	149.	3.8
(x)≈35330				
(x)≈35700				
36386.(3)			306.	26.
37839(28)	3/2	1	272.	30.
38808.(1)			229.	74.
39721.(6)			59.	60.
41563.(9)	3/2	1	404.	15.
43698.(2)			240.	15.
44408.(2)	1/2	0	113.	28.
(x)≈45520				
(x)≈46060				
47919.(2)	3/2	1	129.	32.
48460.(2)	1/2	0	89.	24.
49463(18)			95.	18.
[a]49568.(5)			348.	55.
51352.(4)	1/2	1	90.	8.9

E_r (eV)	J	l	K (meV)	ΔK (%)
52405(14)	1/2	1	90	8.9
54980(19)	1/2	1	102.	37.
55536.(3)	3/2	1	695.	13.
56608.(3)			112.	16.
58733(20)			660.	12.

Uncertainties are given as 2012.89(4)≡2012.89±0.04;
(a) New;
(x) Refers to not observed resonances;

5.12 ^{96}Zr measurement

^{96}Zr is the most neutron rich isotope, it is traditionally considered to be an r-only isotope [91,100] because of the short half-life of ^{95}Zr, 64 days. However, it may be substantially fed by the s-process for $N_n \geq 3 \times 10^8$ neutrons cm^{-3}. Since ^{96}Zr has a low neutron cross section, once it accumulates, it is not easily depleted by neutron captures. In the helium inter-shell of AGB stars, in the ^{13}C pocket, as a result of the low neutron density, ^{96}Zr cannot be created but only depleted and is fed during the small neutron burst by the ^{22}Ne source in the TP. Thus, the s abundance of ^{96}Zr is a strong indicator of the efficiency of the ^{22}Ne neutron source.

Two different measurements with two different samples were made, one at the n_TOF facility and the other at the GELINA facilty.

5.12.1 ^{96}Zr(n,γ) measurement at n_TOF

The sample used at n_TOF is the one reported in Tab 5. 6, where the ^{96}Zr enrichment was 58.3%. As in the case of ^{93}Zr there was a consistent presence of the other Zr isotopes. The energy investigated was between 0.1 – 40 keV, 15 resonances were analysed, one of the resonances reported previously [79], has not been observed in this measurement.

The values obtained by the analyses of the background subtracted capture yield are listed in Table 5.12; examples illustrating the quality of the fits are shown in Fig 5.17.

The neutron widths are much bigger than the radiative width for all the analysed resonances except for the first resonance at 301 eV; then, the present neutron capture measurement is mainly sensitive to the capture width Γ_γ.

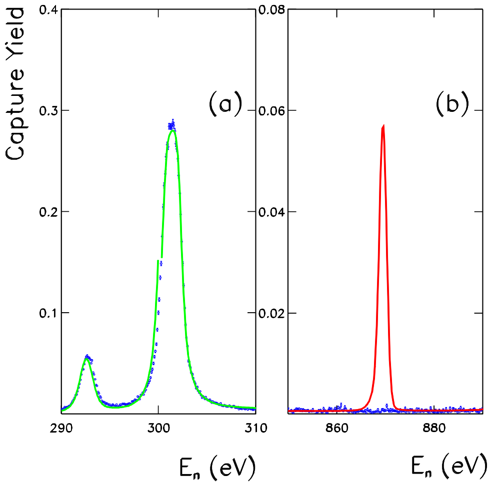

Figure 5.17: ^{96}Zr capture yield as a function of the energy of incident neutrons (E_n). Examples for fits with the R-matrix code SAMMY; in the panel (b) a previously reported resonance [79] that was not observed in this work is drawn (red) using the parameters listed in the JENDL3.3 compilation [88].

Due to the decreasing signal/background ratio, the statistical uncertainty grows with neutron energy from ≈ 4% at 2 keV to ≈6% at 40 keV. The present results can be compared with existing measurements [82, 89, 101, 102]. Fig 5.18 shows the comparison of the kernels measured at n_TOF data with the [79] data compilation, a difference of 25% in average is found.

TABLE 5.12: ^{96}Zr(n,γ) kernels extracted from the fit of the n_TOF capture data.

E_r (eV)	J	l	K (meV)	ΔK (%)
301.28(2)	1/2	1	113.3	0.3
(x) ≈870				
3820.5(1)	1/2	1	34.6	2.8
4135.3(3)	3/2	1	106.5	3.1
5445.5(8)	1/2	0	56.1	3.3
5974.9(2)	3/2	1	181.2	2.2
9009.(1)	1/2	1	47.	5.7
13286.0(7)	3/2	1	78.5	5.4
15150.9(5)	3/2	1	335.8	3.3
15432.(10)	1/2	0	76.7	11.
17790.9(9)	3/2	1	222.7	4.8
24703.(7)	1/2	0	35.4	15.1
29815.(15)	3/2	1	681.	7.1
35186.(17)	1/2	0	144.	21.9
35880.(18)	1/2	1	149.	15.9
36671.(10)	3/2	1	203.	22.5

Uncertainties are given as 301.28(2) ≡ 301.28±0.02;
(x) Refers to not observed resonances;

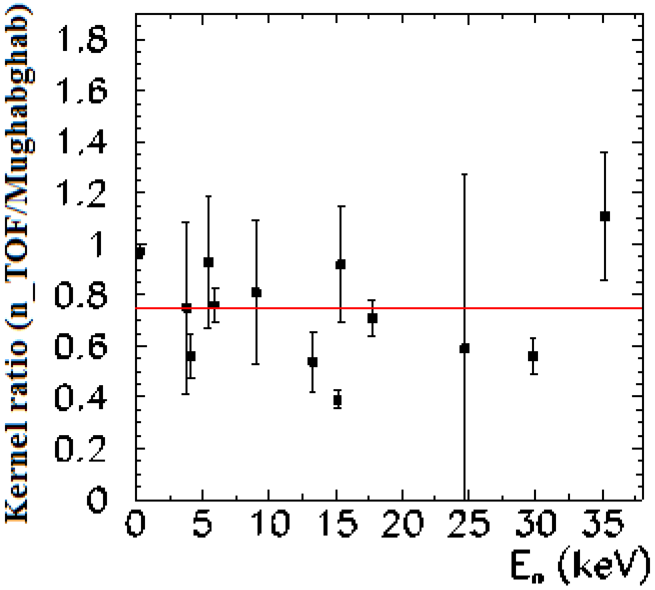

Figure 5.18: Ratio between ^{96}Zr capture kernel values extracted from the present measurement and the results reported in [79], versus resonance energy.

A cross check of the results has been done with the sample used for the ^{93}Zr measurement. The presence of ^{96}Zr in this sample, see Tab

5.6, is almost 20%, the same as for the isotope ^{93}Zr. For this sample only three resonances of ^{96}Zr could be analysed; the comparison between the kernels is reported in Tab 5.13. The agreement between data is better than 6%, Fig 5.19 shows the fits.

TABLE 5.13: Comparison between the ^{96}Zr kernel from Tab 5.12, K_E, and the kernel extracted from the fit of the capture data of the sample used for the ^{93}Zr measurement where the ^{96}Zr enrichment is of 20.5%.

E_r (eV)	K_E (meV)	K (meV)	ΔK (%)
301	113.3	107.1	5.5
3820	34.6	35.2	1.7
4135	106.5	104.2	2.2

The good agreement between the two sets of data gives a good confidence on the validity of the results of the ^{96}Zr analysis.

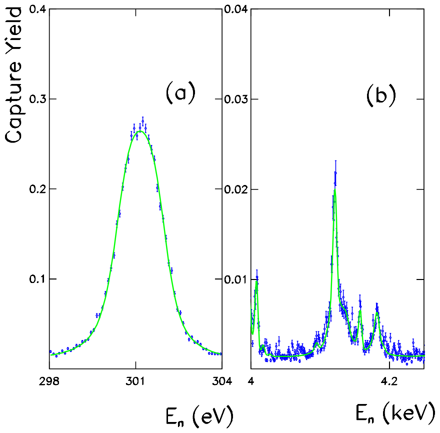

Figure 5.19: Fits with the R-matrix code SAMMY for the resonances of the ^{96}Zr(n,γ)^{97}Zr reaction measured with sample used in measurement reported in § 5.7

5.12.2 ^{96}Zr measurements at GELINA facility

The big discrepancy between the n_TOF data and the previous experiments and the lack of a reliably set of transmission data in the nuclear databases were the motivations for a new measurement of ^{96}Zr at the GELINA facility.

The sample used for this measurement was highly enriched in ^{96}Zr and the characteristics are reported in Tab 5.14

The oxide powder was pressed to a pellet 50 mm in diameter and encapsulated in an aluminum can 0.2 mm thick.

Unfortunately the distribution of the oxide powder in the can was not uniform. An X-ray scan of the sample was done after the measurement; as can be seen in Fig 5.20 the can is only partially filled. The uniformity of the sample is a prerequisite of a measurement with high accuracy, (1) for the relation between sample thickness and the cross section (see Eq. 4.32 and 4.33). (2) for the normalization of the yield, being the geometry and size of the sample not well defined.

Despite the not uniformity of the sample it was interesting to check if the discrepancies found between the n_TOF data and the database were confirmed by the measurement at the GELINA facility.

The normalization was obtained fixing the resonance parameters of the first resonance, 301 eV, to the one found in the n_TOF measurement. This choice is justified by:

a) The first resonance of the ^{96}Zr capture reaction is well studied, [100,91]

b) Of course to normalize at the first resonance of n_TOF data does not make an absolute normalization but it should allow, in any case, to clarify if the large difference found in the n_TOF kernels is real or due to some not well understood problem in the facility or on the sample used at n_TOF.

Table 5.15 reports the comparison of the kernels obtained from the fit of some resonances of the capture data of the GELINA measurements, with the ones reported in Table 5.12. The agreement between the data is better than 10%. This is remarkable considering the limit of this measurement due to the sample. The check was stopped at 25 keV because above such energy the uncertainty associated at the kernels was too high.

Table 5.14: GELINA sample characteristics

Sample	Chemical form	Isotopic composition (%)						Thickness
		^{90}Zr	^{91}Zr	^{92}Zr	^{93}Zr	^{94}Zr	^{96}Zr	(atoms/b)
^{96}Zr	ZrO_2	1.54	0.40	0.73	0.00	1.70	95.63	0.00161

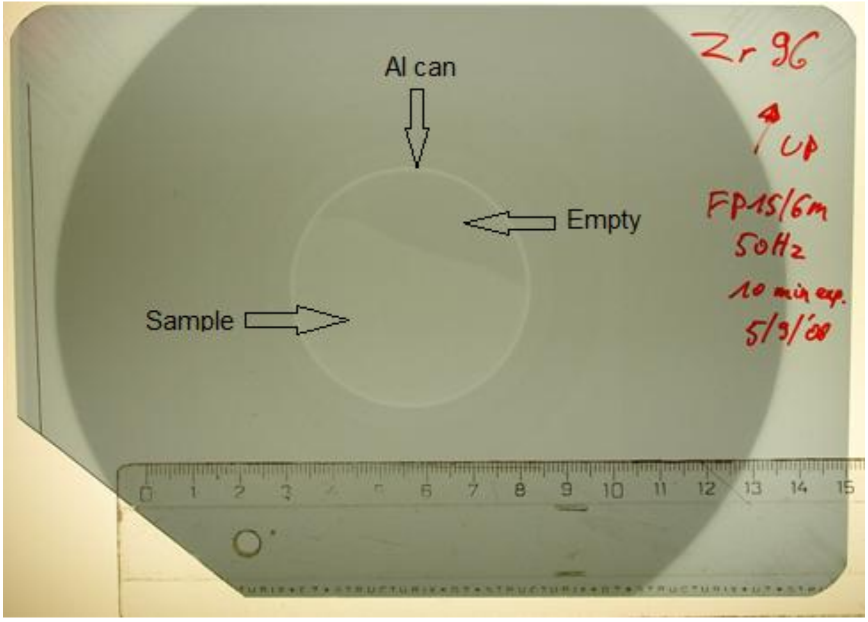

Figura 5.20 X-ray scan of the ^{96}Zr sample used in the GELINA.

Fig. 5.21 shows the fit of the first resonance, panel (a), also in the GELINA data the resonances at 870 eV is not observed, panel (b).

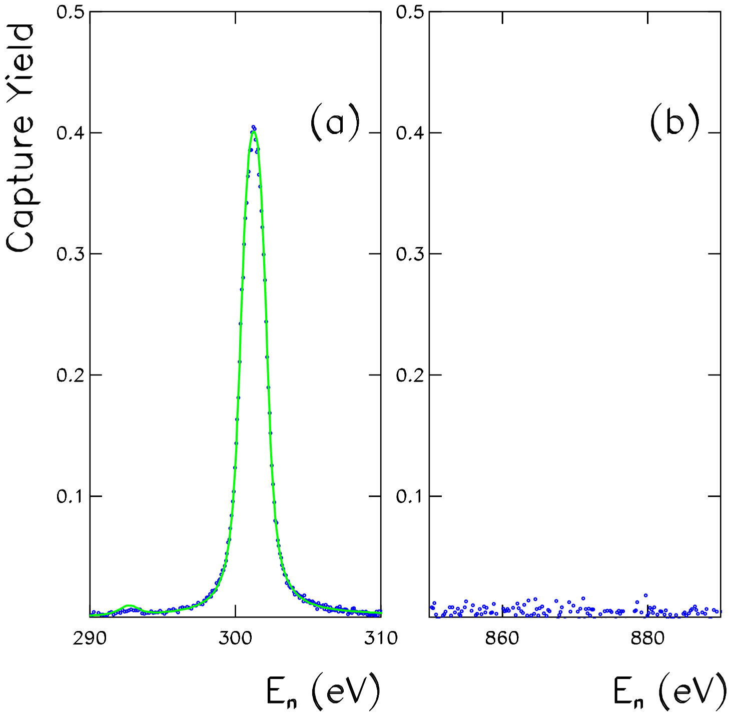

Figure 5.21: Examples of fits of the enriched sample of ^{96}Zr.In the panel (a) is reported the first resonance which was use to calculate the normalization. Panel (b) shows that also in the GELINA measurement the resonance at 800 eV was not observed.

TABLE 5.15: Comparison between the kernels from Tab 5.12, K_{n_TOF}, and the kernels extracted from capture data of ^{96}Zr measurement at the GELINA facility K_{GEL}

E_r (eV)	K_{GEL} (meV)	K_{n_TOF} (meV)	ΔK (%)
301	113.	113.	0.0
3820	32.3	34.6	7.1
4135	111.	107.	4.4
5445	54.3	58.1	6.9
9009	48.3	47.	2.7
13286	71.5	78.6	9.9
15150	33.2	33.6	1.3
15432	78.3	76.7	2.1
17791	21.6	22.3	2.9
24703	38.3	35.4	7.7

5.13 Resonance analysis summary

In all the Zr measurements the kernels extracted show substantial differences with previous measurements, most of them performed at the ORELA facility. Table 5.16 resumes the weighted average ratio between the kernels obtained at the n_TOF facility and the previous measurements performed at ORELA facility.

Table 5.16 Weighted average ratio between the kernels measured at n_TOF and the ones of the previous measurements performed at ORELA facility.

Sample	$<K_{n\_TOF}/K_{ORELA}>$
^{90}Zr	0.84±0.01
^{91}Zr	0.91±0.01
^{92}Zr	0.86±0.02
^{93}Zr	0.66±0.01
^{94}Zr	1.03±0.01
^{96}Zr	0.73±0.02

These systematic differences are due to smaller corrections (e.g. for self shielding and multiple scattering), lower backgrounds, modern data acquisition techniques with fast digitizers, which allowed to analyse the data off-line in the most flexible way, including an efficient pulse shape analysis for n/γ discrimination, and the use of a well tested and improved R-matrix code. All together these improvements can account for less than 5%, the largest contribution to these differences is related to the very low neutron sensitivity of the n_TOF setup.

The sensitivity to scattered neutrons plays an important role for all resonances with a neutron width that is much larger than the radiation width. This is the case of all Zr isotopes except ^{93}Zr. The influences of the neutron sensitivity on the resonance parameters have been illustrated by Corvi in [103] where he compared the average radiation widths for s- and p-wave resonance for structural materials as ^{55,56}Fe, obtained at GELINA with C_6D_6 detectors with those obtained at ORELA where instead C_6F_6 detectors were used (as in the case of the Zr measurements performed at ORELA). The discrepancy found for the p-wave resonances was around 20% while for large s-wave resonances the radiation widths obtained at ORELA were up to a factor 2 larger than those determined at GELINA. The influence of the neutron sensitivity on the determination of the width is shown in Fig. 5.22 for all even Zr isotopes measured, the ratio of the radiation widths reported by [84] ^{90}Zr, [85] ^{92,94}Zr and [102] ^{96}Zr measured at ORELA facility and the ones obtained at n_TOF is plotted in function of the scattering-to-capture ratio Γ_n/Γ_γ measured at n_TOF. The ratio between the experimental radiation widths increases linearly with the Γ_n/Γ_γ ratio for all isotopes except for the ^{94}Zr, it gives a good indication that the systematic differences reported in Table 5.16 are mostly due the difference in neutron sensitivity of the detection.

In the case of ^{93}Zr there is also the contribution of a better discrimination between the signal and radioactivity of the sample.

There is also some difference in the number of resonances observed between the n_TOF measurements and the previous ones. In Table 5.17 the number of new and not observed resonances are listed for each isotopes.

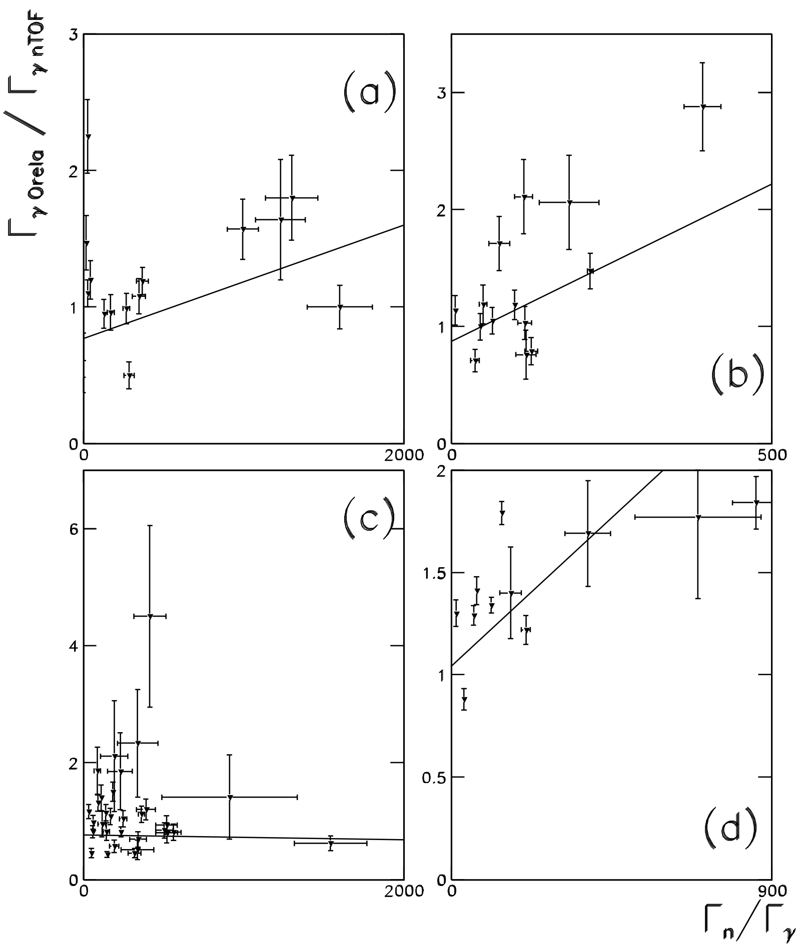

Figure 5.22 Influence of the neutron sensitivity on the (a) ^{90}Zr, (b) ^{92}Zr, (c) ^{94}Zr, (d) ^{96}Zr capture cross sections. The tendency line is obtained from a weighted last-square fit of the data.

Table 5.17 List of new and not observed resonances in the n_TOF measurements

Isotope	New resonances	Not observed
^{90}Zr	11	0
^{91}Zr	33	0
^{92}Zr	3	0
^{93}Zr	3	4
^{94}Zr	4	5
^{96}Zr	0	1

Unfortunately there is a lack of information on the previous capture measurements, as details on the samples used in the measurements, and especially these stored neutron capture data are not in the experimental nuclear reaction database EXFOR [104].

So it is difficult to check if the differences are due to the apparatus resolution or to a lower background. Of course cases as the ones reported in Fig 5.3, 5.6, 5.15c, 5.17 cannot be attributed to the background or to the apparatus resolution but most probably to some inadvertence or problem on the sample. In the case of ^{94}Zr a check on the transmission data, available in the EXFOR database and relative to the experiment reported in [85], was made in order to check if the new observed resonances were also present in that data. Fig 5.23 reports a fit made with the SAMMY code.

As can be seen from Fig. 5.23(a) the resonances at 27.8 and 28.2 keV, were already present in the transmission data but they were not reported in the paper and in any other evaluated libraries as JENDL and ENDF [88, 105]. These resonances cannot be attributed to some other Zr isotopes or impurities present in the sample.

On the contrary in Fig. 5.23(b) two resonances are shown reported in [85] and in ENDF and JENDL library but not observed in the analysis of n_TOF data.

The most visible case is ^{91}Zr, where 30 new resonances were found, most of the new resonances, 20, are in the energy region between 20 and 26 keV where no experimental data were available before the n_TOF data were obtained.

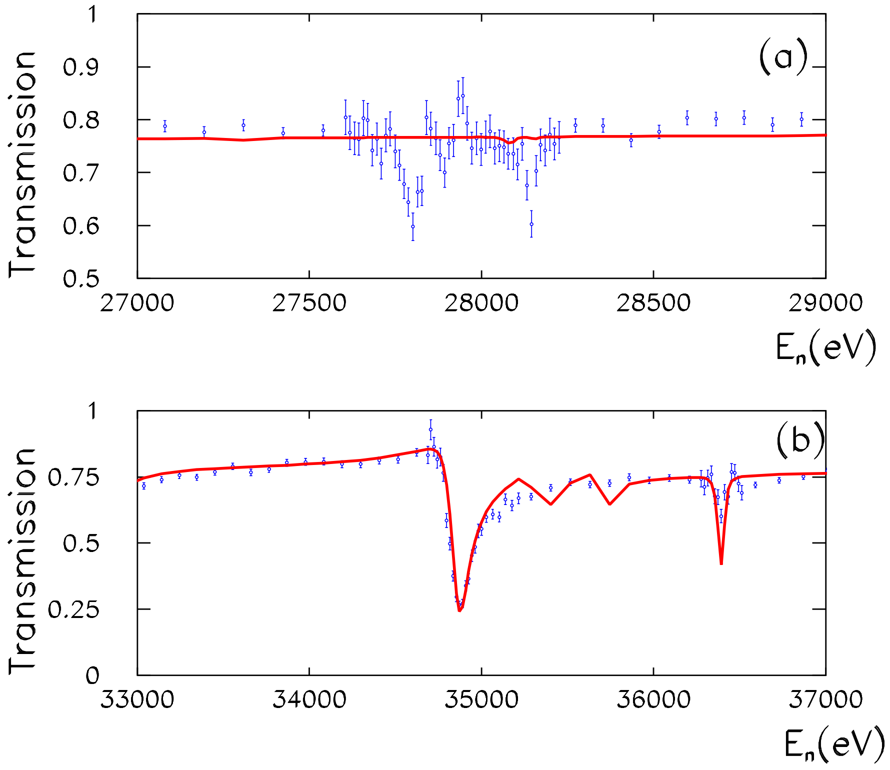

Figure 5.23 Two examples of ^{94}Zr transmission data extracted from the EXFOR data library relative to the ^{94}Zr measurement reported in [85], in blue the data, in red the fit obtained using the resonance parameters reported in [85]. (a) Two resonances observed in the n_TOF measurement and not reported in Boldeman et al.[85] and in the JENDL and ENDF libraries[88].(b) Two resonances reported in Boldeman et al [85] and in the evaluated libraries but not observed in the n_TOF data.

Chapter VI Astrophysical implications

6.1 Introduction

In this chapter calculations of the Maxwellian-averaged cross sections and the astrophysical implications of the results are reported.

6.2 Maxwellian Averaged Cross sections

The MACS at typical s-process temperatures are obtained by folding the capture cross section with the thermal stellar neutron spectra over a sufficiently wide neutron energy range. Typical thermal energies are kT = 8 and 23 keV in low mass stars, and 26 to 90 keV in massive stars, respectively. Therefore, the energy dependent capture cross sections are needed between 100 eV and about 500 keV to account for the highest temperatures reached during carbon shell burning in massive stars. Although this fact restricts the energy range where the capture cross section has to be known, it nevertheless implies that experimental data of the Zr isotopes presented in this work have to be complemented for the neutron energy range above the one that was possible to measure at n_TOF.

As seen in the previous chapter the n_TOF data ranged in energy from 10 eV, as lower limit, to a few tenths of keV (depending on the isotopes). It was reasonable to extend this limit to the thermal energy E_n = 0.0253 eV, since the measured thermal capture cross sections are given for many nuclei [79]. As mentioned in § 4.6 all the Zr isotopes measured in this thesis do not have resonances in the thermal neutron region, so the Westcott g-factor is with good approximation equal to unity for all Zr isotopes under investigation [78]. The resonance analysis was made for all isotopes starting from 10 eV and the lowest resonance found is the 110 eV resonance of ^{93}Zr. In the following part of the chapter only the energy upper limit of the data analysis will be mentioned, omitting the lower one that is 10 eV for all isotopes.

The high energy part of the data was complemented using the evaluated data of the JENDL 3.3 library [88, 90, 105]. This choice was made because the JENDL library provides also the calculated MACS at different stellar temperatures for all isotopes. In the case of the Zr isotopes these MACS were easily reproduced when using the SAMMY code to calculate the MACS with the evaluated data of the library, giving a direct way to compare the goodness of MACS calculations of the n_TOF data.

The MACS were calculated using the code SAMMY using resonance parameters fitted from our measurements, in which were included the thermal capture cross section, complemented by resonance parameters and capture cross sections in the URR from the JENDL library in the remaining energy region. In SAMMY the numerical integration technique is used to evaluate the Eq. 4.45. The capture cross sections are generated from the resonance parameters, the values of the URR are added directly to resonance cross section before the integration.

Concerning the definition of uncertainties associated to the MACS an uncertainty of 10% was considered for the contribution given by the evaluations.

In some cases, the MACS deduced from experimental data have to be corrected by the so-called stellar enhancement factor, which accounts for the possibility that neutron capture may also occur in thermally populated excited states. However, this correction is negligible for all Zr isotopes [6].

6.2.1 ^{90}Zr MACSs

As reported in § 5.6 the neutron energy range investigated for ^{90}Zr at n_TOF was between 0.01 – 70 keV.

For the resonance dominated cross section it is obvious that the MACS is strongly dependent on the energy and strength of the most prominent resonances. To illustrate this effect, the impact of the strongest resonances for thermal energies of kT = 5 and 30 keV (Table 6.1) of ^{90}Zr was evaluated. Already the first four resonances account for more than 84% of the MACS at kT = 5, whereas the five most important resonances contribute only 45% at kT = 30 keV.

Table 6.1: Relative contribution of strong resonances[a] (in %) to the MACS at thermal energies of kT = 5 and 30 keV.

	kT = 5 keV		kT = 30 keV	
E_r(keV)	JENDL3.3[88]	This work	JENDL3.3[88]	This work
3.855	12.8	15.1		
4.005	25.4	24.8		
7.251	31.1	28.5	8.2	7.6
8.852	15.0	15.2	5.1	5.3
19.685			5.0	4.7
26530			5.7	5.7
41.340			21.1	16.7

[a] Only resonances with relative contribution ≥ 4% are considered

The comparison in Fig.5.4 shows that the kernels obtained in the present analysis are on average ≈ 10% smaller than those of Ref. [79].

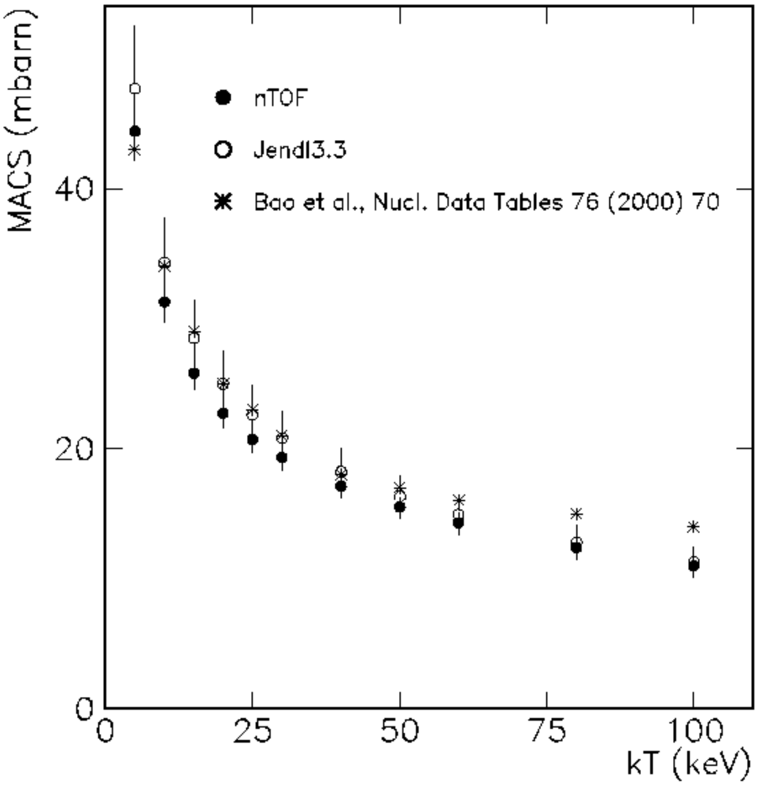

Figure 6.1: Comparison of MACSs calculated with present experimental results complemented by data from JENDL/3.3 [88] above 70 keV (full circles) and thermal capture cross sections [79] with values obtained exclusively with data from Ref.[85] (open circles) and with the compilation of Ref.[6] (asterisks).

Consequently, the MACS calculated with the present experimental data are up to 10% lower than those obtained with previous data as shown in Table 6.2 and Fig.6.1. Another important improvement result of n_TOF measurement is the reduction of uncertainties by more than a factor of two.

Table 6.2: Comparison of MACS (in mbarn) listed in the compilation of Ref. [6] with evaluated data from JENDL/3.3 [88] and this work.

kT	Maxwellian averaged cross sections (mbarn)		
(keV)	Ref. [6]	JENDL3.3 [88]	This work
5	43	47.7±4.8	44.2±2.2
10	34	34.±3.4	31.3±1.5
15	29	28.5±2.9	25.8±1.2
20	25	25.0±2.5	22.7±1.1
25	23	22.6±2.3	20.7±1.0
30	21±2	20.8±2.1	19.3±0.9
40	18	18.2±1.8	17.1±0.8
50	17	16.3±1.6	15.5±0.8
60	16	14.9±1.5	14.3±0.7
80	15	12.8±1.3	12.4±0.6
100	14	11.3±1.1	11.0±0.5

6.2.2 ^{91}Zr MACSs

The present measurement is limited to energies below 26 keV, see § 5.7. After complementing n_TOF data with the library JENDL3.3, overall uncertainties of 5 to 6% below 30 keV thermal energy were obtained. This corresponds to an improvement by a factor two compared to previous values in the temperature range of low mass AGB stars, where most of the Zr is produced.

The present MACS for kT = 30 keV is compared in Table 6.3 with the rather discrepant and uncertain previous values. The recommended

MACS of 60 ± 8 mbarn given in the compilation of Ref. [6] is based on the experiment by Musgrove et al. [80, 106]. The value of the MACS at the temperature of 30 keV for neutron energies below 26 is 36.1± 2 mbarn using n_TOF data, and 35.9 mbarn using the data from JENDL3.3 based on Musgrove measurement. Even though the present capture kernels are 10% smaller, the present MACS is very close to the previous recommendation, because of the new resonances found. The significantly better accuracy of the present measurement is of crucial importance, because the s abundances are inversely proportional to the stellar cross sections.

Table 6.3: Comparison of MACS values at kT = 30 keV thermal energy. Errors are associated only to experimental values.

MACS (mbarn)	Reference	Year
59±10	[62]	1967
68±8	[107]	1971
128	[108]	1976
53±10	[81]	1977
(a) 60±8	[106]	1978
66	[109]	1981
135	[110]	2000
48.4	[111]	2002
53.7	[112]	2005
63±4	This Work	

(a) Recommended value in Ref. [7].

The present MACSs (listed in Table 6.4) and the values of Bao et al. [6], which are based on Musgrove et al. [80, 106], are compared in Fig. 6.2. Uncertainties associated at the present MACS increase with thermal energy and the differences between the two data sets are smaller at higher values of kT due to the fact that the present experimental values have been complemented for the neutron energy range above 26 keV by the JENDL-3.3 evaluation [88].

Table 6.4: MACS calculated with the present experimental data at different thermal energies. Above 26 keV data are complemented by JENDL/3.3 evaluations [88].

kT (keV)	MACS (mbarn)
5	237±12
10	144±8
15	106±6
20	86±5
25	72±5
30	63±4
40	51±4
50	44±4
60	38±3
80	33±3
100	28±3

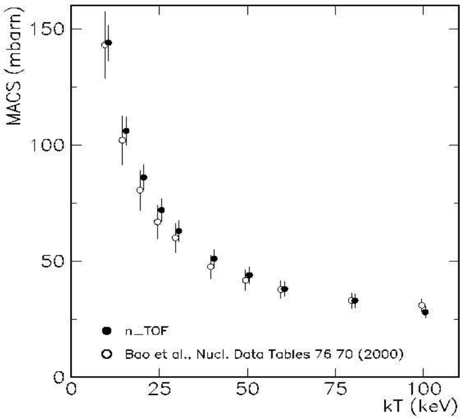

Figure 6.2: Comparison of present MACSs (full circles) with values from the compilation of Ref. [6] (open circles). To avoid the overlap of error bars, values were displaced along the abscissa axis: +0.5 keV (this work), -0.5 keV (Ref. [6]).

6.2.3 ^{92}Zr MACSs

For the resonance dominated cross section of ^{92}Zr the MACS is strongly dependent on the energy and strength of the most prominent resonances. This is illustrated in Fig. 6.3, where the relative resonance contributions are plotted for the characteristic thermal energies. The results of the present measurement cover the energy range up to 40 keV, which contributes 98%, 73%, and 64% of the MACS at 8, 23, and 30 keV, respectively.

The comparison in Table 6.5 shows that the present capture kernels are 20% smaller on average than those reported in Ref.[85] (the relative contributions of these resonances illustrate their importance for the MACS at low thermal energies). This is most probably due to the much lower neutron sensitivity of the n_TOF experimental setup relative to the ones used in previous measurements [85, 95].

The large improvement in the neutron sensitivity is particularly evident in the case of the 6.8 keV resonance, which is characterized by one of the largest Γ_n/Γ_γ ratios (Fig.5.9 (b)). In this important case the present capture kernel is almost a factor of three smaller than reported in Ref. [85].

The impact of the present results is further illustrated in Table 6.6, where the MACS values are compared with those of Nakagawa et al. [88] (which are based on Ref. [85]), for different temperatures and for different upper energy limits, i.e. considering only the contribution of prominent resonances below 7 keV, the resonances below 40 keV investigated in this work, and by using all resonances in the entire

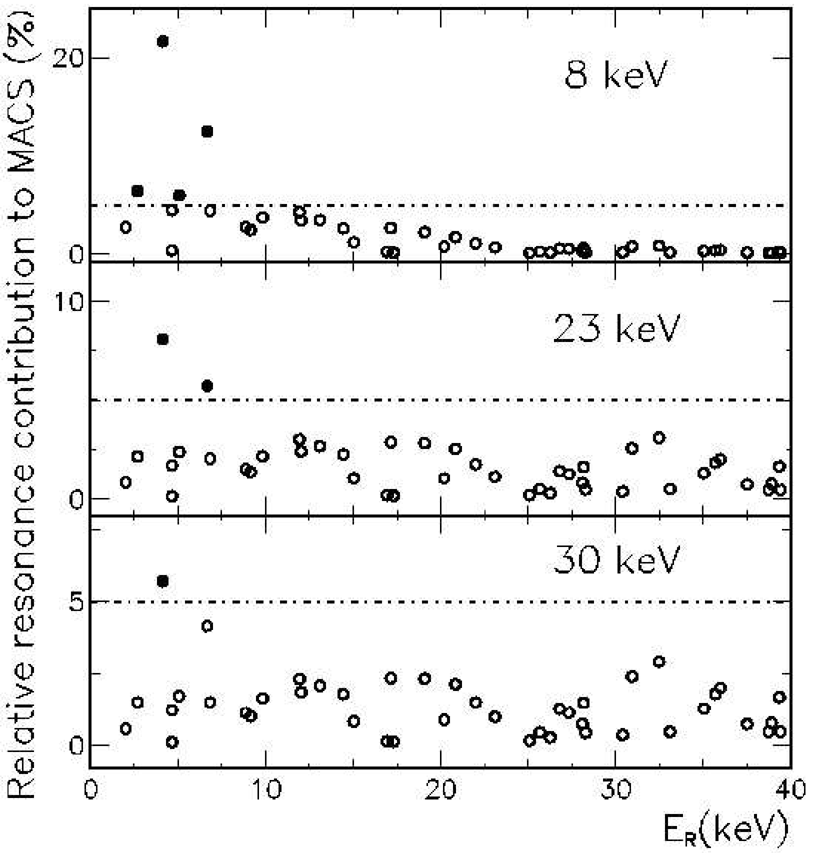

Figure 6.3: Relative resonance contributions for the MACS at characteristic thermal energies. Resonances which contribute more than 5% to the MACS are indicated by full circles.

relevant energy range including the information above 40 keV from evaluated data [88]. The respective contributions to the MACS at the relevant values of kT confirm that the results of this work represent an essential part of the MACS at the stellar environments characterized by kT =8 and 23 keV.

The contributions calculated with the present data are 20 to 25% lower than the MACS obtained with the evaluated data from the JENDL library [88]. Therefore, the evaluated data [88], which were used above 40 keV to complement the present results, have been scaled by a factor of 0.8. Concerning the definition of errors associated with the MACS an uncertainty of 10% was considered for the contribution given by the evaluation.

TABLE 6.5: Capture kernels of the most prominent resonances and their relative contribution to the MACS.

Er	Kernel (eV)		Rel. contribution (%)		
(keV)	This work	Boldeman[85]	kT = 8 keV	23 keV	30 keV
2.7	0.115	0.171	6.5	2.0	1.5
4.1	0.460	0.57	21.7	8.1	5.7
5.0	0.142	0.159	6.0	2.4	1.7
6.6	0.363	0.49	12.5	5.7	4.1
6.8	0.132	0.37	4.4	2.1	1.5

TABLE 6.6: Maxwellian averaged cross sections (in mbarn) calculated for different thermal energies and upper integration limits, compared with the ones extracted from the data in Ref. [88].

Contribution to MACS		kT = 8 keV	23 keV	30 keV
En ≤ 7 keV	JENDL[88]	74±8	14±1.5	9.3±0.9
	[This work]	58±3	12±0.6	7.5±0.4
En ≤ 40 keV	JENDL[88]	115±11	39±4.	28±3
	[This work]	95±5	33±1.6	24±1.2
Full range	Bao[6]	-	-	33±4
	JENDL[88]	117±12	52±5	46±5
	[This work]	97±5	44±3	38±3

The MACS derived from the experimental data of Ref. [85] are somewhat confusing. Although the JENDL evaluation [88] was obtained from these results, the MACS values in Table 6.5 are clearly discrepant [113]. Moreover, the same experimental data [85] were used in another publication of the same authors [106], where the MACS at 30 keV was stated to be 51 instead of 34 mbarn in [85], and both values were subsequently scaled by a common correction factor [114] to 50 and 33 mbarn, respectively.

The final MACSs are compared with previous data in Fig. 6.4. In this figure the full and dashed lines represent evaluations based on the data from Ref. [85]; the full line represents the MACS calculated on the basis of the evaluated data in the JENDL library [88, 113], the dashed line refers to the MACS compilation of Bao et al. [6].

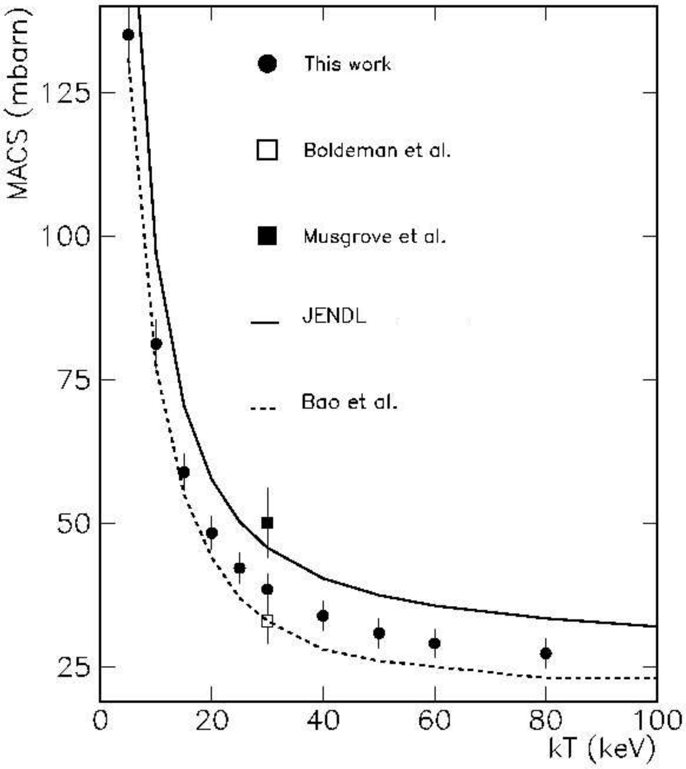

Figure 6.4: Comparison of present ^{92}Zr MACS (full circles) with values from Refs. [6, 85, 88, 106].

The present data agree with Ref.[6] (and disagree with Ref.[88]) at low temperatures; however it must be noted that the agreement with Ref.[6] progressively vanishes toward higher temperatures. In this context, it has to be reminded that the uncertainties of the present results are partly related to the assumption used for the extrapolation above 40 keV. The weight of the extrapolation, and consequently the uncertainty in the MACS, increases with increasing temperature, reaching approximately 10% at kT = 80 keV. A reduction of the overall uncertainty for high temperatures could (eventually) be achieved by new, accurate measurements at energies above 40 keV. A new measurement of the ^{92}Zr has been approved at the GELINA facility for the year 2011 in the framework of EFNUDAT. The measurements will be performed on three ^{92}Zr samples, different in thickness, in order to have a complete set of measurements as capture, transmission and self indication.

6.2.4 ^{93}Zr MACSs

The present measurement is limited to energies below 8 keV, therefore the calculation of the MACS is strongly dependent on the evaluated data used to complement the present data. In Tab. 6.7 a comparison is reported between the MACSs extracted from the present data and those evaluated by the JENDL library for the limited range of the measurement, $E_n < 8$keV.

TABLE 6.7: Maxwellian averaged cross sections (in mbarn) calculated for different thermal energies and with an upper integration limit of 8 keV, compared with the ones extracted from the corresponding data in Ref. [88].

Contribution to MACS		kT = 8 keV	23 keV	30 keV
$E_n \leq 8$ keV	Ref. [88]	142±14	25±2.5	16.0±1.6
	[This work]	95.6±4	17±0.8	10.6±0.6

The contributions calculated with the present data are 30 to 35% lower than the MACS obtained with the corresponding evaluated data.

Since the present data are limited to energies below 8 keV, they have to be complemented with evaluated data, which hence will deliver the main contribution to the calculated MACS. In view of the large discrepancy shown in Tab 6.7, the MACSs were calculated for two extreme cases. In the first case the evaluated data used to complement the data above 8 keV were not scaled, while in the second case they were scaled with a factor 0.65. Fig 6.5 shows the comparison of the present MACSs with the values from Bao [6], the data from the present work are shown as a band representing both cases used to calculate the MACS. In Tab. 6.8 the MACSs calculated for the two cases are reported together with the reference data given in the compilation of Ref. [6].

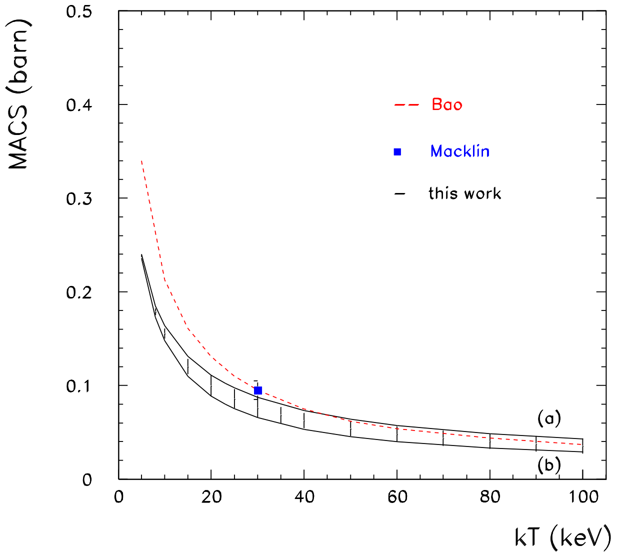

Figure 6.5: Comparison of present ^{93}Zr MACSs (solid lines), with values from Ref. [6] (dashed line) and the experimental data from Ref. [97]. (a) MACSs calculated complementing the n_TOF data with evaluated data [88] not scaled, (b) the complementing data are scaled with a factor 0.65.

The recommended MACS at 30 keV of 95 ± 10 mbarn given in the compilation of Ref. [6] is based on the experiment by Macklin et al. [97]. The difference found is of the order 35% and can be due to a wrong estimation of the radioactive background, to the neutron sensitivity of the γ detectors and, as underlined in § 5.7, from a wrong subtraction in the Macklin measurement of the "background" due to the presence of the other Zr isotopes in the sample.

Table 6.8:Comparison of MACS (in mbarn) listed in the compilation of Ref. [6] and this work calculated for the two different option,(a) complementing data not scaled,(b) complementing data scaled on factor 0.65.

kT	Maxwellian averaged cross sections (mbarn)		
(keV)	Ref.[7]	This work (a)	This work (b)
5	340	240±11	235±11
10	213	164±10.	148±8.9
15	161	130±9.2	110±7.5
20	131	111±8.7	88.4±6.8
25	110	96.9±8.3	74.7±6.5
30	95±10	86.7±7.8	65.1±5.7
40	75	72.6±7.3	52.6±5.3
50	62	63.3±6.3	44.8±4.5
60	54	56.6±5.7	39.5±4.0
80	44	47.9±4.8	32.8±3.3
100	37	42.3±4.2	28.6±2.9

The new values of this work, when the evaluated data are scaled by a factor 0.65, are in good agreement with theoretical values of MOST [111, 112]. In the following only the option (b) of table 6.8

will be considered, this choice is justified by the astrophysical implication of the results, as will be seen in § 6.3.

6.2.5 ^{94}Zr MACSs

For the resonance dominated cross section of ^{94}Zr the two resonances at 5.8 and 17.9 keV contribute to 30% and 14% of the total MACSs at thermal energies of 8 and 30 keV, respectively. Even though on average the capture kernels measured in the present work and those listed in Ref. [85] agree, important differences appear for those specific cases (see Table 6.9).

Table 6.9: Capture kernel of the most prominent resonances

E_R (keV)	K (meV) Ref. [93]	K (meV) This work
5.8	330.±30.	293.±6.
17.9	610.±60.	415.±20.

Given that data of the present work extend only up to neutron energies of 60 keV, for the calculation of the MACSs the energy range needs to be complemented. As illustrated in Fig. 6.6(a) the contribution of the complementary part is negligible at low values of the thermal energies, increases with energy and at 30 keV accounts already for 30% of the total MACS. On this basis we preliminary compared the MACS extracted from the present data and those evaluated by the JENDL library [88], limiting to the energy range up to 60 keV. The interplay of different resonances makes the ratio between MACSs extracted (present work) and evaluated [88, 90, 93] not constant at different values of kT. Concerning the definition of errors associated with the evaluated MACSs an uncertainty of 10% was considered. At low thermal energies the effect of resonances at low neutron energy is dominant, while the weight of single resonances is strongly reduced at higher kT (Fig.6.6 (b)).

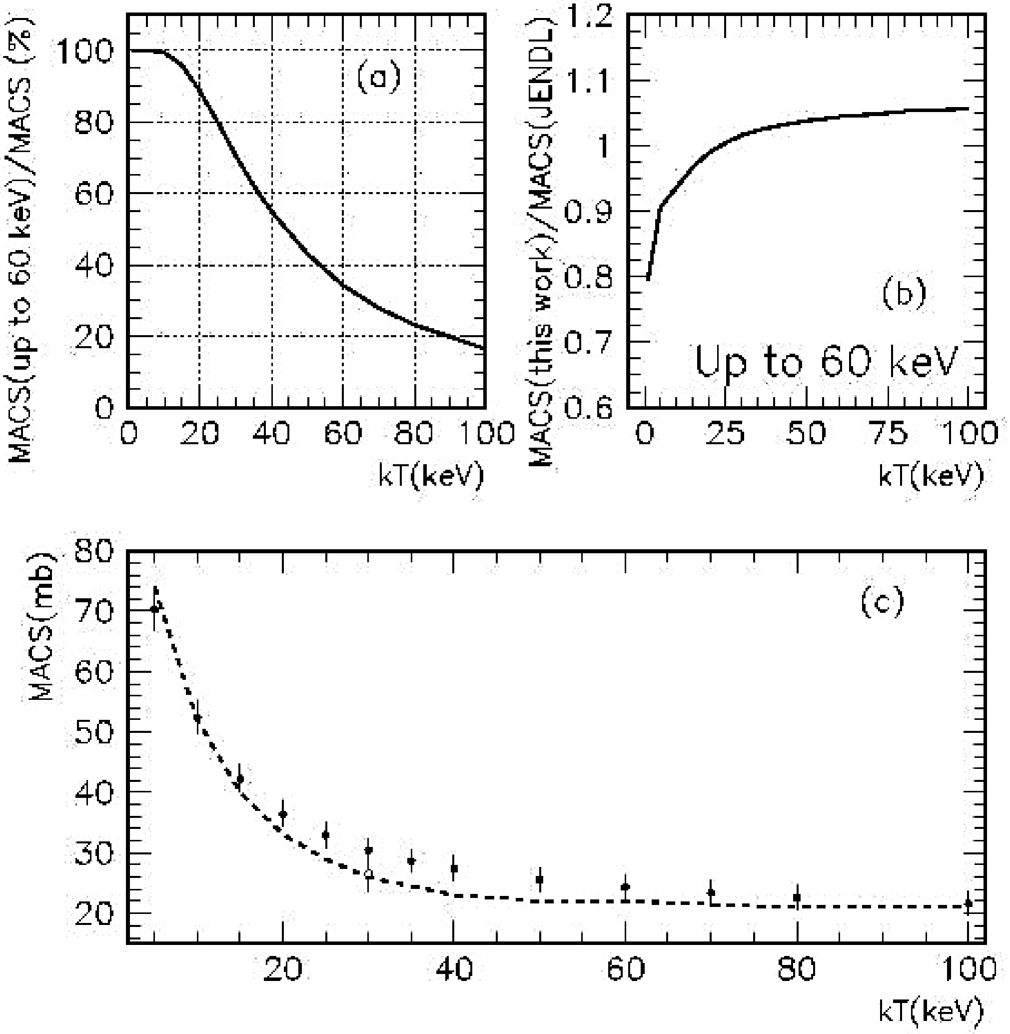

Figure 6.6 ^{94}Zr (a) Relative contribution to MACS as a function of the upper integration limit; (b) Ratio between MACS extracted from the present work and those evaluated in the JENDL library [88], limiting the calculation to the energy range [0, 60] keV, as a function of thermal energy; (c) MACS extracted in present work, complemented above 60 keV by means of JENDL evaluations (full points), as a function of thermal energy. The values at 30 keV extracted in Ref. [85] (open point) and those given by the compilation of Ref. [6] (dashed line) are also reported.

In this context, MACSs extracted from the present data analysis differ significantly at kT values lower than 10 keV, including the case at 8 keV, relevant for the stellar environments in thermally pulsing low mass AGB stars [21].

The MACSs extracted in the present work are lower than those presented by evaluators [88] and by the compilation of Ref. [6] at low values of thermal energies, kT ≤ 10 keV; on the contrary, a general agreement was found with the JENDL evaluation even at larger kT.

Table 6.10:Comparison of MACSs (in mbarn) calculated from this work for different thermal energies and integration limits with the ones extracted from Ref. [6, 88].

kT (keV)	This work $E_n \leq 60$ keV	JENDL[88] $E_n \leq 60$ keV	This work	JENDL[88]	Bao[6]
5	70±3.5	77.5	70.3±3.5	77.5	74.
8	58.5±2.9	63.3	58.5±2.9	63.3	
10	52.0±2.6	55.6	52.3±2.6	55.9	52.
15	40.4±2.0	41.7	42.3±2.2	43.5	40.
20	32.2±1.6	32.6	36.5±2.0	36.7	33.
23	28.4±1.4	28.4	34.0±2.0	34.0	
25	26.2±1.3	26.0	32.9±2.0	32.6	29.
30	21.6±1.1	21.2	30.5±2.0	32.6	26.
40	15.2±0.8	14.8	27.4±2.0	26.8	23
50	11.1±0.6	10.8	25.5±2.0	25.0	22.
60	8.6±0.4	8.2	24.3±2.0	23.8	22.
80	5.4±0.3	5.2	22.6±2.0	22.3	21.
100	3.7±0.2	3.5	21.6±2.0	21.4	21.

For these cases we have to remind that the contribution of the extrapolation above 60 keV of the present data plays a role which importance increases with kT (but a general agreement persists between MACSs calculated limiting the integration to 60 keV). In

Table 6.10 MACS calculated for different thermal energies and upper integration limits are compared with the ones extracted from the data in Refs. [6, 88]

Fig 6.6(c) shows the comparison between the MACSs calculated in the present work and Ref [85, 88].

6.2.6 ^{96}Zr MACSs

The results of the present measurement cover the energy range up to 40 keV, which contributes 100%, 85%, and 75% of the MACS at 8, 23, and 30 keV, respectively.

Tab. 6.11 reports a comparison between the MACSs extracted from the present data and those evaluated by the JENDL library for the limited range of the measurement, $E_n < 40$keV.

TABLE 6.11: Maxwellian averaged cross sections (in mbarn) calculated for different thermal energies and upper integration limit of 40 keV, compared with the ones extracted from the data in Ref. [88].

Contribution to MACS		kT = 8 keV	23 keV	30 keV
$E_n \leq 40$ keV	JENDL[88]	43±4	13.3±1	9.2±1.
	[This work]	32.4±1	9.6±0.5	6.6±0.3

The comparison in Table 6.11 shows that the present capture kernels are 25% smaller on average than those reported in Ref. [88]. This is most probably due to the lower neutron sensitivity of the n_TOF experimental setup relative to the ones used in previous measurements. The neutron sensitivity is particularly important in the case of the ^{96}Zr because all the neutron widths, except for the first resonance at 301 eV, are much bigger than the radiative width for, see § 5.9.1.

The MACS were calculated complementing the experimental data with the evaluated data from JENDL3.3 [88] for neutron energy above 40 keV. The present MACS for kT = 30 keV is compared in Table 6.12 with the rather discrepant and uncertain previous values. The recommended MACS of 10.7 ± 0.5 mbarn given in the compilation of Ref. [6] is based on the experiment by Toukan et al. [115], where the MACS was measured for the thermal temperature of 25 keV and extrapolated to 30 keV.

Table 6.12: Comparison of MACS values at kT = 30 keV thermal energy. Uncertainties are associated only to experimental values.

MACS (mbarn)	Reference	Year
41±12	[62]	1967
30±12	[107]	1971
28	[108]	1976
12±1	[116]	1983
(a) 10.7±0.5	[115]	1990
11	[110]	2000
12.28	[88]	2002
3.2	[111]	2005
8.8±0.4	This Work	

(a) Recommended value in Ref. [7].

The present MACSs (listed in Table 6.13) and the values of Ref.[6] are compared in Fig. 6.7. Uncertainties associated at the present MACS increase with thermal energy and the differences between the two data

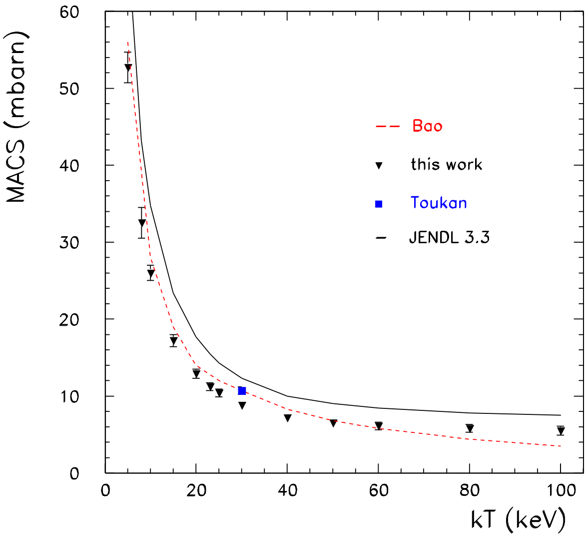

Figure 6.7: Comparison of present ^{96}Zr MACSs (full circles) with values from Refs. [6, 88, 115].

Table 6.13: MACS calculated with the present experimental data at different thermal energies. Above 40 keV data are complemented by JENDL/3.3 evaluations [88].

kT (keV)	MACS (mbarn)
5	52.7±2
8	32.5±1.3
10	26.0±1
15	17.2±0.8
20	12.9±0.6
23	11.2±0.6
25	10.4±0.5
30	8.8±0.4
40	7.2±0.4
50	6.5±0.4
60	6.1±0.4
80	5.7±0.4
100	5.5±0.4

sets are smaller at higher values of kT due to the fact that the present experimental values have been complement by the JENDL-3.3 evaluation [88].

6.2.7 ^{95}Zr MACSs

^{95}Zr is a branching point, its short half life (63 d) does not allow a direct measurement of the MACSs.

Table 6.14: Comparison of MACS (in mbarn) listed in the compilation of Ref. [117] and the one calculated using the MACSs of the Zr isotopes from this work, the calculation of the ^{95}Zr MACSs was done choosing the option (b) for ^{93}Zr values, see § 6.4.2

kT	MACS (mbarn)	
(keV)	Ref.[117]	This work
5	296	178
10	185	74
15	136	45
20	109	31
25	91	24
30	79±12	19
40	63	14
50	54	11
60	47	10
80	39	8
100	34	7

The fact that cross sections of many isotopes of Zr have been consistently overestimated in theoretical calculations [108,109,115] indicates that this may also be the case for ^{95}Zr.

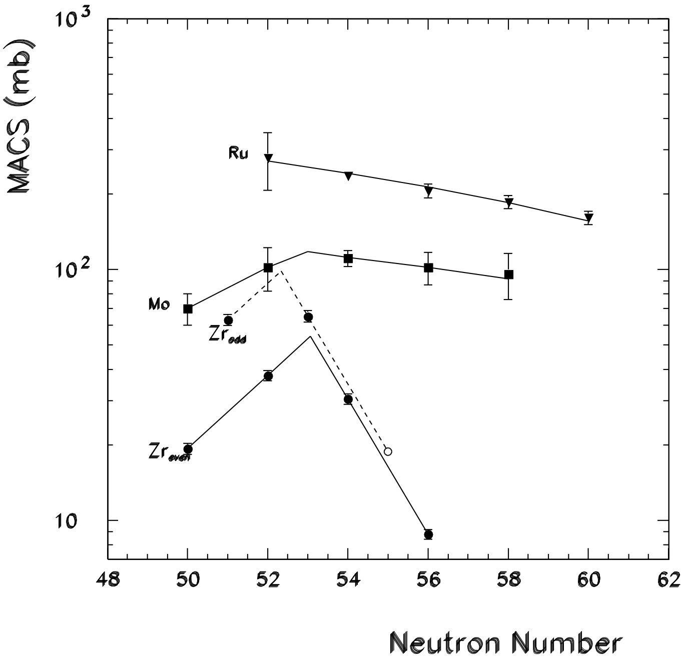

Figure 6.8. Experimental and calculated Maxwellian-averaged capture cross sections in the mass region 90 < A < 102 versus neutron number. Open symbol denote the calculated cross section for the ^{95}Zr. Even isotopes are connected with solid line, odd isotopes with dashed line.

Fig 6.8 shows the experimental stellar cross sections at kT = 30 keV for the even isotopes of molybdenum, ruthenium [6] and zirconium (from this work) connected by a solid line. For Zr also the odd isotopes are included (dashed line). The changes to a very smooth behavior going from Zr over Mo to Ru is due to the strong dependence on neutron number of the cross section. In the light of the systematic of Fig 6.8, it appears plausible to assume the same trend with neutron number for the even and odd Zr isotopes [118].

By normalizing the systematic for even isotopes to the experimental value for the odd isotopes, one obtains the ^{95}Zr cross section at the thermal temperature of 30 keV. The same technique has been used for thermal temperatures ranging from 5 to 100 keV; in Table 6.14 the values found are reported. The values found are significantly smaller than the ones reported in KaDoNiS [117] .

6.3 Astrophysical implications

6.3.1 Astrophysical implications on the s-process abundances

The impact of the improved MACS for the s-process abundance of Zr isotopes refers predominantly to the main s component produced in thermally pulsing low mass AGB stars. The contribution from massive stars is limited to about 2% [89, 90, 119]; therefore, the new cross section has negligible consequences for the abundance of Zr isotopes provided by the weak component. The s-abundances produced in thermally pulsing low mass AGB stars have been studied recently by Bisterzo et al. [120], updating previous calculations [8] with an improved stellar model and with a revised nuclear physics input, particularly the solar abundances from Ref. [120] have been adopted instead of [16] used in Ref.[8]. In Table 6.15 s-process yields obtained are reported using the data from Ref. [117] as input. The MACSs from Ref. [117] produce an overproduction of almost all the zirconium isotopes. The case of ^{96}Zr is particularly evident; indeed for this isotope the s-process contribution should be much lower since it is prevalently a r-process isotope.

Table 6.15: Solar abundances from Ref. [121] and s-process yield calculated using for the Zr's MACS of Ref. [6] and from this work. The s-process yields are normalized to the ratio $^{150}Sm/^{150}Sm_{\odot}$

Nucleus	$N_{\odot}$ Normalized to $N(Si)=10^6$ atoms	$N_s/N_{\odot}$ % MACSs from Ref. [6]	$N_s/N_{\odot}$ % MACS from this work
^{90}Zr	5.546	0.789	0.844
^{91}Zr	1.21	1.066	1.024
^{92}Zr	1.848	1.052	0.981
^{94}Zr	1.873	1.217	1.152
^{96}Zr	0.302	0.842	0.321

If the capture cross sections from [117] are replaced in these calculations by the present results, one obtains the result of the last column in Table 6.11. As can be seen with the new MACSs the s-process yield of all the isotopes decreases except for ^{90}Zr, where the contribution from low mass stars increases to almost 85% of the solar ^{90}Zr. Consequently, the r-process residual, $N_r = N_{\odot} - N_s$, changes significantly from 21 to 15%. Compared to the N_r distribution of the even isotopes in this mass region, this value is still higher but compatible within uncertainties as expected for a smooth r-process pattern [8]. Another important result is the drastic decrease of the N_s for ^{96}Zr that better suits the condition that the ^{96}Zr is predominately produced by the r-process. The lower MACSs for ^{93}Zr brings an overproduction of ^{93}Nb, where the s-abundances increase from 81% to 120 %, as will be better illustrated in § 6.3.3.

6.3.2 Astrophysical implications on SiC grains

Here the model predictions are presented for the Zr isotopic ratios and the Zr and Nb elemental abundances produced by slow neutron capture in C rich AGB stars of masses 1.8 $M_{\odot}$ and 3 $M_{\odot}$ and mettalicity around the solar (Z = 0.01, 0.02 and 0.03), compared to data from single mainstream silicon carbide (SiC) grains extracted from meteorites.

Using the MACSs from KaDoNiS [117] the comparison of AGB predictions to the Zr composition of single SiC data presented some problems: (1) it was not possible to match some of the grains with extreme deficit of ^{96}Zr, and (2) predicted ^{90}Zr/^{94}Zr and ^{92}Zr/^{94}Zr are lower than observed in a fraction of the grains, see Ref [122].

To model the nucleosynthesis in AGB stars the Monash-Mt Stromlo stellar structure code [123,124] has been used. The detailed s-process nucleosynthesis was calculated using a post-processing code that takes information on the stellar structure, such as temperature, densities, and convective velocities, and solves implicitly the set of equations that describes simultaneously changes of the stellar abundances due to the mixing and to nuclear reaction. This method is described in more detail in [125,126].

Figure 6.9 presents the resulting Zr isotopic composition at the stellar surface for four computed stellar models using the Zr neutron-capture cross sections from KaDoNiS, as compared from single SiC grains. The δ notation is used which represents the permil variation of the given ration with respect to the solar ration:

$$\delta\left(\frac{{}^{a}X}{{}^{b}X}\right)(‰) = \left[\frac{\left(\frac{{}^{a}X}{{}^{b}X}\right)_{grain}}{\left(\frac{{}^{a}X}{{}^{b}X}\right)_{standard}} - 1\right] \times 1000$$

In this notation δ=0 represents solar ratios and, e.g., δ=50 means a ratio 50 ‰ higher than solar.

The ^{96}Zr/^{94}Zr ratio depends on the activation of the ^{95}Zr branching point and thus on the neutron density reached during the neutron flux. In the 3 M$_{\odot}$ model (^{96}Zr/^{94}Zr) decreases during the first TDU episodes and then increases during the latest TDUs due to the marginal activation of the ^{22}Ne(α,n) neutron source in the final TPs. In the 1.8 M$_{\odot}$ model the opposite happens because the ^{22}Ne(α,n) neutron source is not activated, however, during the first few TPs the ^{13}C(α,n) neutron source is engulfed in the TPs instead of burning during the interpulse periods. The result is a higher neutron density produced by the ^{13}C(α,n) neutron source in the first phases of the evolution, which activates the branching point at ^{95}Zr and produces positive δ(^{96}Zr/^{94}Zr). After the first few TPs, the situation is renormalized to the standard case where ^{13}C burns radioactively producing low neutron densities and hence the δ(^{96}Zr/^{94}Zr) turns toward negative values. The results for the 3 M$_{\odot}$ models are comparable to those shown in Fig. 5 of Ref. [122].

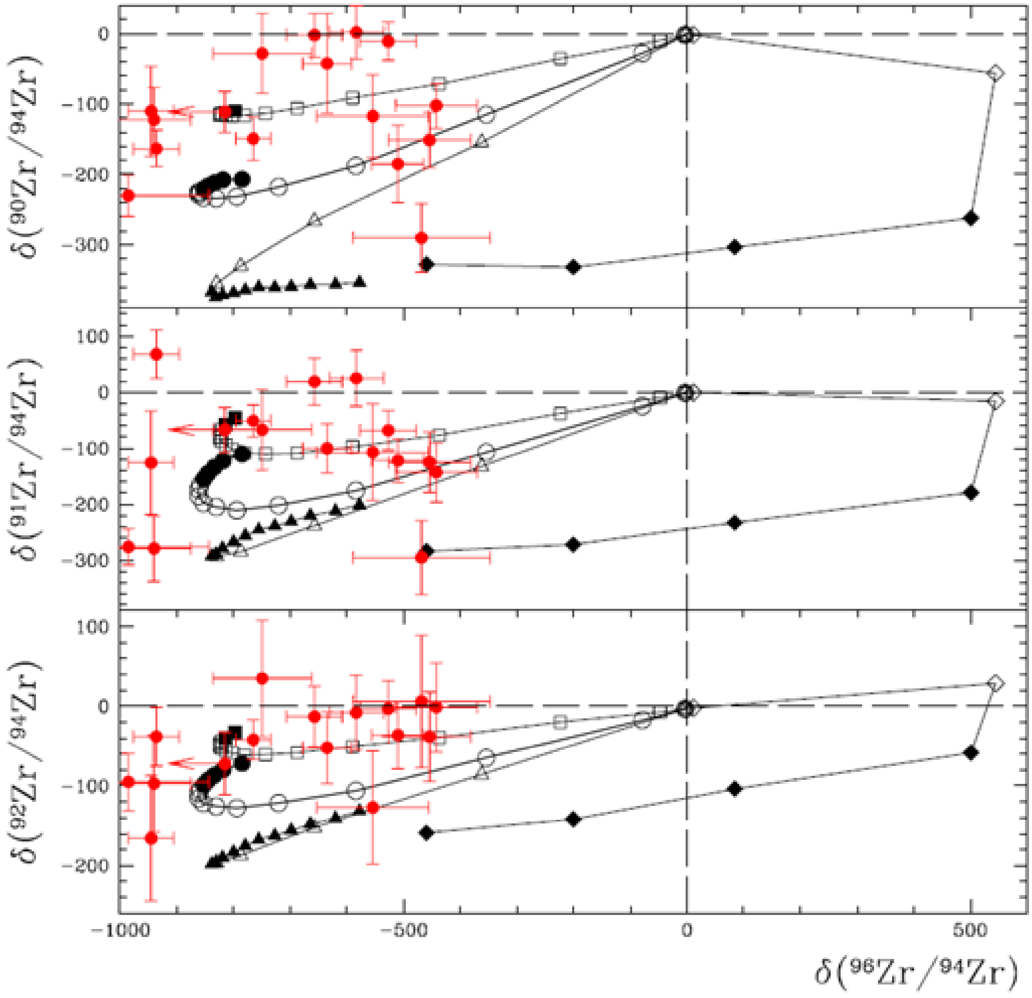

Figure 6.9 The Zr isotopic ratios measured in single SiC grains and predicted by our AGB models computed using the KaDoNiS neutron-capture cross sections of the Zr isotopes. Ratios are plotted using the δ notation. The data are represented by red circles with 2σ standard deviations error bars. The models are represented by black symbols connected by solid lines, where open and full symbols represent TDUs resulting in C/O<1 and C/O > 1, respectively, at the stellar surface. circles: 3 $M_{\odot}$ Z = 0.02, triangles 3 $M_{\odot}$ Z = 0.01 squares 3 $M_{\odot}$ Z = 0.03, diamond 1.8 $M_{\odot}$ Z = 0.01.

Form Fig 6.9 can be noticed that: (1) while the observed $\delta(^{96}Zr/^{94}Zr) < -850$ can be covered by the models, the handful grains with $\delta(^{96}Zr/^{94}Zr) > -850$ are not reached. (2) Some of the grains with $\delta(^{90,91,92}Zr/^{94}Zr) \approx 0$ are difficult to match

All the models computed using the new cross sections from this work are shown in Fig. 6.10. In general, these models provide a better match with the data except for ^{92}Zr. The 3$M_\odot$ Z =0.02 and 0.03 models computed with the new cross sections can reach $\delta(^{96}\mathrm{Zr}/^{94}\mathrm{Zr}) < -900$, as observed.

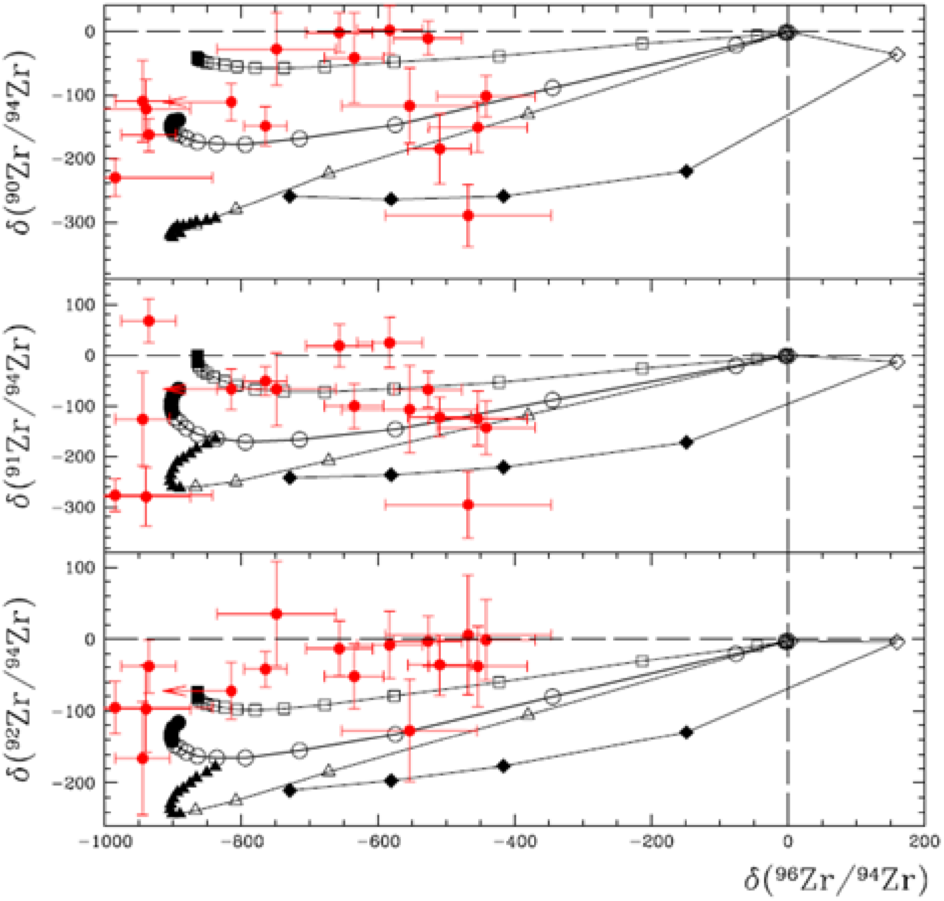

Figure 6.10. Same as in Fig. 6.9 but with the models computed using the neutron-capture cross sections from this work, circle 3$M_\odot$ Z = 0.02, triangle 3 $M_\odot$ Z = 0.01, square 3$M_\odot$ Z = 0.03, diamond 1.8$M_\odot$ Z = 0.01, down triangle 1.8 $M_\odot$ Z = 0.02, hexagon 1.8$M_\odot$ Z = 0.03.

Higher values can be reached considering models of lower masses, such as our 1.8 $M_\odot$ cases, where the ^{13}C(α,n) neutron source is engulfed in the first few TPs thus initially shifting the $\delta(^{96}\mathrm{Zr}/^{94}\mathrm{Zr})$ first to positive values. The $\delta(^{90,91,92}\mathrm{Zr}/^{94}\mathrm{Zr}) \approx 0$ measured in some grains are matched by the stellar models of metallicity slightly higher than solar, i.e., our Z = 0.03 models.

6.3.3 Elemental Zr and Nb abundances in SiC grains

Kashiv et al. [127] measured the elemental abundances of Zr and Nb in stardust SiC grains. The production of monoisotopic Nb is strictly connected to the production of Zr since most of the stable ^{93}Nb is made by the radioactive decay of ^{93}Zr, e.g., ≈ 80% of Nb is initially produced as ^{93}Zr in our 3 $M_{\odot}$ $Z = 0.02$ model. By comparing SiC data to s-process model predictions from [122], Kashiv [127] observed that grain data are consistent with a scenario where all ^{93}Zr initially present has decayed into ^{93}Nb, which is reasonable since the ages of the grains are much longer (they are at least as old as the Sun) than the half life of ^{93}Zr. A problem is that some grains showed Nb/Zr greater than the model predictions.

To explain these data Kashiv et al. [127] proposed that some Zr must have been removed from the stellar gas from which the SiC formed, but no Nb. This could have happened because some Zr would be incorporated in other types of minerals, such as ZrC, which condenses at higher temperature than, and thus before, SiC. The main problem with this scenario is that Nb is as refractory as Zr, so NbC is also expected to have condensed before SiC. Thus, it is not obvious why also Nb should not have been removed from the gas.

Fig. 6.11 reproduces Fig. 1 of Ref. [127] using the Monash models computed with the cross sections from this work. Models computed with the standard cross sections or with the new cross sections only for the stable Zr isotopes are very similar to the models presented by Ref. [127]. However, changing the cross sections of the unstable Zr isotopes resulted in a significant shift of the curves towards the left, i.e., towards higher Nb/Zr ratios. This is because the new cross section of ^{93}Zr is lower than the previous estimate, which results in more ^{93}Zr, and eventually ^{93}Nb, being produced.

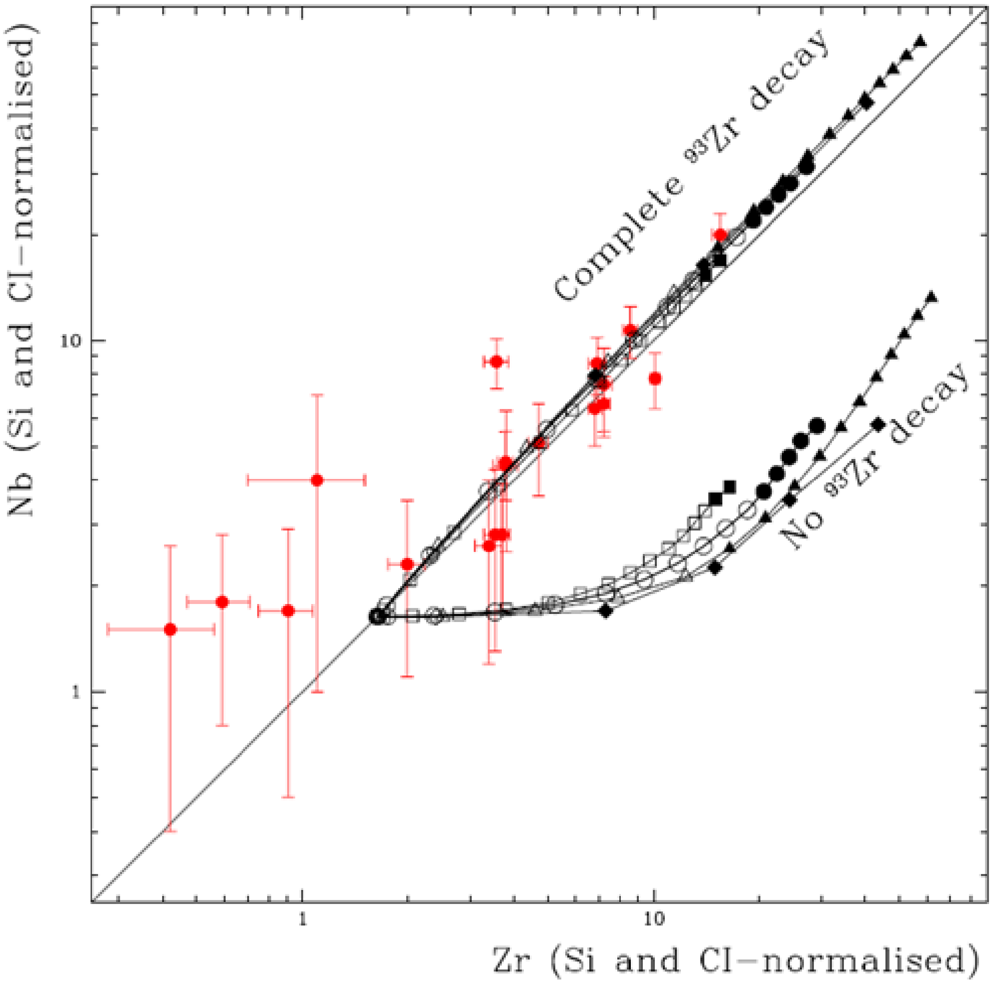

Figure 6.11 - The Zr and Nb elemental abundances (relative to Si and to CI values of Ref. [121]) measured in single SiC grains and predicted by our AGB models computed using the new neutron-capture cross sections of the Zr isotopes. The data are represented by red circles with 2σ standard deviations error bars. As in the previous figures, the models are represented by black symbols connected by solid lines, where open and full symbols represent TDUs resulting in C/O<1 and C/O>1, respectively, at the stellar surface: circle 3 $M_{\odot}$ Z = 0.02, triangle 3 $M_{\odot}$ Z = 0.01 squares 3 $M_{\odot}$ Z = 0.03, diamond 1.8 $M_{\odot}$ Z = 0.01. This figure can be compared to Fig. 1 of Ref. [127]

Thus, while the previous models were located to the right of the solid line, representing the solar Nb/Zr ratio, and of most of the data in Fig. 6.11, the models computed with the new ^{93}Zr cross section are located to the left of the solid line and go through most of the data.

Hence, it would appear that removal of Zr without removal of Nb is not needed to explain the data. Removal of both elements would shift the predictions parallel to the solid line (i.e., keeping the Nb/Zr ratio constant) and help explain data with Zr and Nb abundances lower than the models predicted for C/O > 1.

Conclusion

The (n,γ) cross sections of ^{90,91,92,93,94,96}Zr have been measured over a wide range of neutron energies with improved accuracy using the innovative features of the n_TOF facility at CERN and the GELINA facility at Geel. Predictions of the production of Zr isotopes are critical for the s-process modeling and for identifying the range of masses and metallicities of the SiC parent stars. Several of the Zr isotopes are close to the neutron magic number N=50, ^{90}Zr having exactly N=50. Hence the production of ^{90,91,92,93,94}Zr is sensitive to the overall neutron flux, which is mostly defined by the ^{13}C(α,n) neutron source. The abundance of the remaining stable isotope of Zr, ^{96}Zr, is determined by the activation of the branching point at the unstable ^{95}Zr. Hence the production is sensitive to the neutron density, which is mostly defined by the ^{22}Ne(α,n) neutron source.

The low neutron induced background that was obtained with the optimized experimental setup of the two facilities contributed to a significant improvement of the small neutron capture cross section data. In particular the performance of the n_TOF facility allowed for the first time to measure the capture cross section of ^{91}Zr in the region from 10 eV to 26 keV, the previous measurement stopped at 20 keV.

The capture kernels of the analysed resonances were lower, except for ^{94}Zr, than the ones extracted from the previous experiments. This is essentially due to the lower neutron sensitivity of the detector used in these measurements compared to the previous ones, as discussed in § 5.13, for the stable isotopes, while for ^{93}Zr the large difference found is mostly due to a better ratio signal/radioactive background achieved thanks to the high instantaneous neutron flux, which makes the n_TOF facility unique for measurements on unstable isotopes .

Based on the present results, Maxwellian averaged cross sections for s-process studies of stellar nucleosynthesis were obtained and may be used to improve the recommended data from KaDoNiS [117].

The principal result of these measurements is the improved accuracy in the MACS determination. For all stable isotopes the MACS are calculated in the region of interest with uncertainties smaller than 5%, which is a prerequisite to improve the stellar models.

Particularly interesting are the new values of the MACSs for ^{93}Zr and ^{96}Zr, for the first isotope the difference found is about 35% lower than the reference value, while for the second it is about 25%. These new values give a clear indication that also the value of the MACSs for the ^{95}Zr may be much lower than the recommended one. In this thesis a simple calculation for the MACSs of the ^{95}Zr was made. The new values are about 75% lower than those recommended in KaDoNiS but in good agreement with some theoretical values as the ones reported in MOST [111,112].

The values of the MACSs from this work when used in stellar models give in general a better match between the AGB model predictions and the Zr isotopic ratios, and the Zr and Nb elemental compositions measured in mainstream stardust SiC grains.

Although these measurements were made in a wide range of energies, this range was not wide enough to make the calculation of the MACSs independent on the evaluated library. It is the principal limit of this work (particularly for ^{93}Zr where the largest differences were found). The neutron energy ranges were not sufficiently wide to have a complete independent information on the MACSs at the thermal temperature of interest, since all the data had to be complemented by evaluated data from the libraries. In a few cases the data from the libraries have been scaled in order to take in account the big difference found.

These new results give a strong impulse on the need for new measurements in order to confirm the results and extend the neutron energy in order to permit an unambiguous calculation of the MACSs. In order to meet these goals it is necessary (1) to have an even lower background than the n_TOF one, which would allow a better determination of the kernels and yield also information on the URR; (2) to have a better control of the samples, which as shown in the case of ^{96}Zr has an extreme importance for a high accuracy measurement.

A new series of measurements have started at the GELINA facility using Zr samples in metallic form, which should ensure to meet both the requisites to improve the accuracy and to extend the neutron energy range.

Bibliography

[1] E. Burbidge, G. Burbidge, W. Fowler and F. Hoyle. Rev. Mod. Phys. 29, 547 (1957).
[2] P. Seeger, W. Fowler, and D. Clayton. Ap. J. Suppl. 97, 121 (1965).
[3] F. Käppeler et al. Ap. J. 257, 821 (1982).
[4] D. Lambert et al. Ap. J. 450, 302 (1995).
[5] A. Davis et al. in Nuclei in the Cosmos V, edit by N. Prantzos and S. Harissopulos (Editions Frontières. Paris 1998), pp. 563.
[6] Z. Bao et al. Atomic Data Nucl. Data Tables 76, 70 (2000).
[7] F. Käppeler. Prog. Nucl. Part. Phys. 43, 419 (1999).
[8] C. Arlandini et al. Ap. J. 525, 886 (1999).
[9] F. Hoyle. The synthesis of the elements from hydrogen. Monthly Notices of the Royal Astronomical Society 106(1946) 343.
[10] P. Merrill. Science 115(1952) 676.
[11] H.Palme and H. Beer, in Landolt-Bornestein New Series. Group I. vol. I/3a. edited by O. Madelung (Springer. Berlin. 1993). p. 196.
[12] C. Iliadis, Nuclear Physics of the Stars. Wiley - VCH Verlay GmbH & Co. KGaA Weinheim 2007. ISBN 978-3-527-40602-9.
[13] O. Straniero, R. Gallino, S. Cristallo. Nuclear Physics A 777(2006) 311.
[14] M. Lugaro, Stardust from meteorites. An introduction to presolar grains (Stardust from meteorites / Maria Lugaro. World Scientific Series in Astronomy and Astrophysics, Vol. 9, New Jersey, London, Singapore: World Scientific. ISBN 981-256-099-8, 2005, XIV, 209 pp.)
[15] B. S. Meyer. The r-, s- and p-Processes in Nucleosynthesis Annual Review of Astronomy and Astrophysics 32(1994) 153-190.
[16] E. Anders, and N. Grevesse. Abundances of the elements – Meteritic and solar Geochimical et Cosmochimica Acta 53 (1989) 197.
[17] R. Taam, S. Woosley. T. Weaver. and D. Lamb. Ap. J. 413(1993) 324.
[18] D. D. Clayton, W. A. Fowler, T. E. Hull, B. A. Zimmerman. Ann. Phys. 12(1961) 331.
[19] F. Käppeler et al. Ap. J. 354(1990). 630.
[20] D. D. Clayton, M. Rassbach. Ap. J. 148(1967) 69.
[21] R. Gallino et al. Astrophys. J. 497(1998) 388.
[22] C. Travaglio, et al. Astrophys. J. 549(2001) 346.

[23] C. Arlandini, et al. Astrophys. J. 525(1999) 886.
[24] R. McClure. Ap. J. 280(1984) 231.
[25] E. Bohm-Vitense, J. Nemec, and C. Proffitt. Ap. J. 278(1984) 726.
[26] V. Smith and D. Lambert. Ap. J. 294(1985) 294.
[27] D. Lambert et al. Ap. J. 450(1995) 302.
[28] E. Anders and N. Grevesse. Geochim. Cosmochim. Acta 53(1989) 197.
[29] U.Ott. Nature 364(1993) 25.
[30] E. Zinner. Science 271(1996) 41.
[31] E. Anders and E. Zinner. Meteoritics 28(1993) 490.
[32] W. Ratynski and F. Käppeler *Phys. Rev. C* 37(1988) 595.
[33] G. Lorusso et al. Nucl. Instr. and Meth. A 523(2004) 622.
[34] S. Marrone et al. Nucl. Instr. and Meth. A 517 (1-3) (2004) 389.
[35] A. D. Carlson et al. Nuclear Data Sheet 110(2009) 3217.
[36] D.B. Syme, Nucl. Instr. Meth. 198 (1982) 106.
[37] The n_TOF Collaboration. Proposal for a Neutron Time of Flight Facility, CERN/SPSP 99-8. SPSC/P 310. CERN. Geneva. 1999.
[38] C. Rubbia et al. A high Resolution Spalation driven Facility at the CERN-PS to measure Neutron Cross Sections in the Interval from 1 eV to 250 MeV. CERN/LHC/98-02 (EET)-Add.1. CERN. Geneva. 1998.
[39] C. Borcea et al. Nuc. Instr. and Meth. A 513(2003) 524.
[40] D.J. Simon. Conference Proceedings. "5th European Particle Accelerator Conference". Sitges. Barcellona. Spain. IOP. Bristol (1996)205.
[41] U. Abbondanno et al. Tech. Rep. CERN-SL_2002-053 ECT. 2003
[42] V. Vlachoudis et al. Particle distribution entering the vacuum tube 80x80x60 cm3 lead target. SL-Note-2000-029 (EET). (30 March 2000).
[43] R. Plag, M. Heil, F. Käppeler, P. Pavloulos, R. Reifarth, and K. Wisshak. Nucl. Instr. and Meth. A 496 (2003) 425.
[44] U. Abbondanno et al. Nucl. Instr. and Meth. A 538 (2005) 692.
[45] D. Tronc, J. M. Salomé, K.H. Böckhoff. Nuclear Instruments and Method in Physics Research. A 228 (1985) 217.
[46] J.M. Salomé, R. Cools. Nucl. Instr. and Meth. A 179(1) (1981)13
[47] A. Borella, F. Gunsing, M. Moxon, P. Schillebeeckx and P. Siegler. Phis. Rev. C 76(2007) 0146051-10.
[48] F. Gunsing, CEA/saclay. Presented at WONDER 2006. Caradache
[49] F. Gunsing et al.(n_TOF collaboration). Nucl. Instr. and Meth. B 261(2007) 925.
[50] S. Kopecky and A. Brusegan. Nucl. Phys. A 773

[51] K. Berthold, C. Nazareth, G. Rohr and H. Weigmann. Very high resolutions measurements of the total cross section of natural Iron. in Proc. Intern. Conf. on Nuclear Data for Science and Technology. Gatlinburg. Tennessee. May 9-13. 1994 218.

[52] S. Kopecky, P. Siegler and A. Moens. Low energy transmission measurements of 240.242Pu at GELINA and their impact on the capture width. Proc. Int. Conf. Nuclear data for Science and Technology. edited by O. Bersillon et al. (CEA. Paris. 2008) 623.

[53] A. Foderaro. The Elements of Neutron Interaction Theory. The MIT Press. 1971.

[54] Neutron Radiative Capture. Vol. 3. Editors A. Michaudon, S. Cuerjacks and R.E. Chrien. 1984.

[55] E. P. Wigner, L. Eisenbud. Phys. Rev. 72 (1) (1947) 29.

[56] A. M. Lane, R. G. Thomas, R-matrix theory of nuclear reactions, Rev. Mod. Phys. 30 (2) (1958) 257.

[57] F. Fröhner, Evaluation and analysis of nuclear resonance data, Tech. Rep. JEFF Report 18, OECD/NEA (2000).

[58] J. Humblet, L. Rosenfeld. Nucl. Phys. 26 (4) (1961) 529.

[59] E. Vogt. Rev. Mod. Phys. 34 (4) (1962) 723.

[60] F. Schmittroth,W. Tobocman. Phys. Rev. C 3 (1971) 1010.

[61] M.C. Moxon et al. Nucl. Instr. and Meth. in Phys. Res. A 24 (1963) 445.

[62] R. Macklin et al. Phys. Rev. 159 (1967) 1007.

[63] R. Macklin, B. J. Allen. Nucl. Instr. and Meth. in Phys. Res. A 91 (1971) 565.

[64] F. Corvi, G. Fioni, F. Gasperini, P. B. Smith. Nuclear Science & Engineering 107 (1991) 272.

[65] GEANT, detector description and simulation tool. CERN Program Library W5013 (1994).

[66] J. Briesmeister, MNCP-A General Monte Carlo N-Particle Transport Code-Version 4c2. LA-1370-M. 2000.

[67] U. Abbondanno et al. Nucl. Instr. and Meth. A 521(2004) 454.

[68] A. Borella, G. Aerts, F. Gunsing, M.C. Moxon, P. Schillebeeckx, R. Wynants. Nucl. Instr. Meth. A **577** (2007) 626

[69] F.H. Fröhner. *Evaluation and analysis of nuclear resonance data*. JEFF Report 18. 2000.

[70] D.J. Hughes. J. Nuclear Energy 1(1955) 237.

[71] J.E. Lynn and E.R. Rae. J. Nuclear Energy 4(1957) 418.

[72] F.H. Fröhner, E. Haddad.W.M. Lopez and S.J. Friesenhaln. *Accuracy on resonance parameters from combined area and self-indications measurements*. Proceedings of the International Conference on

Neutron Cross Section Technology. Washington. D.C:. 22-24 March. 1996. 55-66.

[73] E.R. Rae, E.R. Collins, B.B Kinsey, J.E. Lynn and E.R. Wiblin. Nucl. Phys. 5(1958) 89.

[74] J.E. Lynn. Nucl. Phys. 7(1958) 559.

[75] A.M. Larson. Update Users guide for SAMMY: Multilevel R-Matrix Fits to Neutron Data Using Bayes Equation. ORNL/TM – 9179/R6 ENDF-364. July 2003.

[76] H. Beer, F. Voss, and R.R. Wi nters. APJS. 80(1992) 403.

[77] C. H. Westcott, J. Nucl. Energy 2(1955) 59.

[78] S. F. Mughabghab Internetional Nuclear data committee, Thermal neutron capture cross sections resonance integrals and g-factors INDC(NDS)-440 February 2003.

[79] S.F. Mughabghab. Atlas of Neutron Resonances. Resonance Parameters and Thermal Cross Sections Z=1-100 (Elsevier Science. Amsterdam. 2006).

[80] A. de L. Musgrove,.J. Boldeman, J. Allen, B.J. Harvey,and R. Macklin. Aust. J. Phys. 30 (1977) 391.

[81] R.E. Toohey, and H.E. Jackson. Phys. Rev. C 9 (1974) 346.

[82] W.M. Good, and H. Kim. Phys. Rev. 165 (1968) 1329.

[83] G. Tagliente et al. Phys. Rev. C 77 (2008) 035802.

[84] J.W. Boldeman, B.J. Allen, A.R. de L. Musgrove, and R.L. Macklin. Nucl. Phys. A 246 (1975) 1.

[85] J.W. Boldeman, A.R. de L. Musgrove, B.J. Allen, J.A.Harvey, and R.L. Macklin. Nucl. Phys. A 269 (1976) 31.

[86] R.J. Stancliffe, M. Lugaro, A.I. Karakas, and C.A. Tout. Nucl. Phys. A758 (2005) 569.

[87] G. Tagliente et al. Phys. Rev. C 78 (2008) 045804.

[88] T. Nakagawa, S. Chiba, T. Hayakawa, T. Kajino. Atomic Data Nucl. Data Tables 91 (2005) 77.

[89] S.P. Kapchigashev, and Yu.P. Popov. Soviet Journal of Nuclear Physics. 4 (1967) 486.

[90] K. Shibata et al. J. Nucl. Sci. Technol. 39 (2002) 1125.

[91] G. Leinweber et al. Nucl. Sci. Eng. 134 (2000) 50.

[92] K. Ohgama, M. Igashira, and T.Ohsaki. J. of Nucl. Sci.Tech. 42 (2005) 333.

[93] J.F. Minster, and C.J. Allegre. Geochimica et Cosmochimica Acta 46 (1982) 565.

[94] S.S. Moskalev, H.V. Muradian, and Yu.V. Adamchuk.Nucl. Phys. 53 (1964) 667.

[95] Z.M. Bartolome et al. Nucl. Sci. Eng. 37 (1969) 137.

[96] G. Tagliente et al. Phys. Rev. C 81(2010) 055801.
[97] R.L. Macklin. Astrophysics and Space Science 115(1985) 71.
[98] R.L. Macklin, J.A. Harvey. and N.W. Hill. Nuclear Science and Engineering 92(1986) 525.
[99] G. Tagliente et al. submitted Phys. Rev. (2010).
[100] M. M. Salah, J. a. Harvey, N. W. Hill, A. Z. Hussein, and F. G. Perey, “Accurate Determination of the Parameters of the 292.4 eV Resonance of 91Zr and the 301.1 eV Resonance of 96Zr”, Proc. Int. Conf. Nuclear Data for Basic and Applied Scince, Santa Fe, New Mexico, 1985, p. 593.
[101] C. Coceva, P. Giacobbe, M. Magnani, Proc. of the Conf. on Nucl.Cross Sections F. Techn., Knoxville (1979) p.319; A. Brusegan, F. Corvi, G. Rohr, B.J. Allen, Proc. of the Conf. 4. Symp. Neutr. Capt. Gamma-Ray Spectrosc., Grenoble (1981) p.406.
[102] A.R. de L.Musgrove, W.M. Good and J.A. Harvey, Australian Atomic Energy Commission E415 report (1977).
[103] F. Corvi, G. Fioni, F. Gunsing, P. Mutti, L. Zanini, Nucl. Phys. A697 (2002) 581.
[104] Experimental Nuclear Reaction Data (EXFOR). http://www-nds.iaea.org/exfor/exfor.htm
[105] For results compiled in evaluated nuclear data libraries see for example International Atomic Energy Agency (IAEA) on www-nds.iaea.org. or the OECD Nuclear Energy Agency on ww.nea.fr/html/dbdata/
[106] A. de L. Musgrove, B. Allen, J. Boldeman, and R.L. Macklin. in Neutron Physics and Nuclear Data for Reactors and other Applied Purposes (OECD. Paris. 1978). p. 449.
[107] B. Allen, J.H. Gibbons, and R.L. Macklin. Adv. Nucl. Phys. 4 (1971) 205.
[108] J. Holmes, S. Woosley, W. Fowler, and B. Zimmerman. Atomic Data Nucl. Data Tables 18 (1976) 305.
[109] M. Harris, Astrophys. Space Sci. 77 (1981) 357.
[110] T. Rauscher, and F.-K. Thielemann. Atomic Data Nucl. Data Tables. 75 (2000) 1.
[111] S. Goriely, Hauser-Feshbach *rates for neutron capture reactions* (version 9/12/2002). (2002) http://www-astro.ulb.ac.be/Html/hfr.html
[112] S. Goriely, Hauser-Feshbach *rates for neutron capture reactions* (version 8/29/2005). (2005) http://www-astro.ulb.ac.be/Html/hfr.html
[113] wwwndc.jaea.go.jp/nakagawa/MaxwAv/Figs/Zr092.pdf
[114] B. Allen, J.H. Gibbons, and R.L. Macklin. Adv. Nucl. Phys. 4 (1971) 205.

[115] K.A. Toukan, and F. Käppeler. The Ap. J. 348(1990) 357.

[116] J. Wyrick and W. Poenitz, Technical report ANL-83-4, Argonne National Laboratory (1983) 196.

[117] I. Dillmann, M. Heil, F. Käppeler, R. Plag, T. Rauscher, and F.-K. Thielemann, in Capture Gamma-Ray Spectroscopy and Related Topics, AIP Conference Series 819, edited by A.Woehr and A. Aprahamian (AIP, New York, 2005), p. 123 (see also [http://www.kadonis.org]).

[118] R.R. Winter, F. Käppeler, K. Wisshak, A. Mengoni, and G. Reffo. Ap. J. 300(1986) 41

[119] C.M. Raiteri, R. Gallino, M. Busso, D. Neuberger, and F. Käppeler. Ap. J. 419 (1993) 207.

[120] S. Bisterzo, F. Käppeler, R. Gallino, M. Heil, and C. Domingo Pardo, Nuclei in the COSMOS-IX, eds. A. Mengoni et al. (Proceedings of Science, SISSA, Trieste, 2006), http://pos.sissa.it/,contribution 077.

[121] Lodders, K., Palme H., & Gail, H.P. 2009, *Abundances of the elements in the solar system* in: Landolt-Bornstein, New Series, Vol. VI/4B, Chap. 4.4, Trumper, J.E. (ed.), Berlin, Heidelberg, New York: Springer-Verlag, p. 560-630.

[122] M. Lugaro, A.M. Davis, R. Gallino, J. Pellin, O. Straniero, and F. Käppeler.Ap. J. 593 (2003) 486.

[123] Lattanzio, J., Frost, C., Cannon, R., & Wood, P. Mem. Soc. Astron.vItaliana, 67(1996) 729.

[124] Karakas, A. I., Lattanzio, J. C., & Pols, O. R. Publ. Astron. Soc. Australia,19(2002) 515.

[125] M. Lugaro, C. Ugalde, A. I. Karakas, J. Görres, M. Wiesher, J. C. Lattanzio & R. C. Cannon. Ap. J. 615(2004) 934.

[126] S. Goriely, A. Mowlavi. A&A 362(2000) 599.

[127] Y .Kashiv, A. M. Davis, R. Gallino, Z. Cai, B. Lai, S. R. Sutton & R. N. Clayton. Ap.J.713(2010) 212.

[128] R.L. Macklin et al. Nucl. Instr. And Meth. in Phys. Res. A 164(1979) 213.

[129] K. Günther et al. Science 277(1997)1281.

Summary

Nuclear astrophysics is an interdisciplinary branch of physics involving close collaboration among researchers in various subfields of nuclear physics and astrophysics, with significant emphasis in areas such as stellar modeling, measurement and theoretical estimation of nuclear reaction rates, cosmology, cosmochemistry, gamma ray, optical and X-ray astronomy. In general terms, nuclear astrophysics aims to understand the origin of the chemical elements and the energy generation in stars.

This work concerns the measurements of the neutron capture cross sections of ^{90,91,92,93,94,96}Zr isotopes, performed at the time-of-flight facilities n_TOF at CERN and GELINA at IRMM and their implication in stellar modeling.

In Chapters I the nucleosynthesis beyond Fe is presented. The s-, r, p and rp-process mechanisms and the stellar neutron sources for these processes are described. This work is focused on the s-process, to this aim a detailed description of the AGB stars, which are the main sites for the s-process, and the nucleosynthesis in such stars is given.

In Chapter II the stellar models are introduced, from the phenomenological description of the classic model, which gives a good description of the abundances of the elements but does not make any assumption on the stellar site or the specific reaction which acts as neutron source, to the more realistic thermal pulsing low mass AGB

stars model. In this chapter also a brief description of the methods used to measure the abundances of the elements is given.

Chapter III is devoted to the characteristics of the neutron facilities, how neutrons can be generated and their energy measured. Particularly the two facilities were the Zr measurements were performed, n_TOF and GELINA, and their experimental apparatuses are described in details.

In Chapter IV, the measurement and data analysis techniques are presented. The radiative neutron capture process is described and definitions of theoretical and experimental yield, resonance parameters, kernel and Maxwellian-averaged cross sections are given.

In Chapter V, the experimental results for the ^{90,91,92,93,94,96}Zr(n,γ) measurements are presented. The different aspects of the analysis performed are described in detail, from the determination of the weighting function to the measurement and subtraction of the background. The extracted cross sections in the resolved resonance region are then given.

Finally in Chapter VI, the Maxwellian-averaged cross section for different thermal energies of all Zr isotopes measured is calculated. From the MACSs of the experimental data a tentative value of the MACS of ^{95}Zr is obtained. These new results when used in the thermal pulsing low mass AGB stars model reproduce better the data obtained from the spectroscopic observations and meteorites.

Acknowledgment

To be a PhD student at the age of 44 year old is something not very usual. It was not easy to explain the why, especially to my family and my colleagues, but it is never too late to add another island of knowledge into the ocean of my ignorance.

I am very grateful to my promoter Prof. Cyrillus Wagemans, who gave me the opportunity and honour to work with him, and to Peter Schillebeeckx; thanks to their frequent discussions, sharp corrections and fruitful suggestions I have learnt a lot during these years.

Most of the work of this theses is related to measurements done at n_TOF facility, I have been part of the n_TOF collaboration since the start of the collaboration, in the year 2000. It is due to the contribution of all people who have worked there over the years that n_TOF belongs to the top neutron facility in the world. I am very grateful to many colleagues like Cristian, Cesar, Carlos, Daniel, Laure, Christophe, Julien, Shawn, Christos, Gaelle, Marita, Luc, Eric, Stefano, Rita, Pierfrancesco, Giuseppe, Dimitri (I apologize to those I forgot to mention) who contributed in different ways to this thesis. I want to express my particularly gratitude to F. Käppeler, F. Gunsing, A. Mengoni, J. L. Taìn and N. Colonna for their very helpful comments, discussions and suggestions during the measurements and data analysis.

Part of this work was done at GELINA facility, it was an important step in my life, a very enjoyable (not only because of the good beer) and fruitful experience. It was also a pleasure for me to work at GELINA with people like Alessandro, Stefan, Peter, Christos (the same of a few lines before), Ruud and Jean-Claude.

I am also very grateful to R. Gallino and S. Bisterzio for their help in the calculation of the impact of new cross sections in the s-process abundances. An especial thanks to Maria Lugaro who let me work with her at Monash University in Melbourne on the astrophysical implication of the result of this works.

Special mention deserve my "merengue" mate Paolo M., it is a pleasure to work with him but even more to be his friend, to share with him trips and talks.

Finally I want to thank my three little stars, Silvia, Sara and Stefania (it is not a coincidence that their names begin with S), for all the time I steal to them because of my job and especially for this thesis, they see it completely useless, for them I already know everything. To my mother who has devoted her life to allow me to be who I am. To my wife Daniela who patiently let me do my work without protesting too much, and many times she has reasons to do that.

To my good star that even during the big storms, guides me into the safe harbour.